MAGNETIC SUSCEPTIBILITY- BASED WHITE MATTER MAGNETIC RESONANCE IMAGING TECHIQUES

WAY CHERNG CHEN

NUFFIELD DEPARTMENT OF CLINICAL NEUROSCIENCES

KEBLE COLLEGE

UNIVERSITY OF OXFORD

A THESIS SUBMITTED

FOR THE DEGREE OF DOCTOR OF PHILOSOPHY D.PHIL.

TRINITY TERM 2013

Abstract

Gradient echo (GRE) imaging, a magnetic resonance imaging (MRI) technique that is sensitive to changes in the magnetic susceptibility property of tissues, has recently revealed significant signal heterogeneity in white matter (WM) at high magnetic field ($B_0 \geq 3T$). Various aspects of the underlying white matter microstructure have been linked to the observed contrast between white matter regions. This thesis investigates the origins of the observed differences in GRE signal behaviour.

We proposed an explicit multi-compartmental model of WM that incorporates realistic representation of the geometry and magnetic susceptibility of the underlying microstructure that can be used to study the effects of WM microstructural changes on GRE signal characteristics. In particular, we looked at the apparent transverse relaxation rate (R_2*) and the resonance frequency, as well as their respective deviations from mono-exponential decay and linear phase evolution.

Next, we investigated the effect of WM fiber orientation on GRE signal using healthy human volunteers at 3T by correlating the GRE signal from different WM regions with WM fiber orientation information. Using literature-based parameters, we demonstrated that the geometric model predicted similar trends.

Lastly, we studied the effect of myelin on GRE signal using a cuprizone mouse model at 7T. An *ex vivo* study was used to correlate GRE signal in fixed mouse brain with normalized myelin stain intensity. Simulated GRE signal from hypothetical scenarios of demyelination were then compared with the experimental results. R_2* and resonance frequency were then used in an *in vivo* longitudinal study to track myelin changes during demyelination and subsequent remyelination.

Acknowledgements

Many thanks to the members of the Physics group at FMRIB for their valuable insights and criticisms of this work, especially my supervisor Dr Karla Miller, who has been extremely patient and whose guidance has been invaluable. Special thanks also go out to Dr Sean Foxley and Wilfred Lam for their assistance in many aspect of my work. I would also like to thank Dr Kai-hsiang Chuang from Singapore Bioimaging Consortium (SBIC) for his generous support and guidance.

Thank you to my beloved family for their continual support these years, especially to my wife who has been very encouraging through these difficult times. I will also like to take this opportunity to thank my baby girl for brightening up my days with her lovely smile.

Lastly, I will like to acknowledge the Agency For Science Technology and Research (A*STAR) for the funding of this D.Phil.

Contents

List of Figures

List of Abbreviations

Abbreviation	Definition
ADC	Analogue to digital converter
CC	Corpus callosum
CMT	Charcot-Marie-Tooth disease
CSF	Cerebrospinal fluid
DTI	Diffusion tensor imaging
EPI	Echo planar imaging
FID	Free induction decay
FOV	Field of view
GM	Grey matter
GRE	Gradient echo
HWHM	Half width at half maximum
LFB	Luxol fast blue
MRI	Magnetic resonance imaging
MRS	Magnetic resonance spectroscopy
MS	Multiple sclerosis
MT	Magnetization transfer
MWF	Myelin water fraction
NAWM	Normal appearing white matter
NBF	Neutral buffered formalin
NMR	Nuclear magnetic resonance
PBS	Phosphate buffered saline
PD	Proton density

PVC	Polyvinylchloride
QSM	Quantitative susceptibility mapping
RF	Radio frequency
RGB	Red-green-blue
ROI	Region of interest
SE	Spin echo
SNR	Signal to noise ratio
TE	Echo time
TR	Repetition time
UTE	Ultrashort echo time
WM	White matter

1 Introduction

1.1 Motivation

Gradient echo (GRE) based imaging techniques are well-known for their sensitivity to magnetic field inhomogeneity. Recent reports of GRE signal contrast within WM suggest that this contrast originates from differences in the underlying tissue microstructure [37, 38, 89].

However, the link between the actual tissue microstructure and the observed GRE signal behaviour is not well understood. In order to bridge this gap in knowledge, we explicitly modeled the underlying WM microstructure to obtain the whole magnetic field distribution from which a full repertoire of GRE signal behaviours can then be simulated. This geometric model provides a simple yet powerful way to investigate the effects of specific changes in WM microstructure on multiple aspects of GRE signal behaviour.

Specifically, we studied the dependence of GRE signal in WM on orientation to B_0. This relationship has been previously linked to the underlying WM microstructure but none of these studies have looked explicitly at the effects of WM microstructure and orientation dependence [11, 33].

We also studied the effects of myelination on GRE signal. The ability to infer myelination patterns from GRE signal would be helpful in understanding the progression of demyelinating diseases such as multiple sclerosis and to provide markers for recovery from such diseases.

1.2 Thesis overview

Chapter 2 : Basic concept of MRI The basic concepts of MRI are introduced here. This chapter begins with a discussion of the phenomenon of nuclear magnetic resonance which is responsible for generating the signal measured in MRI before moving on to how image formation occurs in MRI. The GRE sequence will be introduced here together with a brief discussion about GRE signal behaviours (e.g. signal magnitude decay and phase evolution).

Chapter 3 : White matter microstructure and magnetic susceptibility This chapter deals with white matter microstructure and its link to susceptibility contrast. We start with a brief description of white matter microstructure, and move on to myelin changes that can happen in the white matter. A short review of MR techniques used to study myelination is then given. Special focus is then given to the concept of magnetic susceptibility.

Chapter 4 : Geometric model of white matter The geometric modeling of white matter microstructure is discussed. A phantom study was used to validate the use of geometric modeling to simulate the GRE signal changes. The 2D geometric WM model is introduced here. This is followed by discussions about the various components of the model.

Chapter 5 : B_0 orientation effects In this chapter, we look at the relationship between GRE signal in WM with WM fiber orientation to B_0. We performed a study that correlates orientation information from WM pixels obtained from DTI to GRE signal in healthy human volunteers at 3T. The experimental GRE signal trends were then compared with simulated GRE signals

using the geometric WM model.

Chapter 6 : Myelin effects In this chapter, the effect of myelination on GRE signal at 7T will be investigated using the cuprizone mouse model. We first correlated GRE signal behaviours(e.g. resonance frequency and R_2*) with histological measures of myelination. We also investigated the longitudinal changes in GRE signal of mice undergoing demyelination and subsequent remyelination. The geometric WM model was then used to create hypothetical scenarios of demyelination to predict the corresponding GRE signal changes.

Chapter 7 : Conclusion This final chapter will summarize the work performed in this thesis. This chapter will also discuss possible improvement to the existing work and also the future direction of the work.

This is a blank page.

2 Basic concept of MRI

This chapter discusses some of the basic concepts of magnetic resonance imaging (MRI). We begin with a discussion about the phenomenon of nuclear magnetic resonance (NMR) which forms the underlying basis for the signal measured in MRI. We will then show how this NMR signal can be spatially localized in MRI to create images. The multi-echo GRE sequence that was used in the various studies in this thesis will also be introduced. The relationship between the underlying frequency distribution and the GRE signal characteristics will be discussed last.

2.1 NMR

Any introduction to MRI will usually begin with the phenomenon of NMR which was first observed in 1946 by Purcell [127] and Bloch [16] separately.

2.1.1 Nuclear spin

Subatomic particles possess an intrinsic angular momentum called spin. Spin is a purely quantum mechanical phenomenon that is quantized and has a value of 1/2 for many nuclei. The spin within a nucleus is the net total of the individual spins from the component subatomic particles. These spins tend to pair up and thus only nuclei with odd number of protons or neutrons will generate a net angular momentum. The hydrogen nucleus with a single proton has a net angular momentum and due to its abundance in the human body (e.g. in the form of water molecules H_2O) is the most investigated nuclei in MRI.

2.1.2 Precession

A proton can be thought of as a rotating positive charge which creates its own magnetic moment. The hydrogen nucleus thus behaves like a minuscule magnet with its poles parallel to the spin axis. In the presence of an external magnetic field, a torque is produced on the hydrogen nucleus that would rotate the magnetic moment such that its poles are in alignment with the external field. However, due to the angular momentum of the hydrogen nucleus, the nucleus does not align with the external field but instead precesses around the field axis (Fig. 1).

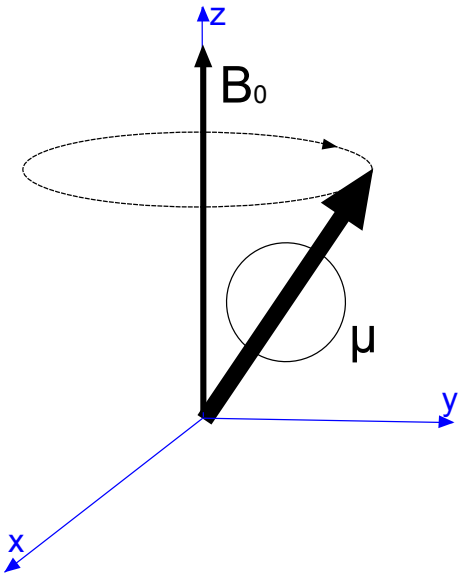

Figure 1: *A proton with angular momentum μ precessing about the direction of the main magnetic field B_0*

This motion is analogous to that of a spinning top whose spinning axis is tilted away from the vertical. Gravity applies a torque to tip the spinning top over but because of its angular momentum, the spinning top precess around the vertical axis at a constant angle to the horizontal instead. The precession frequency of the nucleus is called the Larmor frequency or the resonance frequency

(ω_0) and is related to the magnetic field strength (B_0) by the gyromagnetic ratio (γ). This relationship is given in the following equation:

$$\omega_0 = \gamma B_0 \tag{1}$$

The gyromagnetic ratio of a few commonly used nuclei are shown below:

Nucleus	γ *(MHz/T)*
^{1}H	42.6
^{13}C	10.7
^{19}F	40.1
^{23}Na	11.3
^{31}P	17.3

Table 1: *Gyromagnetic ratio of common nuclei in NMR*

2.1.3 Magnetization

In reality, we do not look at an individual spin but an ensemble of spins. In the absence of a strong external magnetic field, the magnetic moment has no preferred orientation such that a collection of spins are randomly oriented to one another and thus creates no net magnetization (Fig. 2). In the presence of an external magnetic field B_0, spins have a slight tendency to align themselves with the direction of the field (without increased tendency to point in any other orientation e.g. opposite the field) to produce a net magnetization M_0 pointing in the direction of B_0 field [58]. The axis parallel to B_0 is normally denoted as the longitudinal axis and the plane orthogonal to the longitudinal axis is known as the transverse plane.

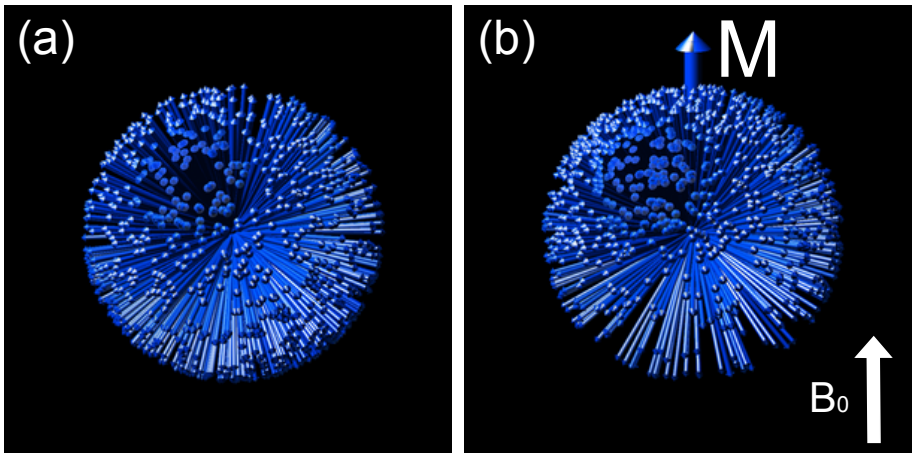

Figure 2: *Net magnetization (a) In the absence of an external magnetic field , magnetic moments are randomly oriented with no net magnetization. (b) In the presence of an external magnetic field, slightly more magnetic moments point towards B_0 resulting in a net magnetization. Diagrams courtesy of Dr. Karla Miller adapted from Hanson [58].*

2.1.4 Excitation

In the presence of an external magnetic field B_0, a net magnetization M_0 is created. The magnetic field produced by M_0 is many orders of magnitude weaker than B_0 and is thus undetectable in the B_0 direction. On the other hand, magnetization in the transverse plane is detectable. Radio frequency (RF) pulses are used to tip magnetization from the longitudinal axis onto the transverse plane to produce an observable, time dependent signal. This RF pulse is effectively a second magnetic field (B_1) which oscillates at the Larmor frequency in the transverse plane. Despite this magnetic field being many orders of magnitude smaller than B_0, the resonance condition ensures efficient transfer of energy to tip M_0 into the transverse plane. An analogy is that of pushing a swing. If the pushing frequency matches the swinging frequency, a small periodic force can eventually produce a large displacement of the swing. On the other hand, if the pushing frequency does not match

the swinging frequency, a much larger force would be required to produce an equivalent displacement. When the equilibrium magnetization M_0 is tipped into the transverse plane, any component of the magnetization in the transverse plane also precesses at the Larmor frequency. The amount of excitation for a hard pulse (i.e. the angle between magnetization vector and the z-axis) is dependent on the strength of the RF magnetic field B_1 and the duration of the pulse t_p and is given by Eqn. 2.

$$\alpha = \gamma B_1 t_p \tag{2}$$

Rotating frame of reference It is helpful to introduce the concept of the rotating frame of reference which is often used to simplify the description of magnetization in a NMR experiment [108]. By defining the rotating frame of reference as a frame rotating at the Larmor frequency about the z axis (i.e. direction of B_0), it can be seen that magnetization precessing at the Larmor frequency is stationary with respect to rotation about the z axis (Fig. 3). In the rotating frame of reference for excitation, B_1 simply tips M_0 away from the z-axis.

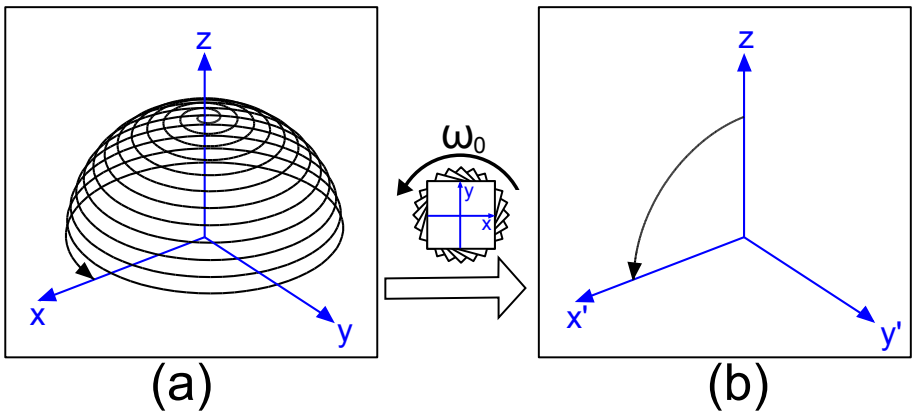

Figure 3: *Rotating frame of reference. (a) Trajectory of precessing (ω_0) magnetization as it is rotated by 90° onto the xy plane. (b) Trajectory of same magnetization in a rotating frame of reference.*

2.1.5 Relaxation

After excitation, relaxation returns the excited magnetization back to equilibrium and is described by two different time constants. T_1 describes the regrowth of the longitudinal magnetization while T_2 describes the loss of transverse magnetization . T_1 relaxation is also called the spin-lattice relaxation in which the spin system loses the extra energy from the RF excitation to the surrounding 'lattice'. T_2 relaxation is also known as the spin-spin relaxation in which decay of transverse magnetization is caused by the loss of phase coherence among spins due to random fluctuations of local magnetic fields at the molecular scale. This decreasing transverse magnetization causes signal loss. Another source of signal loss can occur when spins dephase under the presence of static magnetic field inhomogeneity and this is called T_2' decay. The main difference between T_2' and T_2 is that signal loss from T_2 is irrecoverable but signal loss from T_2' is recoverable (e.g. using a spin echo sequence). The loss of transverse magnetization due to T_2 and T_2' is given by the apparent transverse relaxation time (T_2*) and their relationship is given by :

$$1/T_2^* = 1/T_2 + 1/T_2'. \tag{3}$$

2.1.6 Bloch Equation

The behaviour of magnetization in a NMR experiment can be described by a single differential equation, which was first described by Felix Bloch [16] and is given by:

$$\frac{d\mathbf{M}}{dt} = (\gamma \mathbf{M} \times \mathbf{B}) - \frac{M_x\hat{x} + M_y\hat{y}}{T_2} - \frac{M_z\hat{z} - M_0}{T_1} \tag{4}$$

where $\mathbf{M} = [M_x M_y M_z]^T$ is the magnetization, $\mathbf{B}$ is the total magnetic field, M_0 is the equilibrium magnetization (which lies along the z axis) and T_1 and T_2 are the longitudinal and transverse relaxation times respectively. The above differential equation can be easily solved to give the following solutions corresponding to the time dependent configuration of the components of the magnetization along the three axes.

$$M_x(t) = (M_x(0)cos\omega_0 t + M_y(0)sin\omega_0 t) \cdot exp\left(\frac{-t}{T_2}\right) \tag{5}$$

$$M_y(t) = (M_y(0)cos\omega_0 t - M_x(0)sin\omega_0 t) \cdot exp\left(\frac{-t}{T_2}\right) \tag{6}$$

$$M_z(t) = M_0 + (M_z(0) - M_0) \cdot exp\left(\frac{-t}{T_1}\right) \tag{7}$$

where $\omega_0 = \gamma B$

2.1.7 Free induction decay

After excitation, the precessing magnetization produces a time varying magnetic field. This induces a voltage in a receiver coil to produce a measurable NMR signal which is proportional to the strength of the precessing magnetization. The signal gradually decays and is called the free induction decay (FID). This FID follows a T_2* decay in the presence of static external magnetic field inhomogeneity. This FID can also be loosely referred to as gradient echo (GRE).

2.1.8 Spin echo

This brings us to the concept of spin echo (SE) [56] in which signal loss, caused by dephasing due to static external magnetic field inhomogeneity, can

be recovered with the use of a 180° pulse. Suppose that a spin isochromat (originally along the y-axis at time t=0) precesses with a constant angular velocity ω. From t=0 to t=T, the isochromat would have precessed by ωT. A 180° pulse about the y-axis then flips this spin isochromat about the y-axis such that at t=T+δt the angle between the spin and the y-axis is -ωT. From t=T+δt to t=2T, the spin isochromat would precess by the same amount ωT which puts the spin isochromat back at the same location along the y-axis as t=0. This happens for any spin isochromat undergoing a constant precession resulting in the formation of a spin echo at t=2T. In contrast, for GRE, the same isochromat would have precessed by an angle of 2ωT during the same period. The inability to reverse such dephasing effects makes GRE sensitive to magnetic field inhomogeneity.

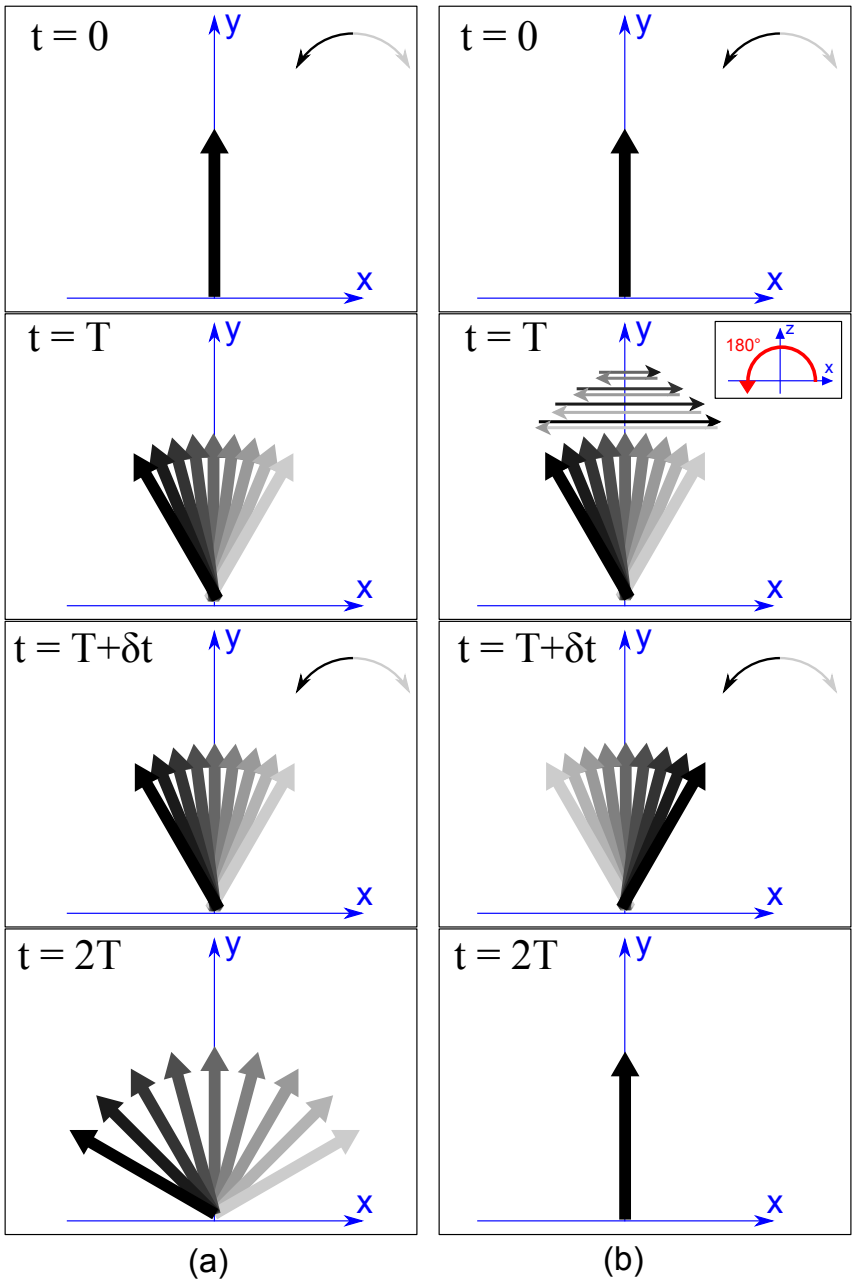

Figure 4: *Gradient echo vs spin echo. (a) GRE scenario. (b) SE scenario. Consider a collection of spin isochromats originally in phase at time t=0. In the presence of static magnetic field inhomogeneity, spin isochromats undergo constant dephasing. At t=T, a 180° pulse is applied in the SE case such that isochromats are flipped about the y axis at t=T+δt. The isochromats continue to precess at the same speed and at t=2T, isochromats in SE would have completely rephased but isochromats in GRE are dephased.*

2.2 MRI basics

2.2.1 Spatial localization

MRI is essentially a NMR spectrometer with signal localization capability. This capability comes from a set of magnetic fields more commonly known as gradients. MRI scanners normally have 3 sets of gradient coils G_x,G_y and G_z that create a linearly changing magnetic field aligned to B_0 along x,y and z axes according the following equation

$$B(\mathbf{r}) = B_0 + \mathbf{G} \cdot \mathbf{r} \tag{8}$$

where $\mathbf{r} = [x, y, z]^T$ is the spatial location and $\mathbf{G} = [Gx, Gy, Gz]^T$ is the gradient field vector. By varying the local magnetic field according to its location in space, the resonance frequency (since $\omega(\mathbf{r}) = \gamma B(\mathbf{r})$) at different spatial locations can be varied thus allowing signal to be localized.

2.2.2 Image formation

In the absence of any gradient field, the MR signal detected from an object comes from the sum of magnetizations present at different locations $\mathbf{M}(\mathbf{r})$ and is given by

$$s(t) \;=\; \int \mathbf{M}(\mathbf{r}) d\mathbf{r} \tag{9}$$

where $\mathbf{M}(\mathbf{r}) = \rho(\mathbf{r}) exp(i\theta(\mathbf{r}))$, $\rho(\mathbf{r})$ is the magnetization density at $\mathbf{r}$ and $\theta(\mathbf{r})$ is the local phase angle due to precession at the local resonance frequency. The magnetization density is a function of proton density (PD) and time (due

to relaxation) while $\theta(\mathbf{r})$ is also a function of time. These dependences on time are important for generating different contrasts in images (e.g. T_1, T_2, PD weighting). In the present discussion, we are only concerned with the generation of an image corresponding to a specific time point (e.g. snapshot [20]) so we can temporarily neglect the time dependence of $\mathbf{M}(\mathbf{r})$.

In the presence of the gradient fields, the magnetization ($\mathbf{M}(\mathbf{r})$) at each position in space acquires an additional phase shift and the MR signal (demodulated at the Larmor frequency) can be expressed as

$$s(t) = \int \mathbf{M}(\mathbf{r}) exp(i\gamma \int_0^t \mathbf{G}(\tau).\mathbf{r} d\tau) d\mathbf{r} \tag{10}$$

where the extra exponential term represents the additional phase shift created by the gradient field at each location. By letting

$$\mathbf{k}(t) = \frac{\gamma}{2\pi} \int_0^t \mathbf{G}(\tau) d\tau \tag{11}$$

We can rewrite Eqn. 10 as below

$$s(t) = \int \mathbf{M}(\mathbf{r}) exp(i2\pi \mathbf{k}(t).\mathbf{r}) d\mathbf{r} \tag{12}$$

Eqn. 12 shows a Fourier relationship between the measured signal s(t) and the spatial frequency parameter $\mathbf{k}(t)$. By taking an inverse Fourier transform of the entire spatial frequency domain, an image of the spatial distribution of magnetization $\mathbf{M}(\mathbf{r})$ can thus be formed. The aim of a MRI experiment then is to read out the MR signal during the time course of gradients such that $\mathbf{k}(t)$ covers the whole spatial frequency domain, also referred to as the k-space. Different schemes of filling up the k-space exist and one of the most common is the cartesian k-space trajectory which will be discussed next.

2.2.3 MRI signal acquisition

A basic GRE sequence will be used here to demonstrate MRI signal acquisition. Fig. 5 shows a schematic (also known as pulse sequence diagram) that demonstrates how the GRE sequence is used to acquire signal.

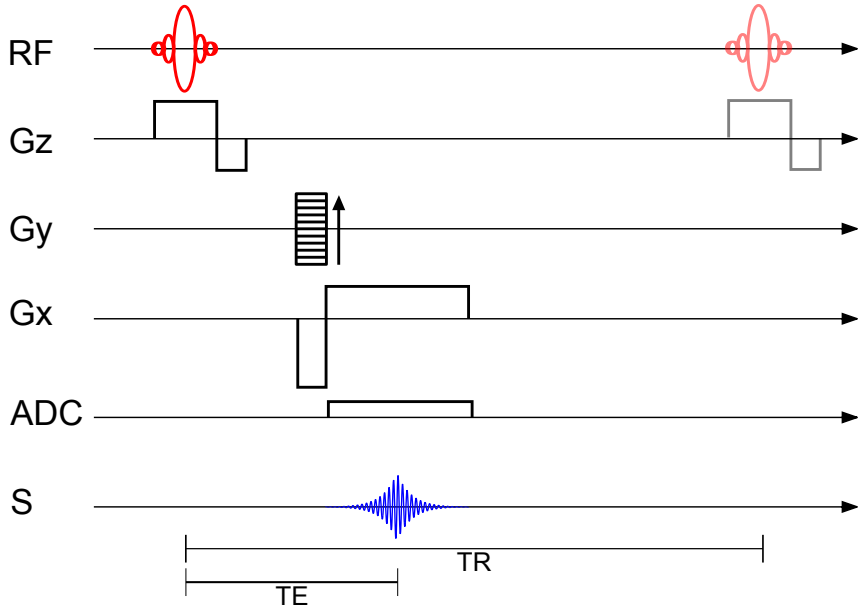

Figure 5: *Pulse sequence diagram of a basic GRE sequence. It consists of a radio frequency (RF) pulse that is used for excitation of magnetizations. 3 sets of gradients Gz,Gy and Gx are used for signal localization. TR is the repetition time. For each TR, the value of Gy is altered. TE is the echo time between the time of excitation and signal acquisition. ADC is the analogue to digital converter which transform the measured induced current in the receiver coil into digital signal.*

The first step of signal acquisition is normally to localize the signal from a single slice or slab. This is achieved by applying a gradient field (G_z) along the z direction such that there is a varying magnetic field along the z direction. The resonance frequency is then given as a function of location along the z axis (Fig. 6).

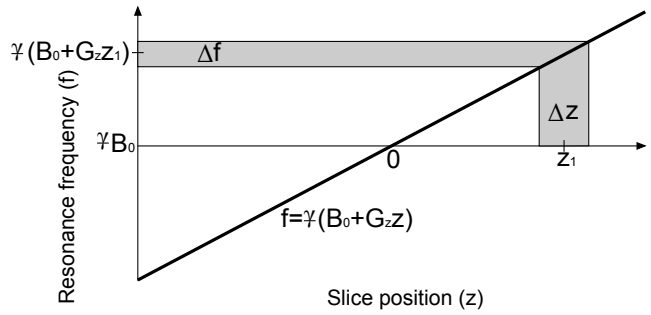

Figure 6: *Effects of the slice selection gradient on resonance frequency. The resonance frequency is a function of location along the z axis and can be used to spatially excite magnetizations along z.*

Next, we apply an RF pulse to excite a specific range of frequencies (Δf). The selected range of frequencies will determine the position (z_1) and thickness (Δz) of the slice selected. Only spins in that selected slice will be excited and thus only signal from the selected slice will be detected subsequently. Due to the presence of a distribution of frequencies within a slice because of the linearly varying gradient field, there is a need to rephase the excited spins. This is achieved by applying another gradient lobe of opposite polarity but with half the area under the lobe such that the dephased spins are fully rephased by the rephasing gradient.

After slice selection, we spatially encode the x and y direction using gradients in the x and y directions. We can view the effects of these gradients as a means to fill up k-space (remember that the inverse Fourier transform of k-space gives the MR image which we are interested in) in which a series of gradients along the x and y axis are applied to move through k-space (e.g. k-space trajectory) such that the entire 2D k-space can be sampled. It can be seen from Eqn. 11 that shifting can be accomplished by changing the gradient and/or the duration of the gradient (i.e. area under the gradient at a specific time which represents the amount of dephasing imparted onto the isochromats).

We look specifically at how the basic GRE sequence samples the entire k-space using a Cartesian trajectory (Fig. 7). Upon the excitation of the magnetization, the k-space trajectory starts at the middle of k-space. A gradient in the y direction (commonly known as the phase encoding gradient) is applied for a short period of time and then switched off. On the k-space, the effect of applying the phase encoding gradient is to shift k-space along the ky direction and the trajectory will remain in the same ky row after switching off Gy. In the x direction, a prephasing gradient is applied to shift k-space in the negative kx direction, after which, another gradient called the readout gradient with opposite polarity and double the gradient area is applied together with the ADC and signal is sampled to fill up a single row of k-space. A gradient echo is formed at the middle of the readout gradient which corresponds to the point at which the readout gradient cancels out the effects of the prephasing gradient.

An implementation that uses the cartesian k-space trajectory is demonstrated here. In the first TR, the most negative phase encoding gradient is applied together with the negative prephasing gradient to shift the k-space trajectory to the bottom left hand corner. The phase encoding gradient is switched off and the readout gradient is then switched on together with the ADC to sample a single row of k-space. On the next excitation, the k-space trajectory again starts from the middle of k-space and with a slightly less negative phase encoding gradient, a new line of k-space above the previously filled one is filled during the frequency readout. The process continues until the required k-space is filled up.

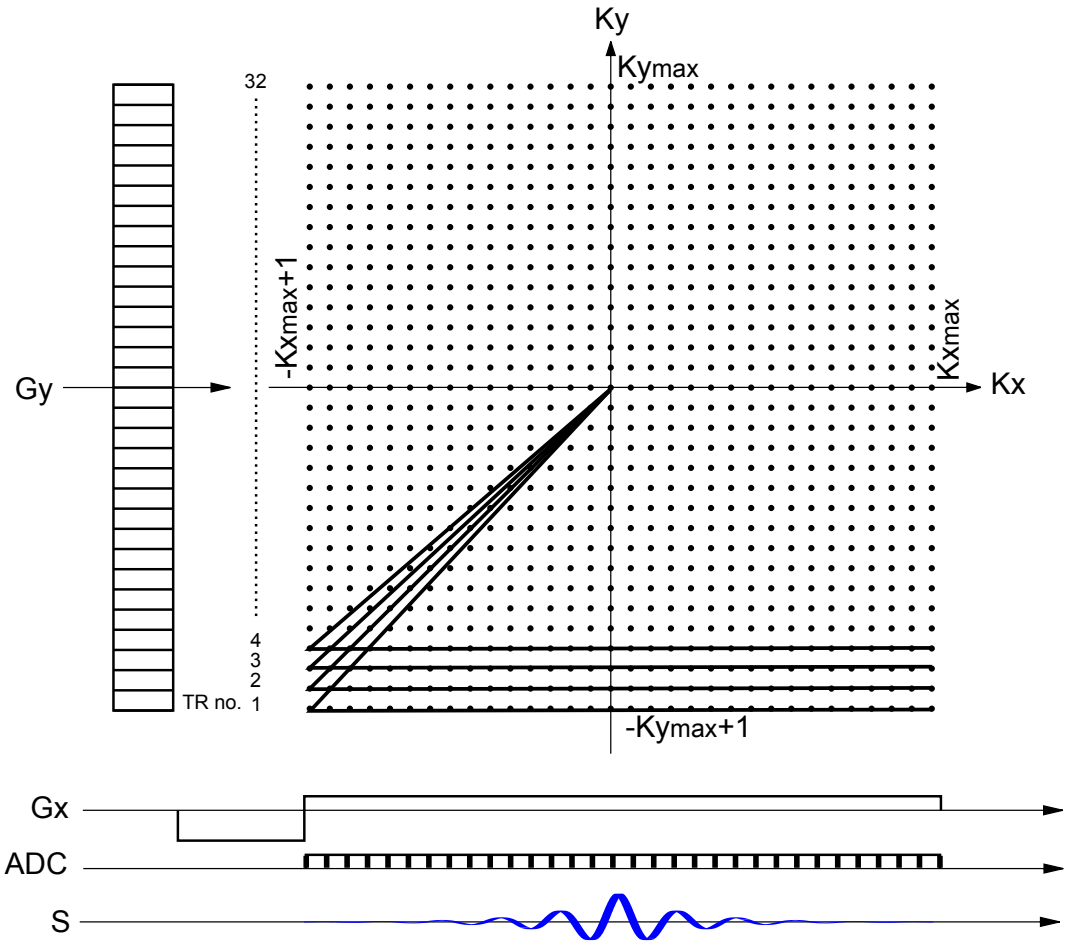

Figure 7: *Cartesian k-space trajectory. The dots represent the discrete k-space coordinates. The first TR with the most negative phase encoding gradient coupled with the negative prephasing gradient pushes the k-space trajectory to the bottom left hand corner. During signal readout, one row of k-space is filled from left to right. On the next excitation, the k-space trajectory again starts from the middle of k-space and with a slightly less negative phase encoding gradient, a new line of k-space above the previously filled one is filled during signal readout. The process continues until the required k-space is filled up. (Gradients are not drawn to scale)*

2.2.4 2D multi-echo GRE

The 2D multi-echo GRE pulse sequence is used extensively in this thesis and is adapted from the basic GRE sequence discussed previously. The main difference lies in the acquisition of multiple echoes during each TR through the use of multiple pairs of bipolar gradients that consecutively dephase and rephase the magnetization to enable sampling of the GRE signal over time. Another addition is the crusher gradients (red boxes in Fig. 8) towards the end of the TR that serves to dephase any remaining net magnetization in the transverse plane. This process is called gradient spoiling and is used together with RF spoiling which adds a (n+1)*117° phase to the following RF pulse to further ensure that no coherence is built up by remnant magnetization in the transverse plane [12]. The complex GRE signal obtained at each TE can then be used to characterize the GRE signal.

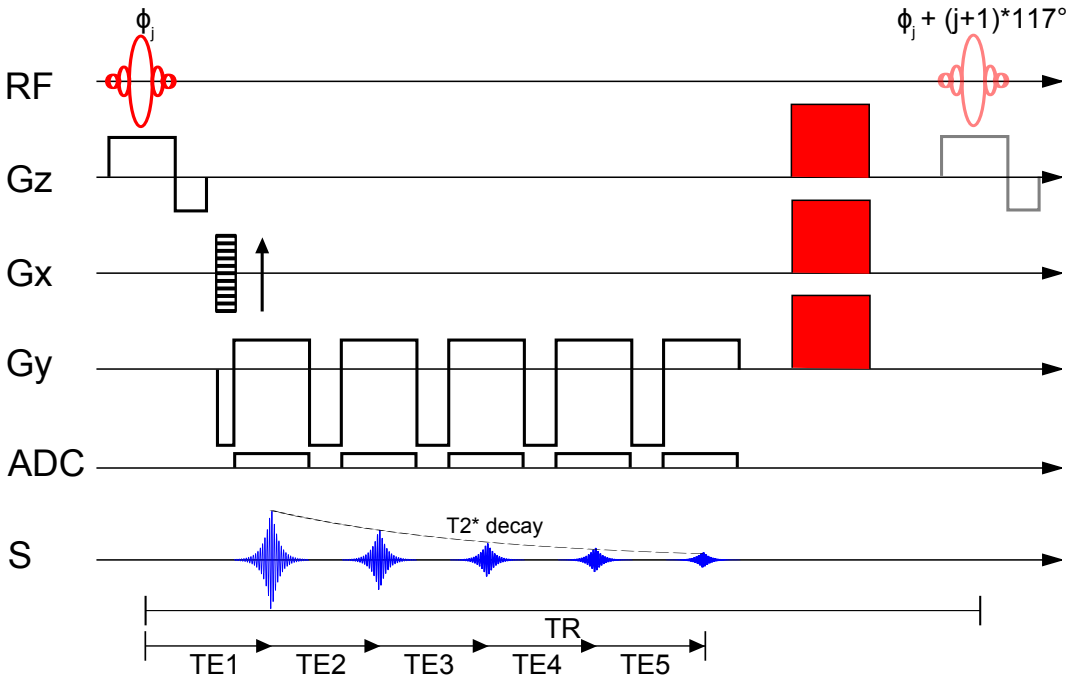

Figure 8: *Pulse sequence diagram of a multi-echo gradient echo sequence. The decrease in signal magnitude in each subsequent echo is due to* T_2^* *decay.*

2.3 Frequency distribution and GRE signal

The basic effect of a frequency distribution is to cause spin isochromats to go out of phase with one another such that there is an overall reduction in the net magnetization. Specifically, the width of the frequency distribution affects the decay of the transverse magnetization magnitude and the mean of the frequency distribution affects the phase of the net transverse magnetization. To visualize these effects, consider 3 different frequency distributions (each denoted by a different color, as shown in the frequency histogram in Fig. 9(a)). The effects of T1 and T2 relaxation of the isochromats are assumed to be negligible in this illustration.

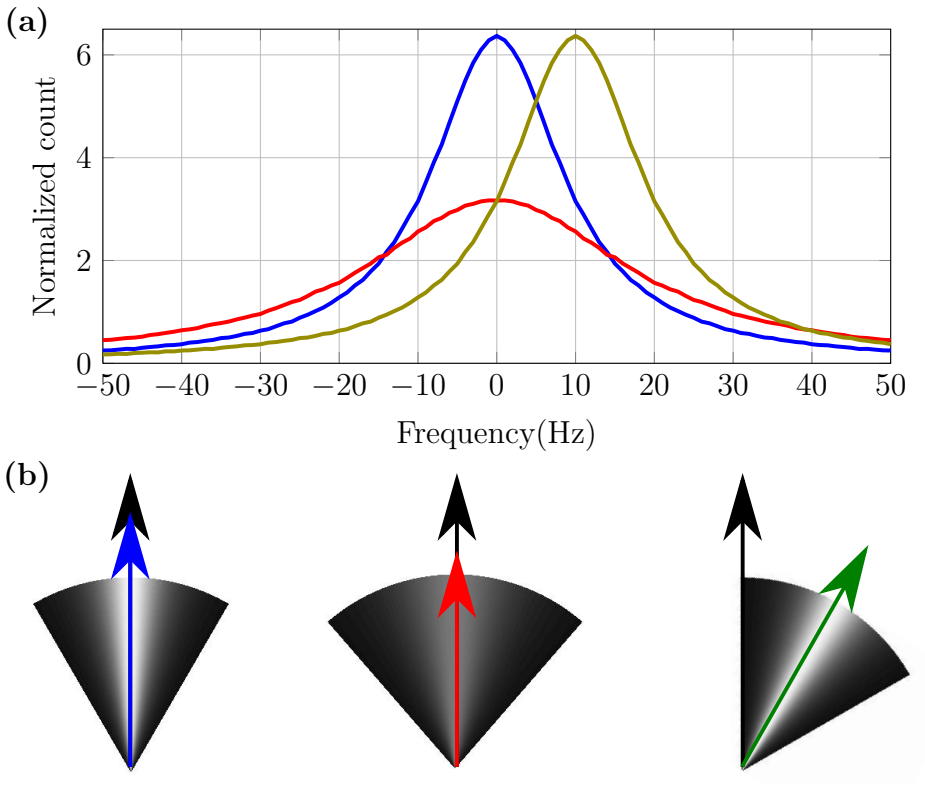

Figure 9: *Effects of frequency distribution on transverse magnetization. (a) shows the frequency histograms of 3 different frequency distributions. (b) shows the distribution of isochromats at an arbitrary time t for the 3 frequency distributions. Black arrows indicate the original net transverse magnetization and the blue, red and green arrows correspond to the net transverse magnetization at time t.*

The distribution of spin isochromats after signal dephasing (as dictated by the frequency distribution) at an arbitrary time t is displayed in a fan plot whereby the intensity indicates the population of isochromats at a particular phase and the coloured arrows represent the effective net transverse magnetization. After time t, all the net transverse magnetization can be seen to decrease (i.e. shorter colored arrows compared to the black arrows) as a result of isochromats going out of phase with one another. The red distribution, which has a wider frequency distribution than the blue distribution, demonstrates a larger fanning out of the phase of the isochromats thereby resulting in a smaller sig-

nal magnitude. The green distribution which has the same width but different mean of frequency distribution shows an identical amount of fanning out of isochromats as the blue distribution but the phase of the net magnetization is shifted due to the difference in their mean frequency.

It is useful to formulate the relation between the frequency distribution and the resultant net signal evolution with time (due only to the effects of dephasing caused by the frequency distribution and ignoring other relaxation effects). For a given frequency distribution $P(f)$, which represents the population of isochromats, the net signal evolution $S(t)$ is given by the integral of the signal evolution of each isochromat weighted by the frequency distribution and can be written as below

$$S(t) = \int P(f) exp(i2\pi ft) df = \mathcal{F}^{-1}\{P(f)\} \tag{13}$$

where $exp(i2\pi ft)$ is the signal evolution of an isochromat (ignoring the effect of relaxation and proton density). This equation implies a Fourier relationship between the net signal evolution and the underlying frequency distribution. Assuming a Lorentz shaped frequency distribution

$$P(f) = \frac{1}{\pi}\left[\frac{\Gamma}{(f-f_0)^2 + \Gamma^2}\right] \tag{14}$$

where f_0 is the median frequency and Γ is the half-width at half-maximum (HWHM). If we substitute Eqn. 14 into Eqn. 13, we get an exponential function which is the Fourier pair of the Lorentz distribution

$$S(t) = exp(i2\pi f_0 t - \Gamma t) \tag{15}$$

where

$$|S(t)| = exp(-\Gamma t) \quad (16)$$

$$\phi(t) = \angle S(t)$$

$$= 2\pi f_0 t \quad (17)$$

From Eqn. 16, it can be seen that the signal magnitude follows an exponential decay with the decay rate directly proportional to the width of the frequency distribution. From Eqn. 17, signal phase evolution is seen to be determined by the mean (median for a Lorentz distribution) frequency.

2.3.1 GRE signal parameters

GRE signal magnitude decay and phase evolution are characterized by T_2* and resonance frequency respectively. The extraction of the parameters T_2* and resonance frequency from GRE magnitude and phase data reduces the confounding factors of spin density, T_1 and RF coil sensitivity variations associated [37] with magnitude and phase images and allows for more robust quantification of the tissue properties.

T_2* decay GRE signal magnitude decay follows the following equation

$$|S(t)| = |S(0)|exp(-t/T_2^*) \quad (18)$$

where |S(t)| is the measured signal magnitude at time t and T_2* is the apparent transverse relaxation time. In order to find T_2* , GRE signal magnitudes of at least 2 time points (e.g. TE1 and TE2) are used in a linear fit of the log of

the signal magnitude (Eqn. 19). Multiple time points can generally be used in the linear fit to obtain a better estimation of T_2* .

$$T_2^* = \frac{TE1 - TE2}{log(|S(TE2)|) - log(|S(TE1)|)} \tag{19}$$

T_2* decay is actually a combination of T_2 and T_2' decays. T_2 decay is the spin-spin relaxation that was discussed previously and T_2' represents additional dephasing of the underlying spins by the presence of static magnetic field inhomogeneity (e.g. the frequency distributions in Fig. 9a) and it is this T_2' that is directly associated with the underlying frequency distribution. Thus, T_2* is related to the width of frequency distribution i.e. the 2nd moment of the frequency distribution. It is sometimes more convenient to refer to the apparent transverse relaxation rate R_2*, where $R_2^* = 1/T_2^*$.

Resonance frequency The GRE phase changes according to the following equation :

$$\phi(t) = 2\pi f t \tag{20}$$

where $\phi(t)$ is the measured signal phase at time t and f is the resonance frequency. The resonance frequency can be obtained from at least 2 time points by fitting a linear equation and obtaining the gradient (Eqn. 21). Multiple time points can be linearly fitted to get a more accurate estimation of the resonance frequency.

$$f = \frac{1}{2\pi} \cdot \frac{\phi(TE2) - \phi(TE1)}{TE2 - TE1} \tag{21}$$

The resonance frequency measures the mean of a frequency distribution i.e. the 1st moment of the frequency distribution.

Brain tissues in general are expected to display the above mentioned signal

characteristics but deviations from mono-exponential T_2* decay and linear phase evolutions have been experimentally observed in WM. These deviation behaviours will be one of the topics brought up in the course of this thesis.

3 White matter microstructure and magnetic susceptibility

White matter microstructure is highly complex, consisting of various cellular structures that are in turn made up of different biological materials (e.g. lipids, proteins) that have different chemical and physical properties such as magnetic susceptibility. This can create mesoscopic magnetic field inhomogeneities that affect the behaviour of GRE signal, thus making GRE sensitive to WM microstructure. Studies have suggested myelin to be one of the major contributors to the observed susceptibility contrast [83, 92].

We begin this chapter by giving a brief overview of WM microstructure before turning our focus to myelin changes followed by a short review of MR techniques used to study myelination. Special attention is then given to the concept of magnetic susceptibility.

3.1 White matter microstructure

WM is highly heterogeneous and is made up of a wide variety of cellular structures belonging to cells that can be broadly classified as neuronal or glial [120]. These cellular structures have unique physical and chemical properties that allow them to work together to allow the WM to perform its function.

Long thin projections known as axons extend from the neuronal bodies present in the gray matter into the white matter. These axons can be thought of as wirings for the conduction of electrical signal that connect the different brain regions allowing them to communicate with one another. During signal transduction, an action potential is first started at the initial unmyelinated

segment of the axon [120]. This action potential will then have to travel along the entire length of the axon to reach its target. This current is relayed via movement of ions through the sequential opening of sodium and potassium ion channels [64]. In the absence of any insulating membrane, substantial current loss occurs due to leaks and charging of the membrane to alter the membrane potential. Since the conduction velocity of unmyelinated axons is directly proportional to their diameters [52, 59], the size of the axons would be excessively large in order to achieve rapid propagation of electrical impulses. To increase the speed of signal transmission without the need to increase axonal diameter, most axons are wrapped around by myelin sheaths, which provide electrical insulation to the axon [120].

Myelin is composed of about 70% lipids and 30% proteins [154] unlike most biological membranes that have a higher ratio of proteins to lipids. Each myelin layer is composed of two layers of lipids to form a bilipid layer that is about 17nm thick [128]. The bilipid layer is wound around the long axonal axis multiple times to form the myelin sheath. The ratio of the myelin thickness to the axonal diameter (or the more widely used definition of g-ratio which is the ratio of the axon diameter to the entire fiber diameter) is tightly regulated in the brain. A g-ratio of between 0.6 to 0.7 is commonly reported in both simulations and experiments and this has been shown to correspond to the maximum conduction velocity achievable for a fixed axonal diameter [70]. The myelin sheaths significantly reduce the loss of current by acting as insulators to current leak across the membrane and by reducing the capacitance of the membrane [107]. Myelin sheaths do not continuously cover the entire length of the axon but form segments along the axon separated by small unmyelinated gaps called nodes of Ranvier. These nodes contain a very high concentration

of sodium channels acting as booster stations to propagate the signal to the next node [21]. This process is also known as saltatory conduction and is responsible for the fast conducting speed of 100-120ms^{-1} in myelinated axons compared to the speed of 25ms^{-1} in the unmyelinated squid axon [65].

Interspersed between these axons are various types of glial cells. Unlike neuronal cells, glial cells do not directly conduct electrical signals and have long been overlooked as a 'brain glue' or 'gap filler' that hold the more important axons together within the white matter [42]. These cells however do play important supporting roles for the normal functioning of the axons. One of the most abundant are the star-shaped astrocytes with their many long fiber-like processes that extend to blood vessels and nodes of Ranvier [144]. They were originally thought of as passive cells that provide mechanical support for the axons. However, there is evidence that they are also responsible for neural transmitter secretion and absorption. Also present are oligodendrocytes that are responsible for the production and maintenance of the myelin sheaths [29], as well as microglial cells that function as macrophages responsible for the autoimmune defence within the brain [5]. Blood vessels run through the WM providing the various cells with essential nutrients.

3.2 Myelin changes

Myelin changes can occur throughout a human lifetime. Myelination begins in the spinal cord 12 to 14 weeks after gestation [161]. From mid gestation to the end of the second postnatal year, myelination is believed to account for the almost tripling of the weight of the brain [72]. Myelination continues throughout childhood, adolescence and into adulthood with the final maturation of

the intracortical fibers of the cerebral cortex after some 30 years [173]. Myelin changes are not just restricted to development. For instance, some studies have found evidence of activity-dependent myelin plasticity in both humans and rodents [41]. Myelin then starts to degenerate during the aging process resulting in widespread damage to the myelin sheaths. In the aging rhesus monkey brain, the amount of damage to the myelin sheath correlates strongly with a decline in the cognitive status of the animals suggesting that myelin breakdown reduces conduction velocity in the affected nerve fibers [121].

Myelin integrity can be affected in diseases. Since myelin ensures the proper transmission of signal between brain regions, it can be seen that disruptions in the myelination of axons can have serious consequences. Two main classes of myelination diseases can be identified based on the mechanism for myelin pathology [97]. In the first class, there is a failure to form normal myelin and this is termed as dysmyelinating disorders. They are mainly caused by genetic factors, and can also result from environmental influences such as iodine deficiency that can lead to hypothyroidism and associated myelination failure [159]. Krabbe disease is an example of dysmyelination disease caused by genetic mutation resulting in a deficiency of the lysosomal enzyme galactosylceramidase which is responsible for metabolizing lipids. The accumulation of un-metabolized lipids disrupts the formation of normal myelin sheath and causes severe motor deficits leading to death [149].

The second class of myelination diseases is known as demyelinating disorders in which normal myelin is destroyed. The most widely studied demyelination disease is multiple sclerosis. Multiple sclerosis (MS) is a chronic, inflammatory and often incapacitating immune-mediated disease in which the body's own immune system attacks the myelin sheaths covering the white matter axons

[116]. MS accounts for the majority of non-traumatic disability among young adults with enormous socioeconomic impact in developed countries [36]. It is estimated that 2.5 million people worldwide are affected by MS [162].MS is a highly heterogeneous disease in which the symptoms, time courses and severity differ from person to person, depending mainly on the locations of the lesion sites [77]. Despite decades of extensive research, the origin of the disease is unknown and there is currently no effective cure for MS with treatment targeted mainly at mitigating symptoms and slowing down the progress of the disease [19].

A third class of myelination disorder may be identified as hypermyelination in which there is excess myelination surrounding a given axon. Hypermyelination is often focal and observed together with regions of hypomyelination, for instance the Charcot-Marie-Tooth (CMT) disease [130].

3.3 Animal models of myelin deficiency

Myelin pathologies are widely studied in both humans and animal models. There exists a variety of animal models that have been used and similar to the classification of myelin deficient diseases, animal models can also be largely grouped into dysmyelination and demyelination models.

The shiverer mouse is a classic dysmyelination animal model [73]. The shiverer mouse model is caused by mutations of the myelin basic protein gene. Myelin basic protein is essential for the formation of compact myelin. Shiverer mice are characterized by incomplete myelin formation in the CNS in which the myelin sheaths are mostly absent or are very thin and loosely packed around normal axons [174]. The absence of axonal damage and inflammation makes

the shiverer mouse model a good choice for the study of the effects of myelination.

The cuprizone mouse model is a toxicity induced demyelination model [106]. The introduction of cuprizone into the diet of young mice causes acute demyelination with complete demyelination observed after 6 weeks. The time course, location and extent of the demyelination are all highly reproducible, making this an attractive model to study the effects of demyelination. Both mouse models have been previously used to study the effects of myelination on GRE signal [83, 92, 93]. In our study, we were primarily interested in inducing different degrees of myelination within the WM and the cuprizone model provides an excellent platform to achieve this.

3.4 MR techniques to study myelination

Various MR techniques have been used to probe myelination in white matter. These include conventional methods such as $T_1$and T_2-weighted imaging, and more advanced techniques such as magnetization transfer (MT) imaging and ultrashort TE (UTE) imaging. Most of these techniques look at the effects of myelin indirectly (e.g. T1,T2, MT) while some attempt to look at myelin directly (e.g. UTE). In this section, we introduce some of the MRI techniques that have been used to study myelination in white matter.

Conventional T_1,T_2 T_1 and T_2 relaxation times in WM have been linked to the amount of myelination in WM. Since myelin water has a short T_1 and T_2, the increase in myelination has been hypothesized to bring about the shortening of T_1 and T_2 relaxation times. This causes WM to change from

hypointense to hyperintense with respect to gray matter (GM) in T_1-weighted images and vice versa in T_2-weighted images [66]. In the clinic, T_1 and T_2-weighted images are used routinely to monitor normal brain maturation and mental development. T_1 and T_2-weighted images have also been used with success in the diagnosis of demyelination diseases such as MS [9, 46]. However, T_1 and T_2-weighted images are not only affected by myelination but also by other factors such as water content and thus lack specificity [112] to a given aspect of the neuropathology (e.g. inflammation vs demyelination). This is exemplified by the lack of success in using T_1 and T_2-weighted images in predicting the progression of disease in patients already diagnosed with MS [43].

Magnetization transfer imaging Magnetization transfer (MT) imaging techniques probe protons of macromolecules such as those belonging to large lipids present in myelin [61]. Under normal circumstances, MRI is only capable of imaging protons with sufficiently long T_2 (e.g. $> 10ms$), thus rendering imaging of protons of macromolecules with much shorter T_2 (e.g. $< 100\mu s$) impossible. However, interactions between the free pool of protons and the restricted pool of protons can be utilized to probe the restricted pool of protons. More specifically, there exists a coupling between the two pools of protons which allows the exchange of magnetization between macromolecular and fluid protons. The macromolecular protons have a much broader absorption lineshape compared with the fluid protons, which allows the macromolecular spins to be preferentially saturated with an off-resonance irradiation with a sensitivity of up to 10^6 [61]. This saturation of the macromolecular spins can then be transferred to the liquid spins via exchange. Taking the difference between images with and without off-resonance irradiation thus provides information

about the pool of macromolecular protons. Subsequent quantification of the relative size of the restricted proton pool, exchange and relaxation rates is possible with a two-pool model.

MT has been shown to be sensitive to myelin. Strong correlations have been reported between the derived restricted proton pool size and myelination observed in postmortem MS brains [134, 135] . MT parameters have also been shown to vary with different degree of myelination in the different WM fiber tracts of normal subjects and especially in very densely myelinated WM fiber tracts [143]. In MS, the derived restricted proton pool size decreases significantly in chronic lesions with a smaller but significant reduction in normal appearing WM [30]. The main disadvantage of using MT methods to study myelination is the partial specificity to myelin since protons belonging to other macromolecules such as proteins cannot be readily differentiated [86]. Another concern with the use of MT in MS is the sensitivity of MT to edema and inflammation since MT is also sensitive to changes in water content [124].

Multicomponent transverse relaxation Another method that has been proposed to look at myelin is multicomponent T_2 relaxation [100, 167, 168]. Unlike MT techniques that distinguish between the liquid and non-liquid constituents of the tissue, the multicomponent relaxation method looks at distinguishing different pools of liquid subpopulations. Two pools model of the WM have been proposed in which short T_2 species ($\approx$20ms at 3T) would represent myelin water while longer T_2 species ($\approx$70-90ms at 3T) would represent extra and intracellular water [79]. In a three-pool model of WM, the longer T_2 pool has also been subdivided into an intermediate T_2 myelinated axon water pool and a longer T_2 mixed water pool [76]. The resulting T_2 decay curve is thought

to be a summation of the different T_2 species weighted by their volume fraction. Thus, we can estimate the volume fractions and T_2 decay rates of each species by fitting a weighted sum of exponentials to a T_2 relaxation curve obtained from a multiecho spin echo sequence. The myelin water fraction (MWF) is computed as the volume fraction of the compartment with the smallest T_2 in both the two and three pools model. The general assumption of this method is that volume fraction of water trapped between the myelin layers is directly proportional to the actual amount of myelin present. Reduced MWF has been reported in lesions [100] as well as in normal appearing white matter (NAWM) in MS subjects [79]. An interesting observation is the reported lack of correlation between MT data and MWF [50] which demonstrates a need to further probe the underlying mechanism behind each measure.

More recently, multicomponent T_2* relaxation [35, 155] has also been investigated. It is based on the same premise of water compartmentalization leading to distinct water pools but is based on GRE sequences.The main advantages of T_2* contrast include the relatively strong contrast amplification and low power deposition of GRE (compared to SE sequences) at higher field strength. However, in multicomponent T_2*, there is a need to consider the frequency shift [155] that is experienced by the different water pools with respect to each other since this phase effect is not negated by GRE sequences as would be in a SE sequence. This increases the number of unknowns to be fitted in order to account for the frequency shifts between compartments. This has indeed been verified by a study by van Gelderen *et al.* [155] that showed that summation of multiple exponential T_2* relaxation curves with frequency shifts showed better fitting than multiple exponential curves without phase shifts.

Direct MR detection of myelin In a recent paper by Wilhelm *et al.* [170] , direct MR detection of myelin in situ and in reconstituted suspension of myelin lipid extract was demonstrated using ultrashort echo time (UTE) MRI methods. Direct imaging of myelin is hampered by its short T_2* (50-1000 μs [67]). UTE methods on the other hand allow the FID to be sampled almost immediately after excitation (e.g. $20\mu s$). When UTE is combined with the attenuation of long T_2* water signal using adiabatic inversion and complex echo subtraction, it has the ability to directly image myelin. This direct visualization of myelin is attractive especially since other methods such as MT and multicomponent relaxation measure indirect changes of myelin via the interaction of myelin with detectable water signals and are hence affected by non-myelin related changes, for example changes in other macromolecules in MT studies. This method is still in its infancy and translation of the technique would require improvements in the MR hardware, e.g. ability to produce very short duration RF pulses.

Magnetic resonance spectroscopy Proton magnetic resonance spectroscopy (MRS) can be used to detect changes in the concentration of important metabolites that can reveal pathology in the brain during demyelination events [44, 112, 125]. Choline resonance changes can reflect the breakdown of myelin and the subsequent release of choline containing membrane phospholipids and elevation of choline has been detected in both acute lesions [7] and pre-lesion normal appearing white matter (NAWM) [151]. Direct observation of lipids which are normally not detectable in MR spectra due to their restricted mobility in membranes becomes possible when they are released from membranes during demyelination [44]. N-acetylaspartate which is present only in neurons and processes in normal brain can be used to detect axonal injuries and loss

[48]. However, MRS techniques are often limited by several technical issues such as the acquisition of a single voxel (which may be rectified using chemical shift imaging), the relative long duration of acquisition time and low signal to noise ratio (SNR) [125].

Diffusion MRI Diffusion MRI is based on signal attenuation typically in the presence of a pair of bipolar gradients [80]. In the presence of the first dephasing gradient, the protons experience a local magnetic field that varies in strength along the gradient and begin to dephase with respect to each other. When the second rephasing gradient of the same strength but opposite in direction is applied, an opposite magnetic field is created which causes stationary protons to precess in the opposite direction and return to the original phase as before the first gradient. In the presence of Brownian motion, the moving protons do not experience the same magnetic field as the first gradient and incomplete rephasing occurs. This causes an attenuation of signal being measured. Since only displacement along the gradient direction can be detected, multiple measurements along different directions are normally acquired from which a diffusion tensor can be obtained. Various measures, such as mean diffusivity and fractional anisotropy, can then be obtained from the diffusion tensor (i.e. diffusion tensor imaging (DTI)). It is often enticing to directly relate the above scalar measures to pathology. For example, Song *et al.* [145] has proposed that radial diffusivity (obtained from the average of the second and third eigenvalues of the diffusion tensor) reflects myelin content. It was however pointed out by Wheeler *et al.* [166] that the link between radial diffusivity and the underlying tissue structure was an over-simplification and may not hold in various pathological scenarios.

3.5 Susceptibility-based GRE techniques

GRE based MRI techniques are sensitive to magnetic field inhomogeneities. Large scale magnetic field inhomogeneity is often associated with magnetic field distortions leading to image artefacts and signal dropouts e.g. imaging near metallic transplants [126]. On the other hand, mesocopic magnetic field inhomogeneity caused by tissue microstructures can provide unique contrast in GRE images. The recent popularity in magnetic susceptibility based contrast generated from GRE sequences is largely due to the amplification of contrast at higher field strengths [38]. From a GRE scan, both magnitude and phase images [53] can be used to probe the underlying tissue microstructure. The focus of this thesis is to look at the effects of WM microstructure on GRE signal behaviour and thus allow a better understanding of the link between actual tissue microenvironment and observed GRE signal characteristics.

3.5.1 Magnetic susceptibility

Magnetic susceptibility (χ) is a quantitative measure of a material's tendency to be magnetized in the presence of an applied magnetic field. The magnetized material then interacts with and distorts the applied magnetic field [133]. Most biological materials can be categorized into two main groups according to their magnetic susceptibility. Diamagnetic materials have negative magnetic susceptibility and are repelled by an external magnetic field (insignificant effects at low field strength) while paramagnetic materials have positive magnetic susceptibility and are attracted to an external magnetic field. It is also common to report the magnetic susceptibility of materials with respect to a reference such as pure water. Other forms of magnetism such as ferromagnetism exist but

are beyond our scope since they are uncommon in normal biological materials of the brain.

In diamagnetism, an applied external magnetic field changes the orbital motion of electrons. According to Lenz's law, an additional magnetic field that opposes the external magnetic field is created [111]. The resultant magnetization is relatively weak and is independent of temperature. Diamagnetism is the default form of magnetism in all materials in the absence of other stronger mechanisms.

Paramagnetism is caused by the polarization of unpaired electrons [111]. Electrons possess intrinsic magnetic moments which tend to align parallel to the applied magnetic field. According to Pauli's exclusion principle, electrons tend to pair up as spin-up and spin-down pairs that have a zero net magnetic moment. The presence of unpaired electrons produces a non-zero magnetic moment. Unpaired electrons can be found in transition metal elements such as manganese and iron as well as rare earth elements such as gadolinium. Salts/ solutions containing these ions are therefore strongly paramagnetic. The alignment of the magnetic moment in the same direction as the applied field reinforces the applied magnetic field. Unlike diamagnetism, paramagnetism is temperature dependent due to greater random motion at higher temperature.

In the presence of differences in magnetic susceptibilities, there is a perturbation in the magnetic field. For example, putting a subject into the middle of the bore of the MRI machine distorts the originally homogeneous magnetic field due to the difference in magnetic susceptibility between the object and the surrounding air. Inhomogeneities in the magnetic field at the macroscopic scale are often undesirable as they can cause signal dropouts, for example in brain areas near the sinus where there is a significant susceptibility differ-

ence between the brain and the air pockets. This is the source of artefacts and distortions in echo planar imaging (EPI) [68] as well as blurring in spiral imaging [176].

At the microscopic scale, susceptibility differences between cellular structures can create magnetic field inhomogeneities that can be used to provide valuable information about the underlying tissue microenvironment. In microscopically heterogeneous tissues, the constituent cellular structures can have different magnetic susceptibilities due to their unique chemical compositions and molecular arrangements. The presence of magnetic susceptibility differences between the cellular structures results in local magnetic field inhomogeneities and hence a distribution of magnetic field. The resultant magnetic field distribution pattern depends on the geometry and chemical composition of each of the cellular structures as well as their spatial arrangement with respect to each other. This distribution of magnetic field creates a resonance frequency distribution for underlying spins which affects the measured MRI signal e.g. GRE phase and T_2*.

3.6 Magnetic field calculation

Magnetic susceptibility effects in heterogenous tissues have been widely studied. Various numerical and theoretical models about signal behaviors due to susceptibility effects in heterogeneous tissues have been proposed to explain experimental data from GRE phase images and R_2* maps.

Iterative numerical methods of solving the differential equations of magnetostatics [69] have been used to study susceptibility effects in heterogeneous tissue [22,47,101]. These methods can be used to explicitly generate the actual

magnetic field distribution due to a given geometry of magnetic susceptibility. However, such approaches are limited by the prohibitive computational overhead of numerical methods for calculating field distribution and it was noted by Yablonskiy *et al.* [172] that such methods are often not generalizable and cannot be applied to similar problems.

Yablonskiy *et al.* [172] introduced a generalized theoretical description of NMR signal decay in which they simplified the tissue microstructure by considering single compartment microscopic structures embedded in a homogeneous medium. The microscopic structures are approximated using perfect ellipsoids and/or spheres with additional assumptions made about their volume fractions and spatial arrangements. For example, ferrite contrast agents were modeled as randomly distributed spheres, blood vessel networks as parallel infinite cylinders and bone marrow as randomly oriented cylinders embedded in a homogeneous medium. Such generalized approximations enable the same theoretical description to be used for multiple systems.

Two methods were used in this project for magnetic field calculations. The first is an analytical method that can give precise solution of the magnetic field perturbation from regular ellipsoids. The second is a 3D Fourier method that can be used to approximate the field perturbation caused by any arbitrary susceptibility distribution [102, 129].

3.6.1 Analytical method

The magnetic field perturbation of a solid infinite cylinder is widely used in geometric simulations and can be obtained by considering the boundary conditions in magnetostatics [54]. The resultant frequency perturbation is given

by Eqn. 22.

$$\Delta f_{SC}(r) = \begin{cases} \frac{1}{2} B_0 \gamma \Delta\chi \left[cos^2\theta - \frac{1}{3} \right] & \text{if } r < R; \\ \frac{1}{2} B_0 \gamma \Delta\chi sin^2\theta cos2\phi \left(\frac{R}{r} \right)^2 & \text{if } r > R. \end{cases} \tag{22}$$

where γ is the gyromagnetic constant, $\Delta\chi$ is the magnetic susceptibility difference between inside of the cylinder and outside (e.g. $\Delta\chi = \chi_i - \chi_e$), θ is the angle between B_0 and the long axis of the cylinder, r is the distance between the position vector $\mathbf{r}$ and the origin and ϕ is the angle between the position vector $\mathbf{r}$ and the x-axis (see Fig. 10).

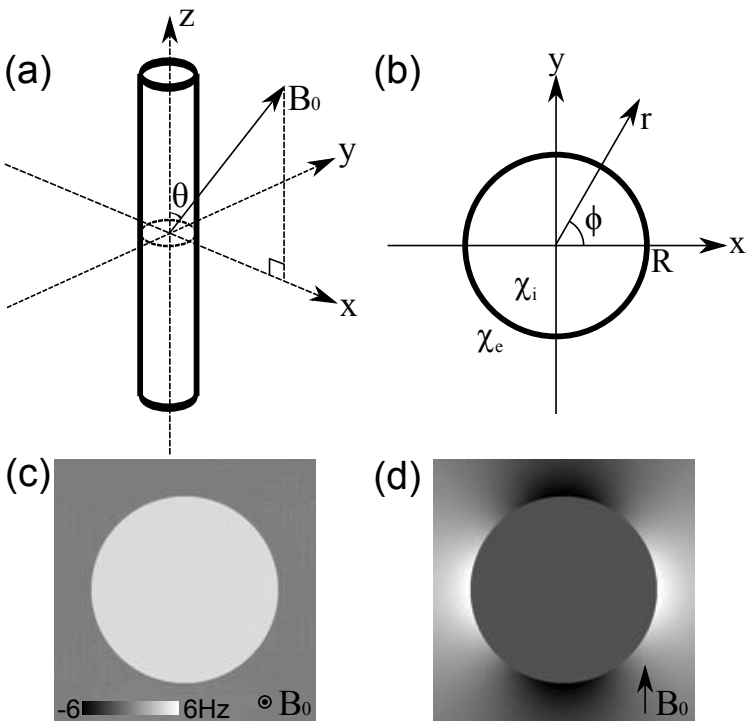

Figure 10: *Analytical solution for frequency perturbation caused by an infinite cylinder. (a) and (b) show the coordinate system used for the analytical solution. (c) and (d) show examples of frequency maps caused by infinite cylinders with long axis at* 0° *and* 90° *to* B_0 *respectively.*

Frequency perturbation by a nested infinite cylinder The frequency perturbation caused by a nested infinite cylinder can be derived from the analytical solution for solid infinite cylinders (e.g. Eqn. 22).Consider the frequency perturbation caused by a nested cylinder with magnetic susceptibility difference $\Delta\chi$ between the nested cylinder and the surrounding medium and an outer radius R_{out} and inner radius R_{in}. Using the principle of superposition, the frequency perturbation caused by a nested cylinder ($\Delta f_{NC}(r)$) can be obtained by subtracting the frequency perturbation of a solid cylinder of radius R_{in} from the field perturbation of a solid cylinder of radius R_{out} (Eq:23).

$$\Delta f_{NC}(r) = \Delta f_{large.SC}(r) - \Delta f_{small.SC}(r) \tag{23}$$

We can derive the analytical expression for the field generated in each of the 3 compartments of the nested cylinder with external radius R_{out} and inner radius R_{in}. For the inner compartment where $r < R_{in}$, there is a total cancellation of the field leading to zero frequency perturbation:

$$\Delta f_{NC}(r) = \frac{1}{2}B_0\gamma\Delta\chi\left[cos^2\theta - \frac{1}{3}\right] - \frac{1}{2}B_0\gamma(\Delta\chi)\left[cos^2\theta - \frac{1}{3}\right] = 0 \tag{24}$$

For the middle compartment where $R_{in} < r < R_{out}$, the net frequency is the subtraction of the frequency outside the smaller cylinder from the frequency inside the large cylinder.

$$\begin{aligned}\Delta f_{NC}(r) &= \frac{1}{2}B_0\gamma\Delta\chi\left[cos^2\theta - \frac{1}{3}\right] - \frac{1}{2}B_0\gamma(\Delta\chi)sin^2\theta cos2\phi\left(\frac{R_{in}}{r}\right)^2 \\ &= \frac{1}{2}B_0\gamma\Delta\chi\left[cos^2\theta - \frac{1}{3} - sin^2\theta cos2\phi\left(\frac{R_{in}}{r}\right)^2\right]\end{aligned} \tag{25}$$

For the outer compartment where $r > R_{out}$, the net frequency is the subtraction of the frequency outside of the smaller cylinder from the frequency outside of the large cylinder and the frequency.

$$\begin{aligned}\Delta f_{NC}(r) &= \frac{1}{2}B_0\gamma\Delta\chi sin^2\theta cos2\phi\left(\frac{R_{out}}{r}\right)^2 - \frac{1}{2}B_0\gamma(\Delta\chi)sin^2\theta cos2\phi\left(\frac{R_{in}}{r}\right)^2 \\ &= \frac{1}{2}B_0\gamma\Delta\chi sin^2\theta cos2\phi\left[\frac{R_{out}^2 - R_{in}^2}{r^2}\right] \end{aligned} \tag{26}$$

To summarize, the frequency perturbation caused by an nested cylinder can be expressed as follows:

$$\Delta f_{NC}(r) = \begin{cases} 0 & \text{if } r < Rin; \\ \frac{1}{2}B_0\gamma\Delta\chi\left[cos^2\theta - \frac{1}{3} - sin^2\theta cos2\phi\left(\frac{R_{in}}{r}\right)^2\right] & \text{if } Rin < r < Rout; \\ \frac{1}{2}B_0\gamma\Delta\chi sin^2\theta cos2\phi\left[\frac{R_{out}^2 - R_{in}^2}{r^2}\right] & \text{if } r > Rout. \end{cases} \tag{27}$$

Lorentz sphere An important concept called the Lorentz sphere for calculating the field offset within an object is discussed here. When an object is placed in a medium with different magnetic susceptibility in the presence of an external magnetic field, a shift in Larmor frequency is created. The frequency shift is affected by the macroscopic effect due to the bulk shape of the object and a nanoscopic effect due to the interaction between the nanoscale magnetic susceptibility inclusions that make up the object. This nanoscopic contribution in often described in terms of a Lorentz sphere effect [34, 40, 95]. The Lorentz sphere is an imaginary boundary used to account for the internal magnetic field experienced by a nucleus in a homogeneous medium in the presence of an external homogeneous magnetic field (Fig. 11a).

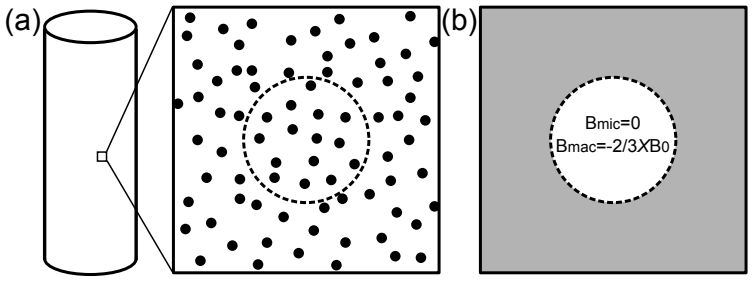

Figure 11: *(a) Bulk shape of a cylinder with a zoomed in cartoon of the molecular 'granularity' of the supposed continuous medium. Dashed lines represent an arbitrary Lorentz boundary (b) Effective contribution from macroscopic and microscopic field sources.*

Consider a system in which susceptibility inclusions are modeled as magnetic dipoles and are distributed randomly throughout an object. To find the magnetic field experienced by a single nucleus within the object, an imaginary sphere surrounding the nucleus is constructed. The sphere is assumed to be microscopically large such that the nucleus sees the outside of the sphere as a uniform macroscopic continuum but macroscopically small as compared to the bulk shape of the object. Within the sphere, the combined field experienced by the nucleus from the dipoles is practically zero due to the symmetric distribution of dipoles. Since the nucleus sees the outside of the sphere as a uniform macroscopic continuum, the field due to the Lorentz sphere in a homogeneous object can be approximated as the inside of a continuous sphere. The effective field seen by the nucleus is the summation of the field from within the Lorentz sphere (which is zero) and the field from outside the Lorentz sphere(Fig. 11b). Since the sphere is macroscopically small, the same conclusion can be extended to all nuclei within the object. This correction for the effective field seen by the nucleus is added to the nanoscopic field contribution due to the bulk shape of the object when calculating the actual magnetic field perturbation due to a homogeneous object of a particular bulk shape in an external magnetic field.

3.6.2 Fourier method

The 3D Fourier method [102,129] is a fast and efficient method used for approximating the magnetic field perturbation caused by an arbitrary distribution of magnetic susceptibility. The basic idea is to convert the convolution of the underlying susceptibility distribution with a unit dipolar field into an element-wise multiplication in the Fourier domain [102]. This method compares well with other more accurate but slower iterative methods [75] as well as theoretical values for well-defined ellipsoids, with observable errors only near susceptibility boundaries, where the finite extent of calculation in the Fourier domain limits the ability to represent abrupt spatial changes. This method has been used for post-acquisition image correction and magnetic field shimming [75, 102]. The 3D Fourier method has also been used to model tissue microstructures of much smaller scale such as in a realistic model of the cortical vasculature of a rat brain [103]. More recently, this method has been inverted to obtain susceptibility maps from GRE phase maps [31, 136, 139, 163]. This method was used in this thesis for simulating the magnetic field perturbation of some non-ellipsoidal 3D structures (e.g. Fig. 34).

4 Geometric model of white matter

GRE signal phase and magnitude are sensitive to mesoscopic magnetic field inhomogeneities caused by the underlying tissue microstructure. Recent studies have attributed GRE phase and magnitude contrast observed between WM and GM and within WM itself [89] to microstructural differences. However, most studies do not relate the explicit WM microstructure , which is inherently a geometric property of tissue microstructure, with the observed GRE contrast.

The aim of this study is to create an explicit geometric model of WM that can be used to simulate the effects of the actual WM microstructure on GRE contrast. We begin with a look at existing models that describe the effects of tissue microstructure on GRE signal. Next, we introduce the concept of using geometric modeling to obtain the actual magnetic field perturbation from a spatial distribution of magnetic inclusions. We then test the validity of geometric modeling by simulating the frequency perturbation caused by a random packing of parallel cylinders and comparing the resultant orientation dependent GRE signal with a polypropylene fiber phantom. Thereafter, we introduce our geometric model of WM and show the simulated GRE signal characteristics from a sample scenario before discussing some considerations in the model.

4.1 Effects of tissue microstructure on GRE signal

4.1.1 R_2* changes

Geometric models have been used in the brain to quantify changes in R_2*. Ogawa *et al.* [118] used a single representative cylinder to model BOLD related changes. Fisel *et al.* [45] and Boxerman *et al.* [18] used multiple cylinder models to study the effects of paramagnetic contrast agents in vasculature.

The use of geometric models to quantify changes in the WM is less common. The observed orientation dependence of R_2* in WM has been closely linked to the long structure of the axons. Bender *et al.* [11] has linked this dependence to the theoretical approach for parallel cylinders proposed by Yablonskiy *et al.* [172]. According to Yablonskiy *et al.*, R_2* change (assuming that R_2 does not change, such that $\Delta R_2* = \Delta R_2$') of parallel randomly distributed cylinders depends on a number of factors and can be expressed as Eqn. 28

$$\Delta R_2* = 2\pi \cdot \frac{1}{2} \cdot \gamma \cdot \Delta\chi \cdot B_0 \cdot sin^2\theta \cdot \zeta \tag{28}$$

Where γ is the gyromagnetic ratio, $\Delta\chi$ is the susceptibility difference between the magnetic field perturbators and the medium, ζ is the volume fraction of the magnetic field perturbators and θ is the orientation of the long axis of the cylinder to B_0. Δ R_2* is expected to show linear variations with changes to magnetic susceptibility and volume fraction of the perturbators and a sin^2 variation with orientation to B_0. Underlying assumptions include low volume fraction of the susceptibility inclusions such that signal change is only considered in the medium (not the perturbers) and that the static dephasing regime is valid. The extension of a similar approach to study MR signal behavior in

WM is non-trivial due to the presence of signal from multiple compartments and the significant volume fraction of each of these compartments. The summation of signal contributions from the different compartments can cause the deviation of the signal behavior from that predicted by a single compartment model.

4.1.2 Resonance frequency changes

Phase changes in WM are often regarded as bulk changes to a homogeneous distribution of magnetic field perturbators [38] and analytical solutions based on Lorentz sphere correction are then used to calculate possible frequency shifts.

Anisotropic cellular structure can cause orientation dependence of signal [60]. Especially in WM which is actually composed of a large number of longitudinal structures such as myelin sheaths and filaments that mostly run along the long axis of the WM fibers. These longitudinal structures have different magnetic susceptibilities compared to the surrounding environment (e.g. lipid rich myelin sheaths are expected to be diamagnetic [38]) and are expected to generate orientation dependent magnetic field perturbations. He *et al.* [60] has previously reported that the Lorentz sphere correction is unable to account for the lack of large resonance frequency difference between the WM and cerebrospinal fluid (CSF) in the motor cortex despite the substantial difference in their magnetic susceptibility. He *et al.* argued that the Lorentz sphere correction is incompatible with a system in which the microscopic susceptibility inclusions are longitudinal structures that cannot be accurately approximated using point dipolar sources. He *et al.* therefore proposed a generalized Lorentzian cavity theory which takes into account the presence of longitudinal

structures by introducing a Lorentz cylinder instead of a Lorentz sphere in order to properly enclose the susceptibility inclusions. According to He *et al.*, the microscopic frequency shift due to longitudinal structures (excluding any bulk shape effects) can be expressed as below

$$\Delta f = \frac{1}{2} \cdot \gamma \cdot \Delta\chi \cdot B_0 \cdot sin^2\theta \cdot \zeta \tag{29}$$

Where γ is the gyromagnetic ratio, $\Delta\chi$ is the susceptibility difference between the magnetic field perturbators, ζ is the volume fraction of the magnetic field perturbators and θ is the orientation of the long axis of the cylinder to B_0. Similar to Δ R_2*, resonance frequency is predicted to change linearly with magnetic susceptibility and volume fraction of the perturbators and with a sin^2 trend with orientation to B_0. The longitudinal structures themselves are assumed not to give off MR signal themselves. In accounting for the lack of difference in resonance frequency of CSF and WM, this Lorentz cylinder theorem predicted an orientation dependence of WM resonance frequency.

Another mechanism that can lead to changes in resonance frequency is changes in magnetic susceptibility [82, 91] itself when orientation to B_0 changes. The mechanism is termed susceptibility anisotropy and is attributed to the presence of highly ordered structures at the molecular level that can cause an orientation dependent disturbance in electron orbit [37]. Such anisotropy has been observed in various biological structures spanning a range of length scale, including helical proteins, bilipid layers and muscle fibers [37]. Susceptibility anisotropy in WM was first demonstrated by Lee *et al.* [82] using postmortem WM sections in which he showed non-local GRE phase changes when orienta-

tion changes despite controlling for bulk shape effects. Lee *et al.* then used simulations incorporating susceptibility anisotropy to explain the observed non-local effect, which was not predicted by the Lorentz cylinder theory.

Despite increasing evidence that WM microstructure affects GRE signal, there is a lack of a model that shows a direct link between the experimental observations to actual changes in WM microstructure. The aim of this project is to develop a multi-compartmental geometric model of WM microstructure in which we explicitly model the myelin sheaths and axons to simulate the changes in frequency perturbation. It is noted here that since the start of this project, other groups have also introduced similar geometric models of WM microstructure [131,164], and comparisons with these models are not discussed in this thesis but would be a subject of future investigation. We then generate the field distribution to simulate the full spectrum of signal behaviours in GRE(i.e. time evolution of both signal magnitude and phase from which lower moments such as R_2* and resonance frequency as well as higher moments such as deviation from mono-exponential decay and deviation from linear phase evolution can be studied). This is important because most signal theories are only designed to answer a single aspect of the signal characteristics with respect to changes in the local magnetic field due to microstructure changes. However, it can be seen that these changes share a common origin and it would be beneficial to use a single model that can be used to study a wide range of signal behaviours.

4.2 Geometric modeling

The frequency perturbation caused by a single infinite cylinder at a specific orientation to B_0 can be calculated using Eqn. 22. For an ensemble of infinite cylinders, the effective frequency perturbation is the summation of the frequency perturbation created by each individual cylinder. For a circular bundle of randomly arranged cylinders, the resultant frequency perturbation when the long cylinder axis is parallel and perpendicular are shown in Fig. 12e and f respectively.

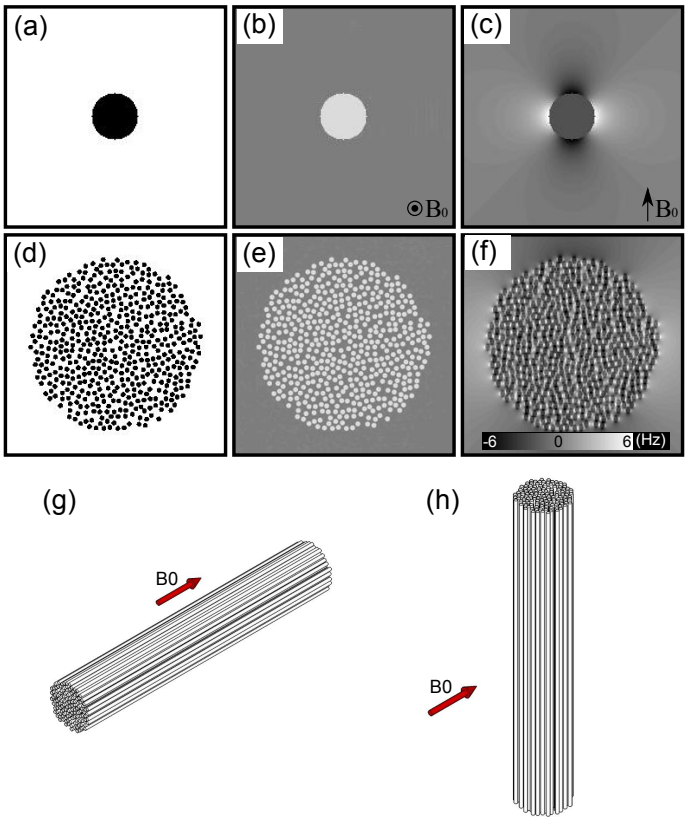

Figure 12: *Geometric modeling of a bundle of cylinders. (a) Susceptibility map of a single infinite cylinder. The frequency perturbation maps caused by the single cylinder when the magnetic field is parallel and perpendicular to the long axis of the fiber are given in (b) and (c) respectively with* $\Delta\chi$*=0.1ppm. (d) Circular bundle of infinite cylinders. The frequency perturbation maps at* 0° *and* 90° *are given by (e) and (f). (g) and (h) shows the bulk shape of the fiber bundle when the magnetic field is parallel and perpendicular respectively.*

4.2.1 Macroscopic vs microscopic field

The effective magnetic field can be decomposed into a macroscopic component (bulk field due to overall phantom shape) and microscopic component (introduced by each fiber). The macroscopic field in the circular bundle of cylinders is due to the cylindrical shape of the bundle with the long axis of the bulk shape being in the same direction as the constituent cylinders (Fig. 12g-h). It is useful to separate the microscopic field contribution (due to the susceptibility inclusions) from the macroscopic field contribution (due to bulk shape). The microscopic field contribution would be equivalent to the magnetic field caused by an infinite extent of susceptibility inclusions. Going back to the circular bundle of fibers, we can imagine the outside of the circular bundle to be filled with fibers (Fig. 13b). The presence of an infinite extent of fibers outside the fiber bundle creates a magnetic field within the fiber bundle. This additional magnetic field can be calculated by treating the fibers outside of the fiber bundle as a homogeneous medium with magnetic susceptibility equal to the mean volume susceptibility of the modeled fibers (Fig. 13c).

In order to find the microscopic field contribution from the fiber bundle, we first find the magnetic field caused by the fiber bundle embedded in a medium of null susceptibility. We then find the magnetic field due to an infinite extent of fibers outside the circular bundle, which can be calculated as the constant magnetic field within an infinite cylinder with susceptibility equivalent to negative of the mean volume magnetic susceptibility of the circular bundle. Adding these two magnetic fields would give the microscopic magnetic field (Fig. 13d-i). It can be seen that the effective magnetic field and the microscopic magnetic field are linked by a constant field shift which will not affect the simulated GRE signal decay rate but will have implications in predicting frequency shifts.

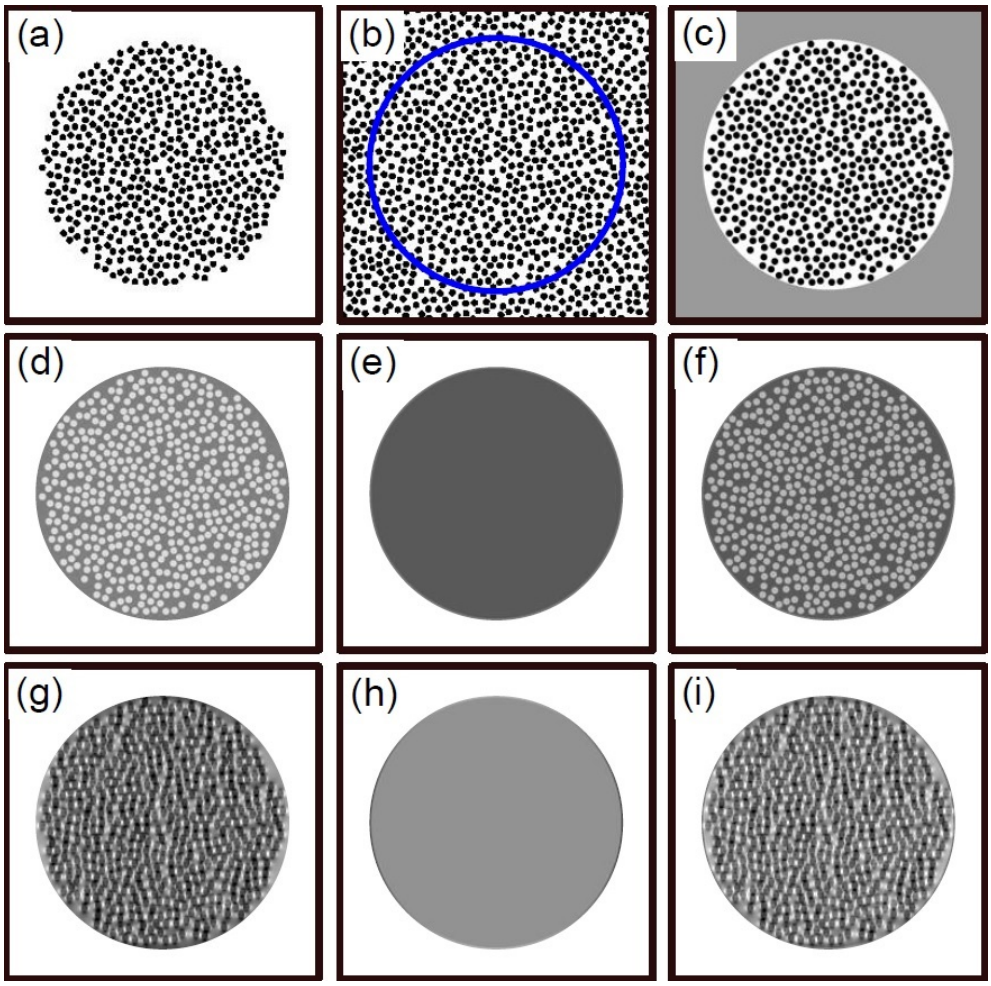

Figure 13: *Microscopic magnetic field perturbation. For a circular bundle of fibers (a), the magnetic field perturbation generated is associated with the bulk shape. In contrast, the microscopic magnetic field perturbation is equivalent to the magnetic field perturbation that would be experienced if the fiber bundle is just a subsample of an infinite extent of parallel fibers shown in (b). The outside fibers can be approximated as that by a bulk continuum with equivalent mean volume susceptibility (c). (d) represents the frequency map within a circular bundle when the fibers are parallel to* B_0*. (e) represents the frequency map contribution from the outside fibers. (f) shows the frequency map obtained by the sum of (d) and (e). (g) to (i) correspond to the case for fibers perpendicular to* B_0*. Note that for (d) to (i) only the intra-bundle fields which are of interest are illustrated.*

4.2.2 Effective frequency distribution

The effective magnetic field perturbation at a given location is the sum of the macroscopic magnetic field perturbation caused bulk shape of the subject and the microscopic magnetic field perturbation resulted from the underlying microstructure. Given the bulk shape and the microscopic magnetic field perturbation due to the underlying microstructure, the frequency distribution (e.g. frequency histogram) due to both effects can be obtained by the convolution of the frequency distribution due to the bulk shape with the frequency distribution due to the microstructure.

4.2.3 Single cylinder approximation

At low volume fractions and susceptibility, it is sufficiently accurate to use a single cylinder [117] to model frequency changes that will be caused by a collection of smaller cylinders with the same volume fraction. However, this approximation gets more inaccurate as the volume fraction or susceptibility increases [45] . This is especially so if we were to consider the signal from inside the cylinder.

Effects of FOV shape on single cylinder simulation To simulate the frequency perturbation of a single cylinder with large volume fraction, the shape of the region of interest (ROI) can affect the field pattern sampled, leading to potentially important differences in the simulated GRE signal. The selection of field of view (FOV) can bias the sampling of the frequency perturbation (Fig. 14). Let us consider the frequency perturbation caused by a single cylinder ($\Delta\chi = 0.1ppm$) with volume fraction 0.4. We consider 3 dif-

ferent FOVs representing a concentric circle FOV, square FOV centred at the middle of the cylinder and an off-centred square FOV (Fig.14).

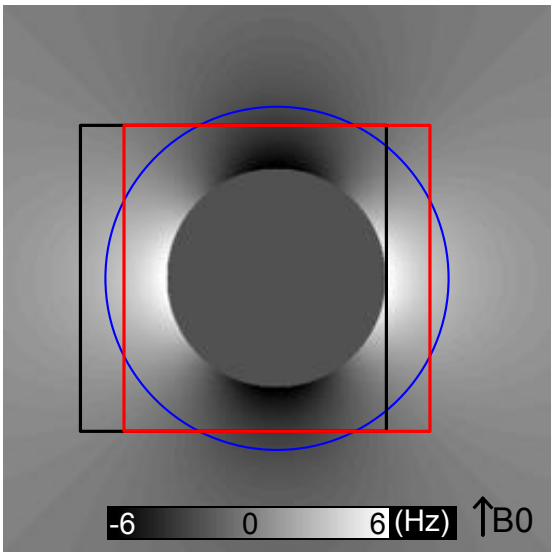

Figure 14: *FOV shapes and location. Diagram shows the frequency map generated by a single cylinder perpendicular to the magnetic field. 3 different FOV shapes were drawn corresponding to circular FOV (blue), centred square FOV (red) and shifted square FOV (black)*

Considering only the outside of the cylinder compartment, the frequency histogram for the circle FOV is distinctly different from that of the centred square FOV (Fig. 15a). 2 distinct peaks are seen for the circle FOV while 3 are seen for the centred square. The resultant GRE signal magnitude decay (Fig. 15b) is significantly faster for the circle FOV compared to the square FOV. Both the circle and centred square FOVs displayed a linear phase evolution at 0Hz (Fig. 15c). On the other hand, the evolution of signal phase with time for the shifted square FOV shows a peculiar non-linear trend. This non-linear phase evolution can be explained by the asymmetric frequency distribution caused by biased sampling of frequencies in the shifted square FOV. Unlike the circle and centred square FOVs in which the symmetric frequency distribution ensures complete cancellation of the positive and negative frequency shifts, the shifted

square FOV does not have a median frequency about which positive and negative frequencies can completely cancel out each other. The shifted square FOV can also be seen to cause less signal decay than the centred square FOV.

If we include contribution of signal from the intra-cylinder compartment, the frequency distribution is skewed to the negative frequency(Fig. 15d). Interestingly, the GRE signal magnitude decay (Fig. 14e) seems to be slower with the signal interference from the intra-cylinder compartment, although the circle FOV still decays faster than the square FOV. The asymmetric frequency distributions in all three FOVs show significant negative non-linear phase evolution (Fig. 14f).

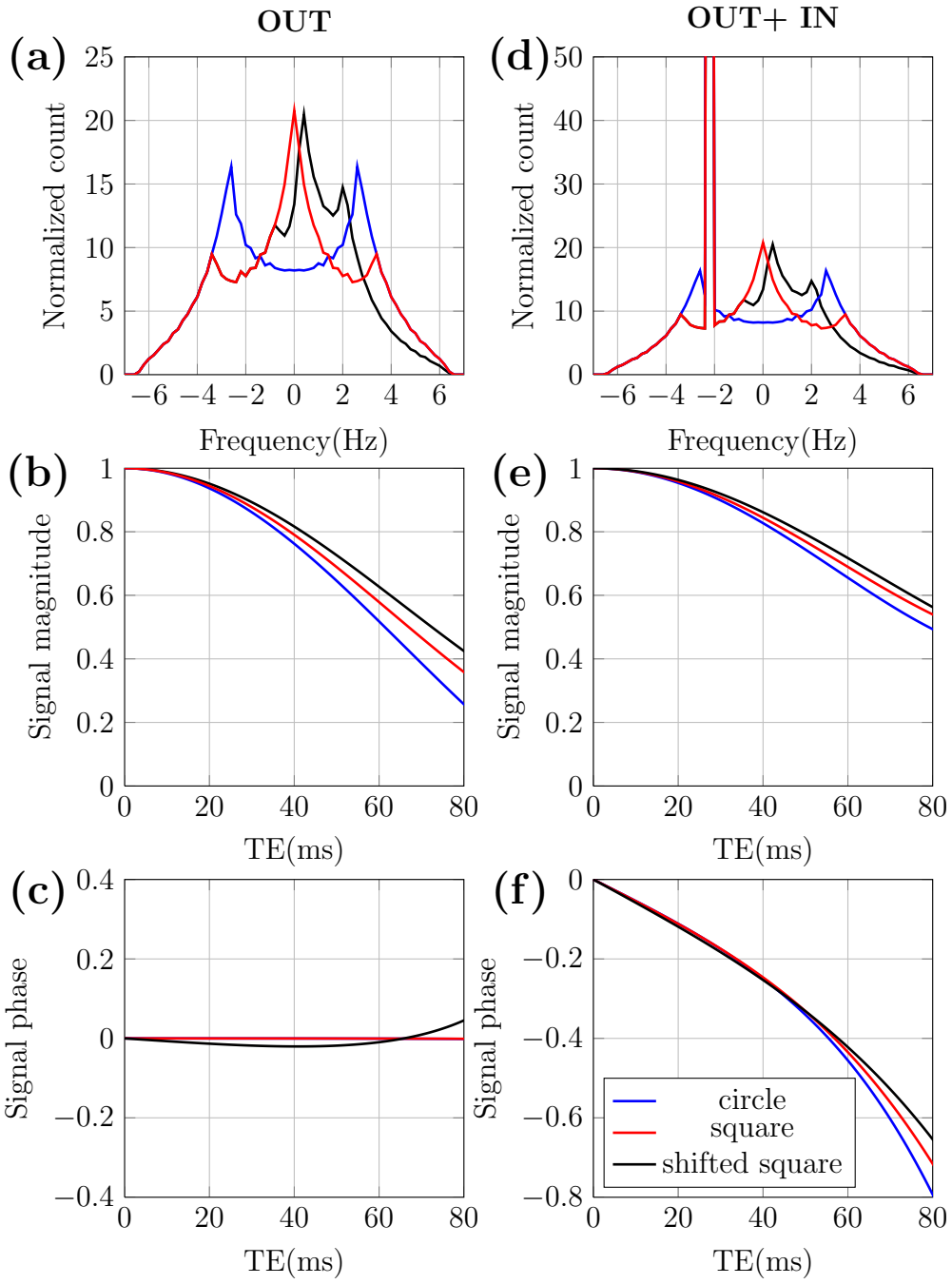

Figure 15: *Effects of FOV. The first column shows the effect of FOV on the frequency map sampled from outside of the cylinder. Blue, red and black represents the circle, square and shifted square FOVs respectively. (a) shows the frequency histogram. (b) shows the signal magnitude decay. (c) shows the phase evolution. The second column (d-e) shows the effect of FOV on the frequency map sampled from the whole FOV (i.e. outside and inside of the cylinder)*

Single vs multiple cylinders Next, we investigate the approximation of field generated by an ensemble of multiple cylinders using a single cylinder of equivalent volume fraction. We first consider a single cylinder model (Fig. 16a) with a large volume fraction and a multiple smaller cylinders model (Fig. 16b) with the same volume fraction (0.4). Some details of the model include $\chi = 0.1ppm$ and B_0 at 90° to the long axis of the cylinder. The bulk shape of the multiple small fiber packing is circular and a central square region is considered here.

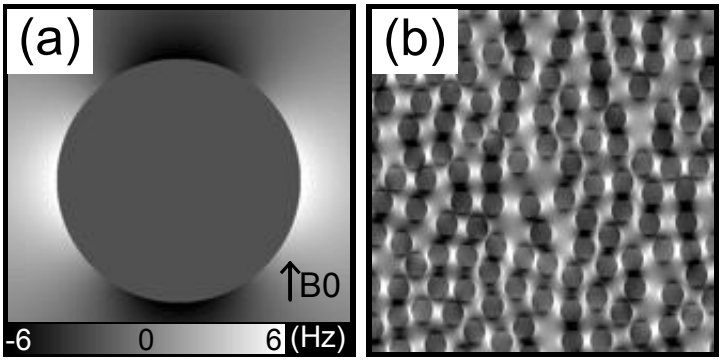

Figure 16: *Single vs multiple cylinders. Frequency maps generated by (a) single cylinder and (b) multiple cylinders with the same volume fraction and magnetic field perpendicular to long cylinder axis.*

The frequency distribution for the single cylinder with a centred square FOV is distinctly different from that of random packing of smaller cylinders. In general, a more smoothed out frequency distribution is obtained for the random packing of multiple smaller cylinders in which the multiple peaks seen in single cylinder are no longer visible (Fig. 17a,d). This is due to the superposition of frequency perturbations generated by the individual cylinders. The signal magnitude decays of the single and multiple cylinders display minute differences when only the extra-cylinder compartment is considered (Fig. 17b). Specifically, the decay for the multiple cylinders is faster than the single cylinder before 70ms. The difference becomes more obvious when considering all

compartments (Fig. 17e). Here, the multiple cylinders display a faster signal decay throughout the whole range of TE simulated. The difference between a single cylinder and multiple smaller cylinders is expected to be more significant as the volume fraction of the perturbators increase. For phase evolution, both single cylinder and multiple random cylinders create a linear zero phase evolution when considering only the extra-cylinder compartment which is expected due to the symmetric distribution (Fig. 17c). The contribution from inside the cylinder will cause both phase evolutions to be negative and non-linear (Fig. 17f). Minimal difference is seen between the phase trends from the single and multiple cylinders.

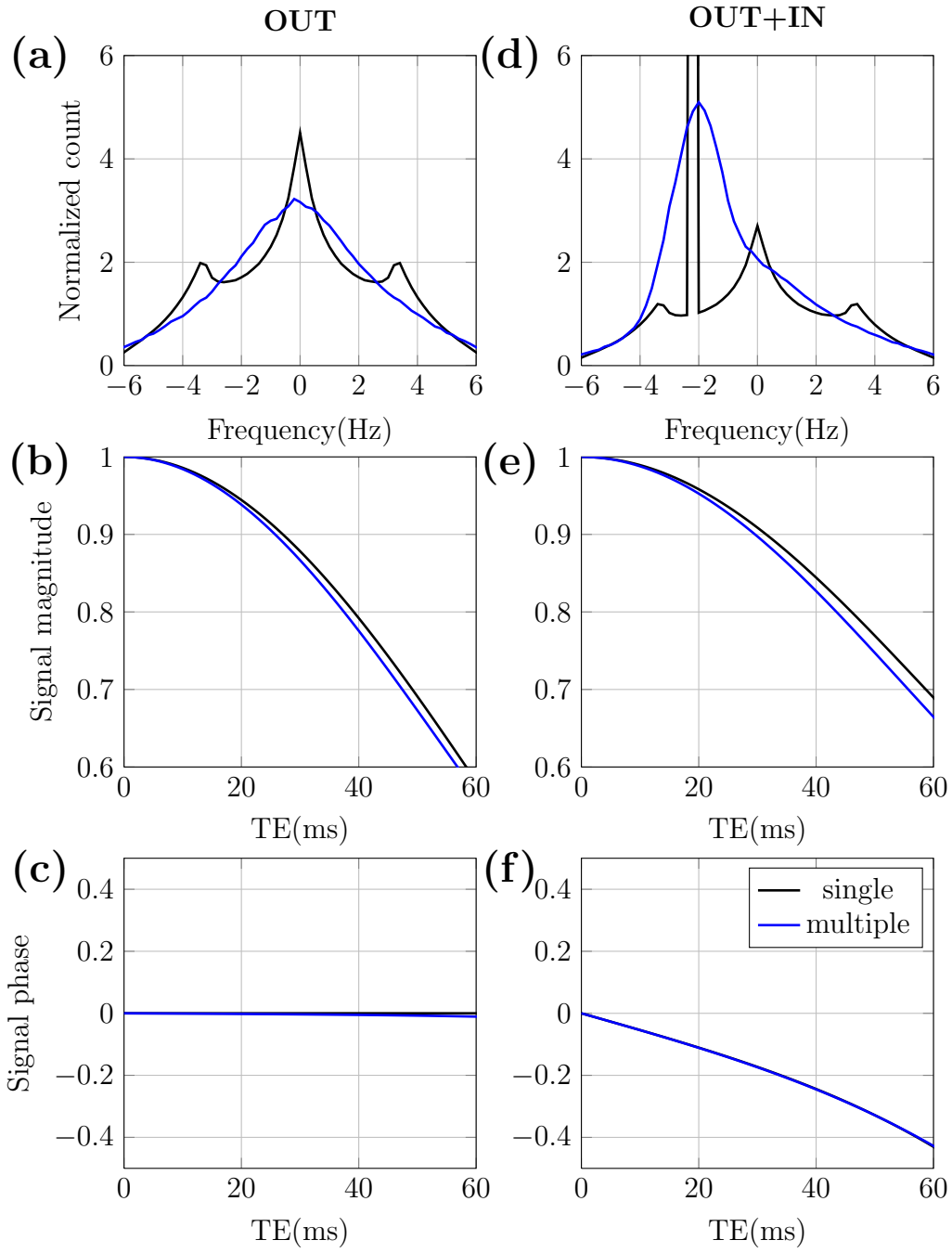

Figure 17: *Results of single vs multiple cylinders simulations. The first column shows the effect of packing on the frequency map sampled from outside of the cylinder. (a) shows the frequency histogram. (b) shows the signal decay. (c) shows the phase evolution. The second column show the frequency map sampled from the whole FOV (i.e. outside and inside of the cylinder) (d) shows the frequency histogram. (e) shows the signal decay. (f) shows the phase evolution.*

4.2.4 Effects of different packings

In a multiple cylinder model, the spatial packing of the cylinders can affect the frequency distribution, which will in turn affect the simulated GRE signal characteristics. To illustrate this, we compared the frequency perturbations caused by random, hexagonal, square and rectangle packings (Figs. 18a-e). For rectangle packings, we considered 2 cases in which one packing is rotated 90° with respect to the other. Like before, we separate the observations made if we consider only the external compartment and if we consider both the internal and external compartments.

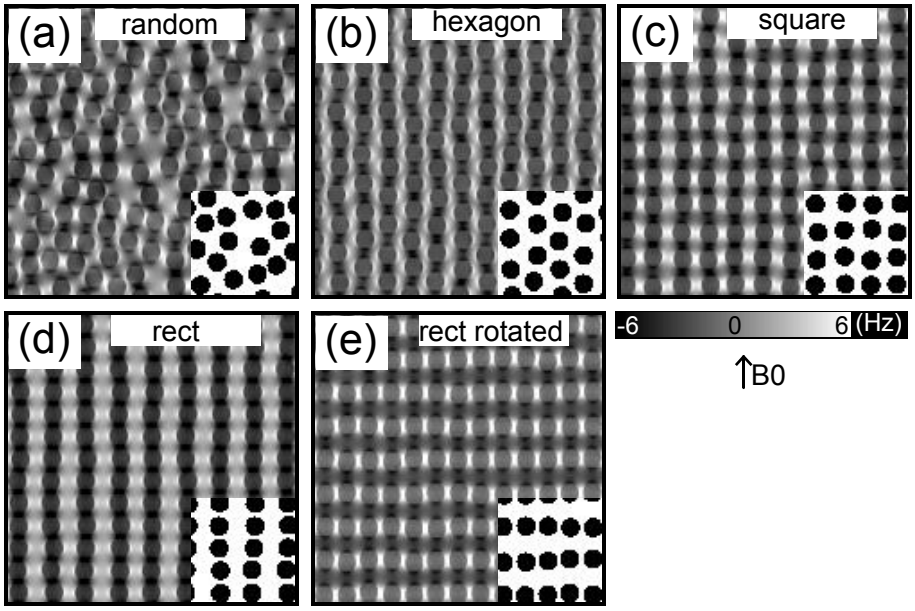

Figure 18: *Effect of packing was illustrated with the frequency maps corresponding to the following packings (a) Random (b) Hexagon (c) Square (d) Rectangle (e) Rectangle rotated. Slight perturbations were added to all the packings. Small box at the bottom right of each sub-figure shows a representation of the spatial arrangement of the cylinders.All scenarios have the same volume fraction (0.4) and volume susceptibility* ($\chi = 0.1ppm$)

Considering only the outer compartment, we can see that the hexagonal packing produces an asymmetrical frequency distribution (Fig. 19a). The decay

rate can be seen to be faster than that of the random packing (Fig. 19b). The asymmetry introduced significant non linear phase evolution (Fig. 19c). A square packing leads to a frequency histogram with 2 large peaks near the ends of the frequency range, a result of the biased overlapping of the frequency distribution at the poles of the cylinders. The resultant signal decay is the largest compared to the other packings. Phase evolution is zero and linear due to symmetry of frequency distribution. For the rectangle packings (orange and magenta lines), two highly asymmetric frequency histograms which are mirror reflections of each other about the y axis can be seen. The resultant decay curves are identical while the phase evolution curves are reflections of each other about the x axis. This implies that for the same spatial arrangement of magnetic field perturbators it is possible to obtain frequency changes that varies with orientation to B_0. Both phase evolution curves are non linear as expected from asymmetrical frequency distributions.

If we consider both inner and outer compartments, all the previously symmetrical frequency distributions become highly skewed to one side (Fig. 19d). The decay rates for all the packings appear to decrease except for the rectangle packing with horizontal long axis (orange line) in which the decay rate increases. The addition of the inner compartment causes the frequency distribution of the 2 rectangle packings to no longer be reflections of each other, leading to a different signal decay curve. All the phase evolution curves gain a negative gradient and deviations from linear phase evolution can be seen.

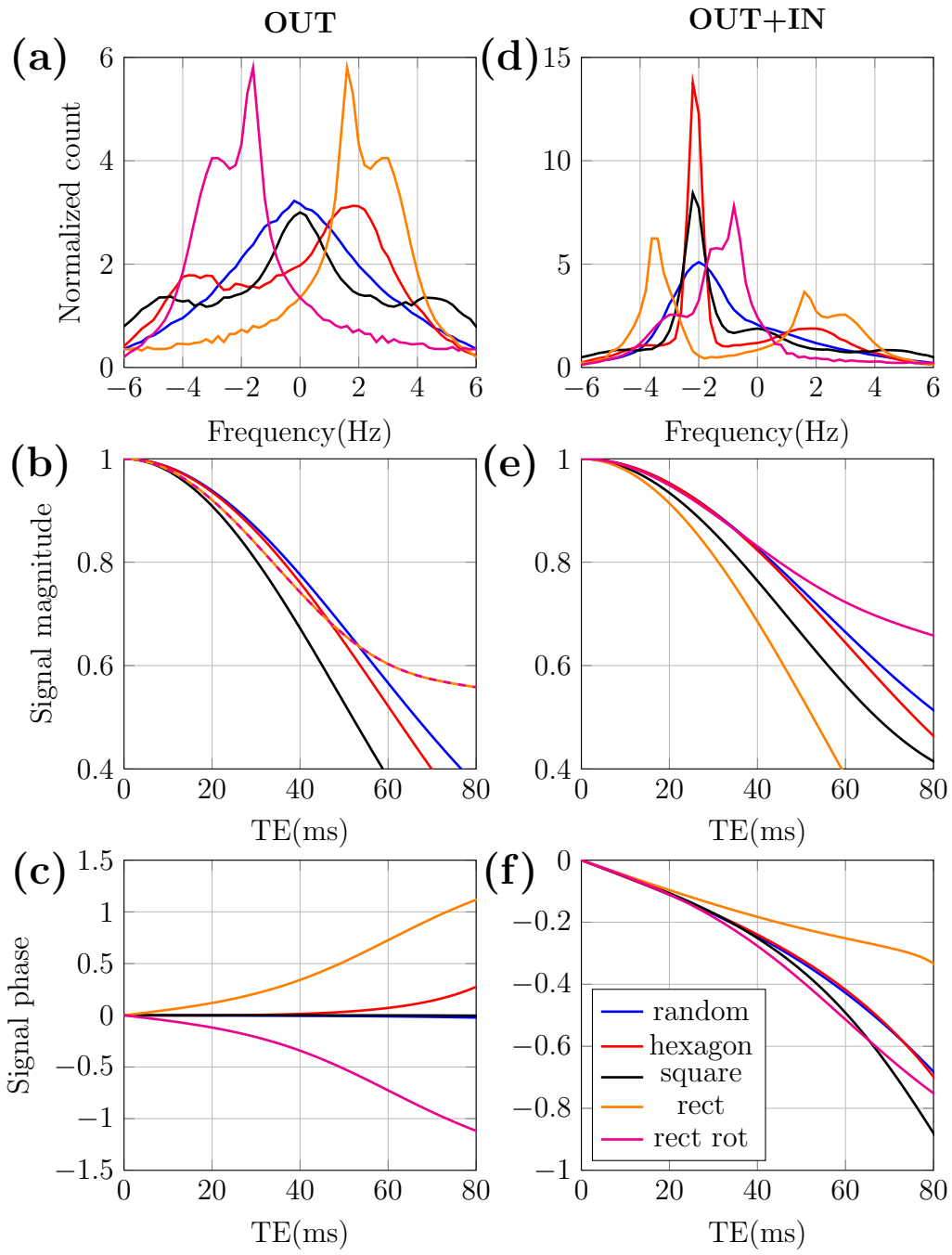

Figure 19: *Results of packing. Each line represents to one of the packings in Fig. 18. The first column shows the effect of packing on the frequency map sampled from outside of the cylinder. (a) Frequency histogram. (b) Signal magnitude decay. (c)Signal phase evolution. The second column show the frequency map sampled from the whole FOV (i.e. outside and inside of the cylinder) (d) Frequency histogram. (e) Signal magnitude decay. (f) Signal phase evolution.*

4.3 Phantom validation

Most GRE signal models have considered susceptibility inclusions which have low volume fraction and simple geometry e.g. modeling the magnetic field perturbation from blood vessels using a single cylinder [118, 172]. A realistic model of WM microstructure will include more complicated geometries and tighter packing due to the higher volume fraction of perturbators (e.g. myelin). As a first step, we validate the geometric modeling of high volume fraction perturbators using a polypropylene fiber phantom. Specifically, we compare the experimental orientation dependence of resonance frequency and R_2* of long polypropylene fibers with simulations results.

4.3.1 Materials and methods

Phantom construction The phantom consists of a central cubic region with straightened polypropylene fishing lines (Vantage Pro lbs brown, 13-353-14, 0.35mm) stacked approximately parallel to each other. An outer ring of fishing lines was arranged orthogonal to these fibers in order to roughly match the magnetic susceptibility of the inner square (Fig. 20). The cylindrical bulk shape of the fibre-packed region minimizes the bulk susceptibility effects between different spatial regions when the phantom is rotated. This fishing line phantom was then immersed into a container filled with copper (II) sulphate doped water.

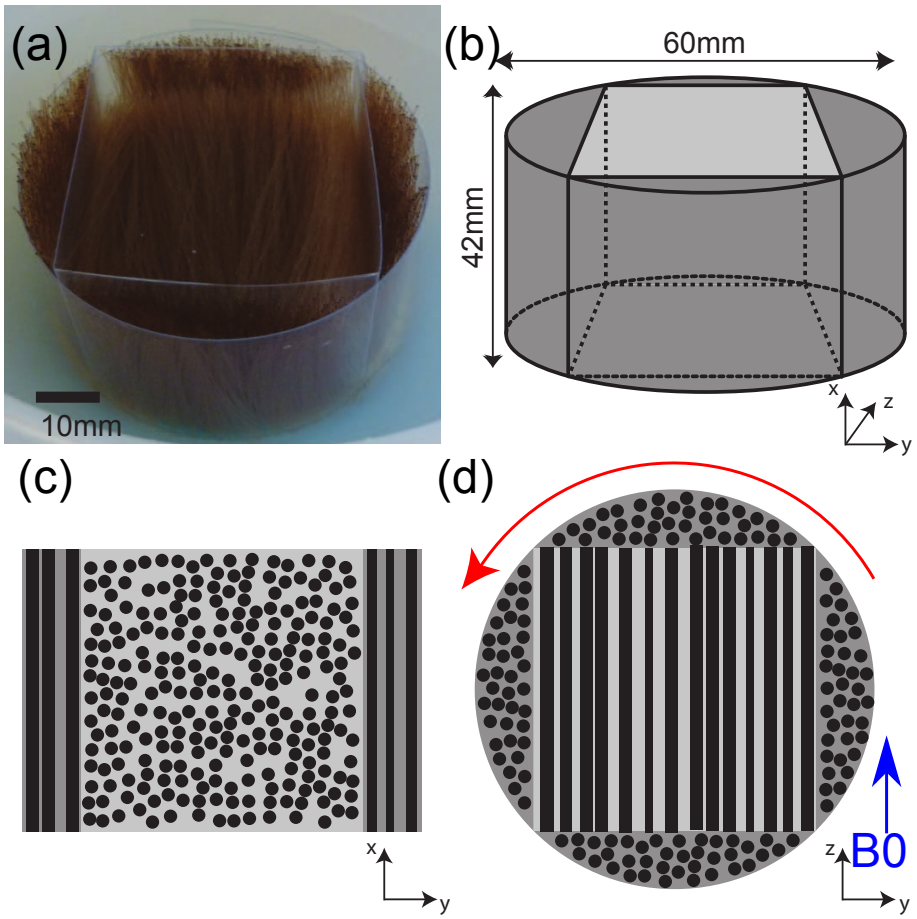

Figure 20: *(a) Polypropylene fishing line phantom. (b) Dimensions of the phantom. Cross sectional views of the phantom along the xy plane and yz planes are shown in (c) and (d) respectively. The blue arrow indicates the direction of B_0 and the red arrow indicates the direction of rotation of the phantom about the mid point.*

Imaging and fitting protocol The phantom was carefully rotated about the x-axis at the middle of the phantom to obtain 10 different orientations of the long fiber axis to B_0 from 0° to 90° in steps of 10°. R_2*, R_2 and resonance frequency measurements were carried out at each of the 10 orientations. A 2D multi-echo GRE sequence was used to measure the R_2* decay. Eight, 2mm-thick interleaved slices were acquired with 6 echoes at TE 20,24,28,32,36 and 40ms (TR = 1500ms, FOV $128 \times 128 mm^2$, matrix 64×64, 2 averages and flip angle 45°). The R_2* value was estimated with linear fitting to the

logarithm of the magnitude images for even echoes. T_2 was measured with a 2D dual-echo spin-echo sequence with 2 echoes at TE 12 and 50ms (TR = 1500ms, FOV $128 \times 128mm^2$, 64×64, 2 averages), and R_2 was fitted using the same procedure. GRE phase was obtained from the GRE echoes at TE 4 and 20ms (TR = 1500ms, FOV $128 \times 128mm^2$, matrix 64×64, 2 averages and flip angle 10°). The complex conjugate of the raw image of the second echo was multiplied with the raw image of the first echo and the resultant phase image was phase unwrapped using FSL [71]. The final resonance frequency map was then obtained by dividing the phase difference by the echo time interval and 2π. Background phase contribution was removed by fitting a 2D 4th order polynomial to the unwrapped phase images and then deducting the fit from the original image. A $10mm \times 10mm$ middle region at slice 5 was selected for ROI analysis. The actual orientation of the fibers were found to deviate slightly from the 10° step and the adjustment to the actual orientation was performed by measuring the angle along a prominent edge of the central cubic region in the magnitude images using ImageJ.

Geometric modeling We model the polypropylene fibers as randomly distributed infinite cylinders . Since the macroscopic field contribution from the phantom does not change with each rotation of the phantom, we consider only changes due to microscopic field contribution at each orientation (i.e. Fig. 13). To create a random distribution of parallel infinite cylinders of various volume fractions, we randomly placed circles in a circular FOV in a sequential, non-overlapping manner until the required volume fraction is obtained. Multiple re-runs of the circle packing process are normally required to obtain higher volume fraction packings.

The volume fraction of the fibers can be estimated from the volume of fiber used in making the phantom (length=952m, diameter=0.35mm) divided by the volume occupied by the fiber phantom in the container (height=42mm, diameter=60mm) to give a volume fraction of 0.19. The magnetic susceptibility difference between the polypropylene fibers and the solution is unknown. This value was estimated by fitting the simulated R_2* and GRE frequency at different orientation to B_0 and getting the best fit (computed using least squares fitting). The best fit magnetic susceptibility obtained was 0.24ppm.

4.3.2 Results and discussion

Resonance frequency changes The measured resonance frequency shows a sinusoidal increase as θ (angle between long fiber axis to B_0) is increased (Fig. 21). The simulated GRE frequencies over the range of θ follows a $sin^2\theta$ trend and matches the experimental results well. This $sin^2\theta$ trend is similar to that predicted by He *et al.* [60].

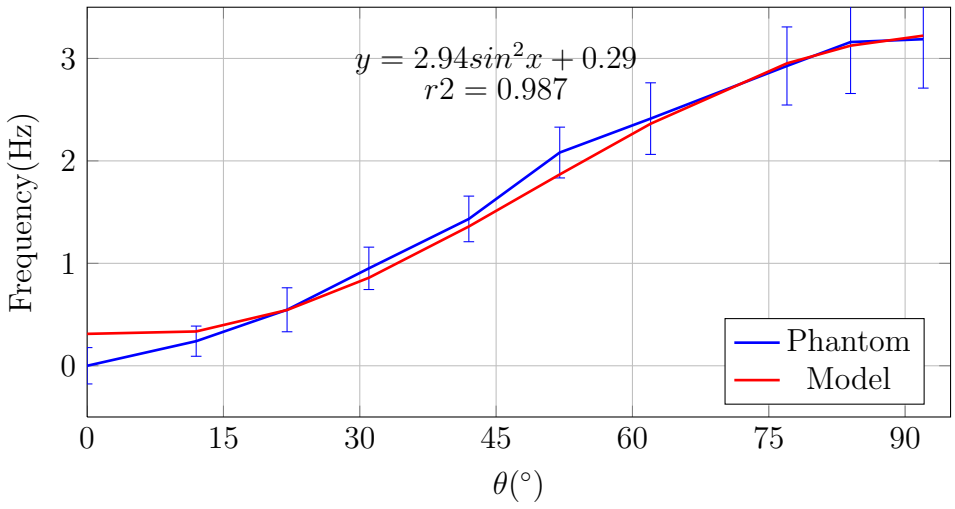

Figure 21: *Changes in resonance frequency with orientation to B_0. Blue line shows the experimental results with the error bars indicating standard error across pixels. Red line shows the model results.*

In the polypropylene fiber phantom, rotation of the phantom does not change the bulk shape of the phantom with respect to B_0. Therefore, the resonance frequency change observed can be attributed to changes in the microscopic field changes and not macroscopic field changes.

R_2* changes The measured R_2* shows a sinusoidal increase as θ (angle between long fiber axis to B_0) is increased (Fig. 22). The simulated R_2* over the range of θ follows a $sin^2\theta$ trend and matches the experimental results well. This $sin^2\theta$ trend is similar to that predicted by Yablonskiy *et al.* [172].

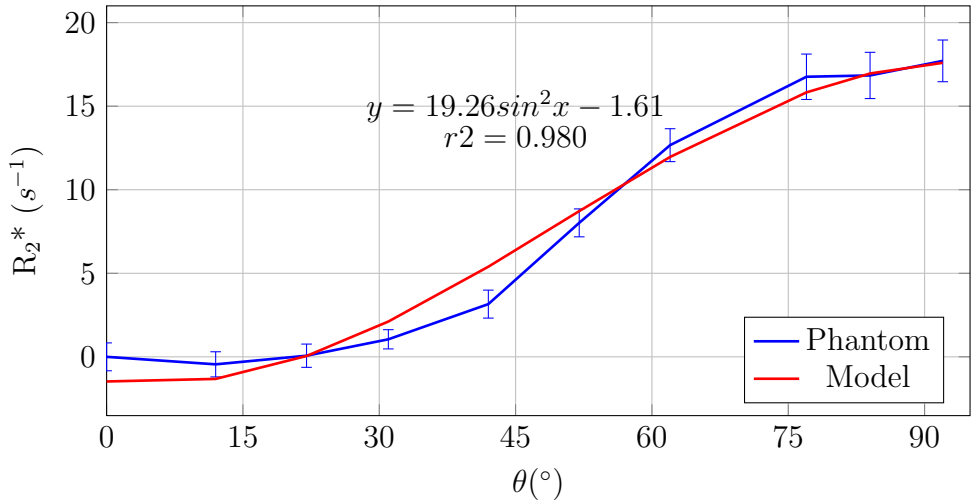

Figure 22: *Changes in R_2* modulation with orientation to B_0. Blue line shows the experimental results with the error bars indicating standard error across pixels. Red line shows the model results.*

The R_2 relaxation rates at the different orientations do not show any significant differences ($P = 0.1173$, one-way ANOVA test) indicating that the decrease is likely due to R_2' (since $R_2^* = R_2 + R_2'$). This is expected as the dipolar pattern generated by these long structures are at the maximum when perpendicular to B_0 thus generating a large distribution of local magnetic field perturbations. The R_2* trend shown here is similar to a study by Yablonskiy *et al.* [171] on

a fiber matrix phantom used to mimic the bone structure. Major differences from our phantom include the density of fiber packing and the bulk shape of the phantom.

According to the theories of R_2* and resonance frequency changes by Yablonskiy *et al.* [172] and He *et al.* [60], changes in R_2* and resonance frequency caused by parallel fibers are linked [83]. It can be seen that these two equations Eqns. [28-29] imply a direct relationship between the expected frequency shift and R_2*. More specifically, we can see that frequency shift is related to R_2* by a factor of 2π or about 6.28. From our results, the factor is 6.55 which is very similar to that predicted by theory. Differences may be attributed to the higher volume of perturbators used as compared to the low volume fraction of perturbator used in the theory by Yablonskiy *et al.* [172]. The polypropylene fibers were assumed to be perfectly parallel to each other and deviation from this assumption is also expected to contribute to deviation from predicted trend.

4.4 Geometric white matter model

In the polypropylene fiber study, we have previously shown that geometric modeling using analytical solutions for infinite cylinders can be used to model the magnetic field perturbation and hence GRE signal (GRE phase and R_2*) modulation in a system of high volume fraction susceptibility inclusions, which by themselves do not contribute to MR signal directly. The orientation dependence of GRE signal observed in the fiber phantom is similar to recent reports of dependence of GRE signal on WM orientation to B_0 [11, 33] supporting the idea that phase and T_2* variation in WM fibers is related to magnetic susceptibility effects associated with axonal micro-geometry.

To investigate the magnetic field perturbation caused in WM, we explicitly model the underlying WM microstructure. This is to allow the effects of high volume fraction of perturbators to be considered as well as to incorporate the effects of myelin water which unlike the polypropylene fibers do give off detectable MR signal. Diffusion effects can also be simulated on the frequency maps generated.

4.4.1 Formulation of WM model

A 2D geometric model of white matter is proposed here. The aim is to create a realistic representation of the WM microstructure. This 2D model represents a single plane transecting an ensemble of white matter fibers. Macroscopically, the model consists of a circular bundle of WM fibers surrounded by a reference medium (Fig. 23). The choice of the macroscopic shape of the WM fibers is important because it affects the overall magnetic field perturbation. A circular bundle will result in a relatively homogeneous macroscopic magnetic field perturbation across all the white matter fibers. If we were to let the magnetic susceptibility of the reference medium be equivalent to the mean susceptibility of the fiber bundle, we are effectively looking only at the microscopic magnetic field perturbation, similar to the discussion for the polypropylene phantom (see section 4.3.1 page 53). It should be noted that in reality, the macroscopic magnetic field perturbation differences at different locations due to the irregular bulk shape of the various brain structures will affect the effective magnetic field perturbation experienced. If we know the bulk shape of the object, we can approximate the frequency distribution due to this bulk shape using a forward model of the Fourier method of field calculation and convolve it with the microscopic frequency distribution from our model to obtain the effective frequency distribution (see section 4.2.2 page 55).

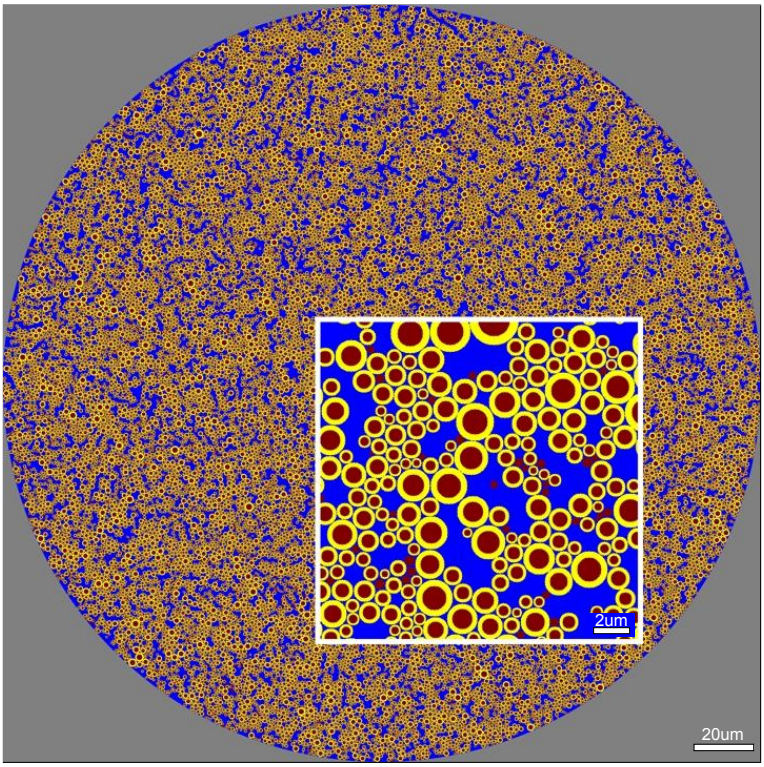

Figure 23: *2D representation of WM microstructure. WM is modeled macroscopically as a circular bundle embedded in a reference medium (gray region). Within the WM fiber bundle, the axonal compartment is represented in red, the myelin compartment in yellow and the extra-axonal space in blue. The white bar in the main cartoon represents a length scale of* $20\mu m$ *and the white bar in the zoomed-in box represents* $2\mu m$*.*

The WM fiber bundle is divided into 3 micro-compartments corresponding to axon, myelin and extra-axonal space (Fig. 23 white box). The axon whose length (1mm to 1cm [119]) is much longer than its diameter (1μm [119]) is approximated as a solid infinite circular cylinder. A nested cylinder is used to model the myelin sheath surrounding each axon. The myelin thickness around each axon follows a pre-defined mean g-ratio of 0.65 [4, 70] unless otherwise stated, where g-ratio is defined as the ratio of inner to outer diameter of the myelin sheath. The myelinated axons are densely-packed at random locations (using a circle packing algorithm [27]) with a mean volume fraction of WM fibers of 0.7 (assuming 0.2 extracellular space [114, 150] and 0.1 glia volume

fraction [85]). The WM fibers (axon+myelin) have a mean diameter of approximately $1\mu m$ and the fiber diameter follows a gamma distribution [1].

The extra-axonal space includes interstitial fluid, glial cells and blood vessels. It can be noted here that the geometry of the glial cells has not been modeled exclusively in this model. This may be justified partially by the relatively low volume fraction of the glial cells in WM. The assimilation of glial cells into the extra-axonal space also implicitly assumes that glia has the same susceptibility and MR relaxation properties as interstitial fluid. Blood vessels have also been excluded from our model due to their relatively low volume fraction in white matter.

The mean magnetic susceptibility of the myelin compartment is -0.08ppm [83, 92] and the axonal and extra-axonal compartments and reference space are set at 0ppm, unless otherwise specified. T_2 values at 3T for the myelin and extra-axonal compartments were set to $25ms$ and $75ms$, respectively [79]. To account for the reduced water fraction in myelin compartment, the proton density of the myelin compartment is set to half that of the axonal and extra-axonal compartments [154]. For realism, the magnetic susceptibility, g-ratio and WM fiber orientations are randomly varied from one axon to the next. The WM fibers are approximately parallel with slightly randomized orientation (angular variance of 5°).

The 2D model was simulated over a FOV of 0.35mm×0.35 mm to calculate signal for an area roughly comparable to a single MRI pixel. A high resolution grid space was used to ensure that the frequency perturbation pattern for each axon is sufficiently represented. After considering the trade-off between accuracy and computational feasibility, the grid was chosen such that 28×28 grid points covers $1 \times 1\mu m^2$ (exactly framing an axon of median diameter)

and the simulated FOV comprises approximately 7000×7000 grid points with 50,000 axons.

The important parameters used in the WM are summarized in the table below

g-ratio	0.65	VF	0.7
	myelin	axon	extra-axonal
χ(ppm)	-0.08	0	0
T2(ms)	25	75	75
PD	0.5	1	1

Table 2: Parameters used in WM geometric model. VF refers to volume fraction of WM fiber (myelin and axon). PD refers to proton density. T2 values are at 3T.

Frequency perturbation by a single myelinated axon The frequency perturbation for a single myelinated axon can be calculated from the summation of the frequency perturbations generated by a solid infinite cylinder (Eqn. 22) and a nested infinite cylinder (Eqn. 27) representing the axonal and myelin compartments respectively.

For the axonal compartment with susceptibility difference $\Delta\chi_{ax}$ ($\Delta\chi_{ax} = \chi_{ax} - \chi_{ea}$, where ax and ea denote the axonal and extra-axonal compartments respectively) and radius R_{ax}, the frequency perturbation comes only from the solid cylinder since the frequency perturbation from the nested cylinder is zero

$$\Delta f_{ax}(r) = \frac{1}{2} B_0 \gamma \Delta\chi_{ax} \left[cos^2\theta - \frac{1}{3} \right] \tag{30}$$

For the myelin compartment with susceptibility difference $\Delta\chi_{my}$ ($\Delta\chi_{my} = \chi_{my} - \chi_{ea}$, where my denotes the myelin compartment) and external radius R_{my}, the frequency perturbation comes from the body of the nested cylinder and that outside of the solid cylinder.

$$\begin{aligned} \Delta f_{my}(r) = \frac{1}{2} B_0 \gamma \Delta\chi_{my} \left[cos^2\theta - \frac{1}{3} - sin^2\theta cos2\phi \left(\frac{R_{ax}}{r} \right)^2 \right] \\ + \frac{1}{2} B_0 \gamma \Delta\chi_{ax} sin^2\theta cos2\phi \left(\frac{R_{ax}}{r} \right)^2 \end{aligned} \tag{31}$$

For the extra-axonal compartment, the frequency perturbation is the sum of fields from outside both the nested and solid cylinders.

$$\begin{aligned} \Delta f_{ea}(r) = \frac{1}{2} B_0 \gamma \Delta\chi_{ax} sin^2\theta cos2\phi \left(\frac{R_{ax}}{r} \right)^2 \\ + \frac{1}{2} B_0 \gamma \Delta\chi_{my} sin^2\theta cos2\phi \left[\frac{R_{my}^2 - R_{ax}^2}{r^2} \right] \end{aligned} \tag{32}$$

The final expressions for the frequency perturbation caused by a myelinated axon is given below (see Fig. 10 for coordinate system).

$$\Delta f_{ax} = \frac{1}{2} B_0 \gamma \Delta\chi_{ax} \left[cos^2\theta - \frac{1}{3} \right] \tag{33}$$

$$\Delta f_{my} = \frac{1}{2} B_0 \gamma \{ \Delta\chi_{my} \left[cos^2\theta - \frac{1}{3} \right] - [\Delta\chi_{my} - \Delta\chi_{ax}] \left(\frac{R_{ax}}{r} \right)^2 sin^2\theta cos(2\phi) \} \tag{34}$$

$$\Delta f_{ea} = \frac{1}{2} B_0 \gamma sin^2\theta cos(2\phi) \{ \Delta\chi_{my} \left(\frac{R_{my}}{r} \right)^2 - [\Delta\chi_{my} - \Delta\chi_{ax}] \left(\frac{R_{ax}}{r} \right)^2 \} \tag{35}$$

For a given WM fiber, the frequency perturbation contribution is calculated at every grid point by selecting between Eqns. [33–35] depending on which compartment the grid point lies in with respect to that axon, and the total field at a given point is the summation of field contributed by all axons. WM fiber orientations were varied by changing θ, which is an approximate and simplistic method for adding slight angular variation to an otherwise perfectly parallel fiber system. Thus, although the axons are simulated as perfect circles in the simulation, the field effects reflect a narrow range of orientations. Simulation was performed using Matlab (R2010a, Mathworks, Natick, MA) and requires a total processing time for one simulated FOV of about 1 hour when run parallel on a 100-node cluster.

4.4.2 Basic white matter model predictions

Here, we demonstrate the use of the WM model to simulate the frequency distribution from the WM model at 3T with the WM fibers orientated at 90°

to B_0. The simulated frequency distribution (corresponding only to the microscopic field perturbation) is shown in Fig. 24a. The myelin compartment shows a double peak distribution with a shifted mean phase due to the susceptibility difference between the axonal/extra-axonal and myelin compartments. The axonal and extra-axonal compartments both show single peak frequency distributions centred at the same mean frequency. The extra-axonal compartment can be seen to display a wider distribution of frequency compared with the axonal compartment.

The simulated GRE signal magnitude decay and phase evolution curves are shown in Figs. 24b and c. By fitting a mono-exponential curve to the signal magnitude decay, it can be seen that the decay curve can be mostly described by a mono-exponential function but there does exist an observable deviation from mono-exponential decay of approximately 2% of the original signal magnitude (Fig. 24d). The phase evolution can be seen to differ from a linear function, which is further confirmed by a linear fitting to the phase evolution curve (Fig. 24e).

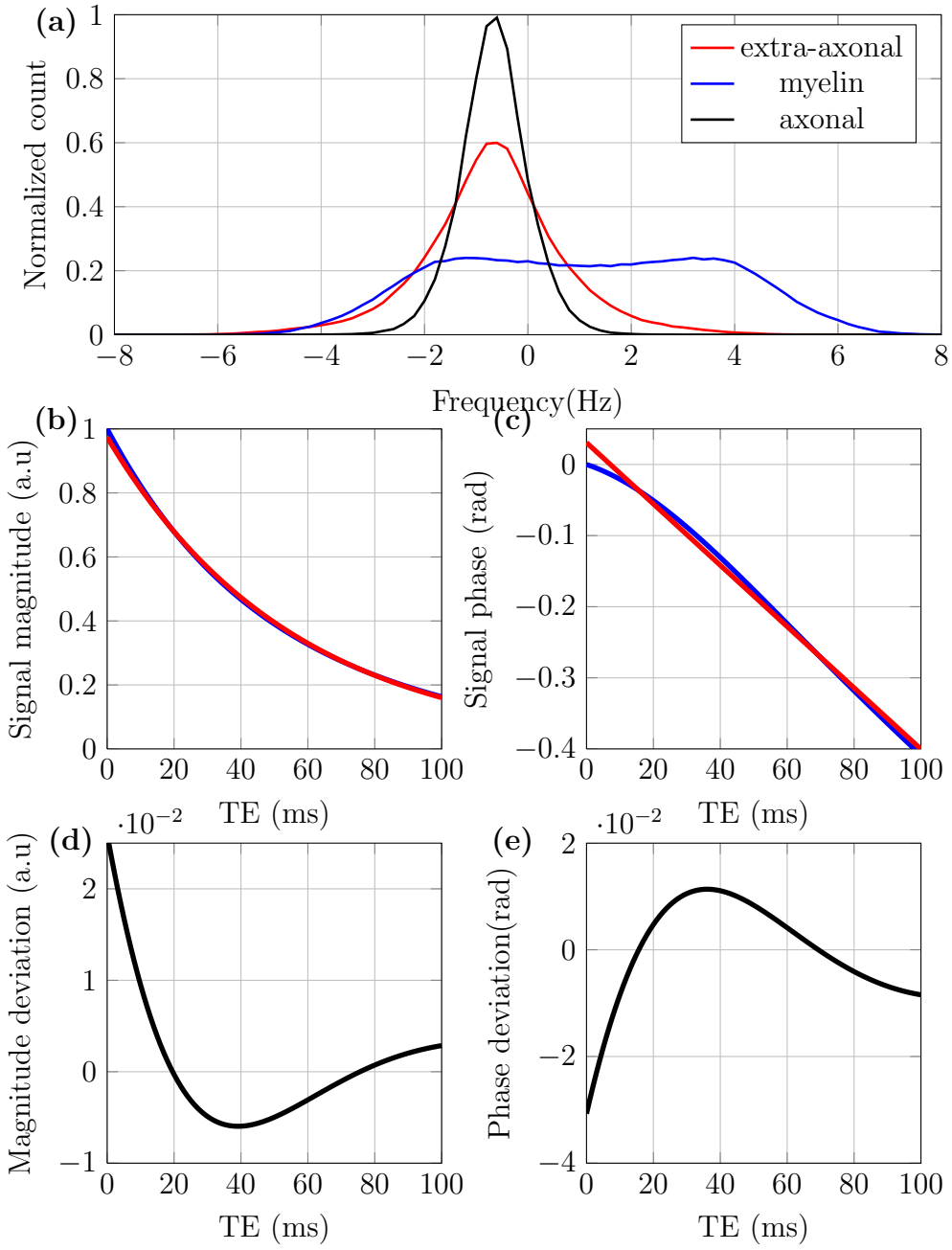

Figure 24: *WM model simulation of microscopic magnetic field perturbation when WM fibers are oriented at 90°. (a) Frequency histogram of the different compartments. (b) Signal magnitude decay with time (Blue line). Red line represents mono-exponential fit to decay curve. (c) Phase evolution with time (Blue line). Red line shows linear fitting to phase evolution curve. (d) Deviation of magnitude decay from mono-exponential decay. (e) Deviation of phase evolution from linear evolution.*

Deviation from mono-exponential decay Various sources can contribute to the deviation of the T_2* signal magnitude decay from mono-exponential decay. First, it can be clearly seen that the frequency distributions in each of the compartments have different widths, implying the presence of multiple species with different T_2'. This is coupled to the different T_2 of the different compartments. It would be tempting to model this as a simple sum of multiple exponential decays [35]. However, this contribution is further complicated by the presence of frequency shifts between the compartments, which in our case would correspond to the frequency shift between the myelin compartment and the other 2 compartments. van Gelderen *et al.* [155] have shown the improved fitting obtainable by including frequency shifts between compartments in their multiple exponential signal decay model. Another source of deviation from mono-exponential decay may be the deviation of the distribution itself from a Lorentzian distribution. In our model, it can be seen that the myelin compartment with its dual rounded peaks cannot be modeled as a single Lorentzian function.

Deviation from linear phase evolution Non-linear phase evolutions can originate from a couple of scenarios. Firstly, it can be caused by an asymmetric frequency distribution. It can be seen in future examples that when the frequency distribution is asymmetric due to specific packing patterns that lead to biased sampling of the underlying magnetic field, the resultant phase evolution is non-linear. Secondly, it can also be the result of the presence of multiple frequency shifted distributions with different decay rates. Since the effective frequency shift is the weighted contribution from the frequency distribution in each compartment, the difference in decay rate will result in an unequal weighting as time progresses. From the frequency histogram (Fig. 24a), it can

be seen that each of the individual compartments have a symmetrical shape. However, due to the frequency shift in the myelin compartment, there is an asymmetry in the overall frequency distribution. The shifted myelin compartment also has a different decay rate due to differences in both R_2 and R_2'. The interplay between these asymmetric frequency distribution and multiple T_2 species modulates the observed deviation from linear phase evolution.

Previous models have looked mainly at R_2* and phase changes by treating WM as a homogeneous bulk material with a characteristic mean susceptibility value. Those models do not predict the presence of the signal deviations that are observed in our geometric model.

4.4.3 Effects of tissue parameters

Other than the geometry of the different compartments that makes the WM microstructure, other factors can affect the simulated frequency perturbation and/or the simulated GRE signal. These factors will be discussed next.

Diffusion The static dephasing regime was assumed for the simulation results shown thus far. To investigate the effect of diffusion on the simulation results, Monte Carlo simulation was performed on 50,000 spins. Spins were randomly placed in the 2D frequency map corresponding to a fiber orientation of 90° (which results in the largest magnetic field perturbations and therefore greatest sensitivity to diffusion). Each spin undergoes a random walk with compartment-specific diffusion coefficient. The diffusion coefficient of spins in the axonal and extra-axonal compartments was set at $1\mu m^2 ms^{-1}$ [26] and spins present in the myelin are assumed to be stationary. All boundaries are impermeable and spins are reflected at the boundaries (by treating the bound-

aries as being perpendicular to the 2D plane). The effects of varying diffusion coefficient on the GRE signal magnitude and phase at different echo times was investigated.

Simulation results (Fig. 25) show very similar GRE magnitude decay and GRE phase evolution curves for simulations with and without diffusion. These simulations suggest that the change in the signal due to diffusion is relatively small and should not significantly affect the simulations calculated without diffusion effects (i.e., the static dephasing regime is a sensible approximation). In addition, the simulations demonstrate that the dependence on diffusion coefficients is negligible for the range of values found in white matter (0.1-1 $\mu m^2 ms^{-1}$), indicating that the orientation dependence should not be driven by preferential diffusion along axons.

The assumption of negligible diffusivity in myelin is important to this result, as the myelin sheath is the region of largest field heterogeneity. MRI studies have demonstrated that diffusion within myelin is lower than intra- or extracellular diffusion by at least a factor of two in peripheral nerves [6], while a recent microscopy study of myelin in functional axons concluded that diffusion is "profoundly slower" in axons in the central nervous system compared to peripheral nerves [157]. These studies would suggest that negligible diffusion within myelin is a reasonable assumption.

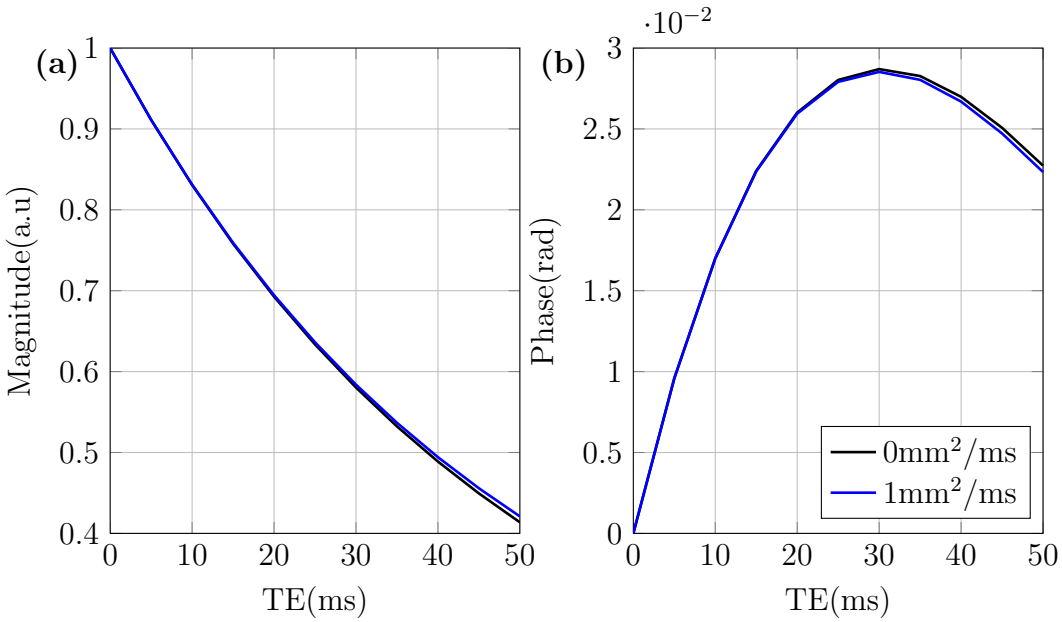

Figure 25: Effects of diffusion

Magnetic susceptibility In general, the simulated GRE signal magnitude and phase are dependent on the magnetic susceptibilities of the various compartments. The volume magnetic susceptibility of a bulk object can be accurately measured using a magnetic susceptometer (e.g. Evans balance [39]). Biological samples such as red blood cells can also be extracted from the body, purified and its magnetic susceptibility measured. Theoretically, we can isolate the myelin sheaths from brain samples and then measure its magnetic susceptibility, however, such a measurement requires high technical proficiency and is rarely performed [133]. Also, the molecular structure of the isolated compartment may change *ex vivo* and is thus not a good approximation of its *in vivo* property.

Another method would be to approximate the volume magnetic susceptibility of the WM compartments from the volume fraction and magnetic susceptibility of the constituent biological materials (e.g. the different types of proteins

and lipids) [60]. This method would require good estimates of the relative composition of the different biological materials in the WM compartments. There is also the assumption that the difference in the molecular structure of the constituent materials *in vivo* and *ex vivo* does not affect the magnetic susceptibility. This is unlikely to be true especially for the myelin compartment in which the lipids in the myelin sheaths are highly ordered and its magnetic susceptibility will be different from a solution of constituent lipids.

The magnetic susceptibility of the myelin compartment used in our model was estimated from literature values. The estimated -0.08 ppm is within the range of χ_{my} values proposed by other authors. Lee *et al.* [83] proposed a value of between -0.089ppm and -0.068ppm. A value of -0.0825ppm can be deduced from the paper by Liu *et al.* [92] if the myelin volume fraction is assumed to be 16%. However, it should be noted that these values proposed by the other authors were derived assuming the validity of more generic signal decay models. Lee *et al.* assumed that GRE phase changes can be explained by the Lorentz cylinder theory and R_2* changes can be explained by the parallel cylinders signal decay theory. Liu *et al.* on the other hand assumed that the underlying microstructure is homogeneous in using QSM to quantify the susceptibility.

To investigate this dependence of the simulated GRE signal on magnetic susceptibility for our relatively complicated geometry, the GRE signal phase and magnitude was simulated for a range of magnetic susceptibilities for fibers oriented at 0° to B_0. The magnetic susceptibilities of myelin and axonal compartments were independently varied from -0.2 ppm to 0.2 ppm (i.e., ranging from diamagnetic to paramagnetic) while fixing the magnetic susceptibility of extra-axonal compartment at 0 ppm. TE is 20ms and all other modeling pa-

rameters are the same as Table.2. The simulated results are shown in Fig. 26.

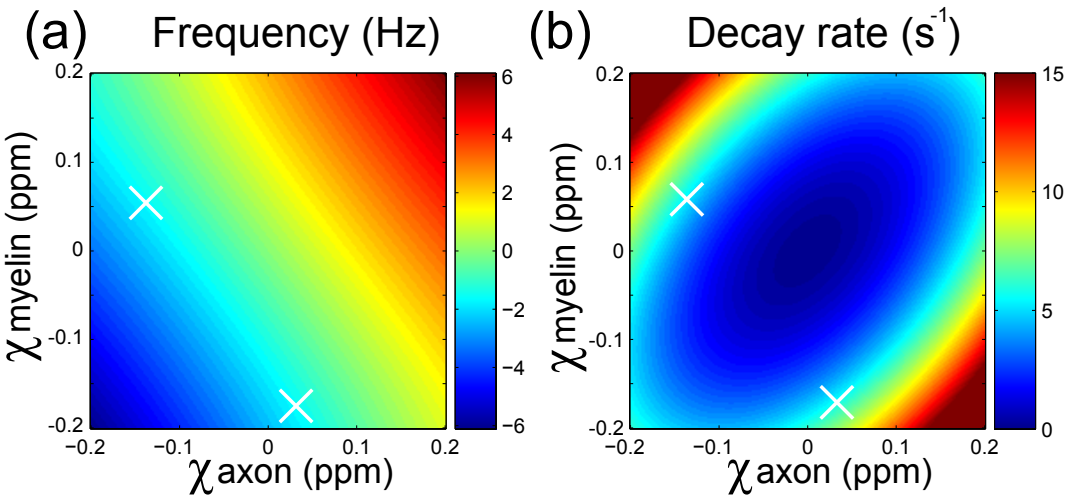

Figure 26: *The effect of varying susceptibility values for χ_{my} and χ_{ax} on resonance frequency and R_2*. White crosses represent 2 distinct pairs of χ_{ax} and χ_{my} that can create the same resonance frequency and R_2*.*

Both frequency and decay rate plots show significant changes with χ_{my} and χ_{ax}. Fig. 26a shows that there exists a range of values of χ_{my} and χ_{ax} (along in an oblique line in the $\chi_{my} \times \chi_{ax}$ plane) that would create the same calculated phase. This suggests the intuitive result that the phase is driven by $\chi_{my} + \chi_{ax}$ (for a fixed extra-axonal susceptibility, volume fraction, etc). Likewise, Fig. 26 b shows that there exists a range of values of χ_{my} and χ_{ax} (which lies in an ellipse in the $\chi_{my} \times \chi_{ax}$ plot) that would create the same calculated decay rate.

These 2 observations imply that for an observed set of R_2* and frequency changes in a single experiment, the values of χ_{my} and χ_{ax} are generally not unique since the intersection between the oblique line and ellipse will yield 2 distinct solutions (see white crosses in Fig. 26) except at the circumference of the ellipse. The elliptical trend observed in the decay rate plot also shows that the decay rate is primarily driven by the difference in susceptibility of myelin and axonal water (extremes at the upper left and lower right corners of

Fig. 26b), with a more minor effect of the relative offset of both to extra-axonal water (upper right and lower left corners). These dependencies are expected to vary with orientation as well as with different values of χ_{ea}.

T_2 of myelin compartment The susceptibility-shifted myelin compartment plays an important role in modulating the signal magnitude and phase behavior. However, the non mono-exponential decay and non-linear phase accrual will also be affected by the fast decay of myelin signal [167]. As such, it is expected that changing the T_2 of the myelin compartment would also change behavior of both the signal phase and magnitude decay. From Fig. 27, it could be seen that increasing T_2 of myelin shifts the peak of the phase curve to the right and produces a larger phase change. The shapes of the magnitude decay curve change with increasing T_2 . At shorter T_2 , a faster decay at the early time point can be seen. These results indicate that both the T_2 and magnetic susceptibility of myelin modulates the signal temporal dynamics. However, T_2 cannot create the profound orientation dependence observed in the temporal dynamics of both phase and magnitude signal, indicating that susceptibility plays a crucial role in the observed temporal dynamics.

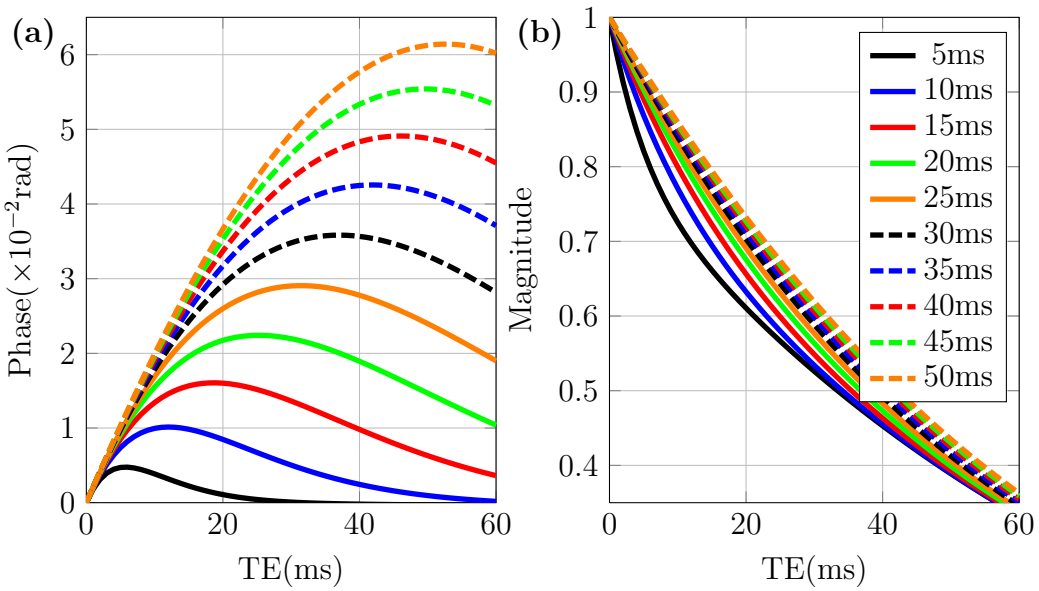

Figure 27: *Effects of varying myelin T_2. (a) shows the change in signal phase over time for a range of simulated T_2 of myelin. (b) shows the change in signal magnitude over time for a range of simulated T_2 of myelin*

4.5 Conclusion

We have introduced a geometric model of white matter from which the magnetic field perturbation and the subsequent effects on GRE signal behaviour can be modeled. This provides a platform to study the link between the actual WM microstructure and observed GRE signal changes. We have tested the validity of using a geometric model to model GRE phase and R_2* changes in a system of high volume fraction of perturbators by using a polypropylene fiber phantom and studying the orientation dependence of the GRE signal. The magnetic field perturbation caused by our WM model has been shown and the effects on GRE signal magnitude and phase has been discussed. Our model predicts deviation of the GRE signal from conventional GRE signal from a homogeneous sample, specifically, deviation of signal magnitude decay from mono-exponential and deviation of phase evolution from linearity. We have also discussed some of the important aspects of the model such as the effects of packing.

The following 2 chapters will focus on studying changes in GRE signal due to specific changes in WM microstructure. In the next chapter, we look at dependence of GRE signal on the orientation of WM fibers to B_0 in a human study at 3T. In the chapter after the next, we look at the effects of myelination changes in a rodent study at 7T both *in vivo* and *ex vivo*. In both chapters, we compare experimental results with simulations from the geometric WM model.

5 B_0 orientation effects

Orientation dependence of GRE signal magnitude and phase have been reported by various groups in recent years [11, 33, 60, 82, 132, 169]. However, the source of this orientation dependence is not well known. Various mechanisms have been used to explain the observed experimental trends but most of these focus only on a limited aspect of the signal behaviour. We used the geometric WM model presented in the previous chapter, in which compartmentalized susceptibility produces a microscopic pattern of magnetic field perturbations, to predict GRE signal changes due to orientation differences. Comparison of GRE signal predictions from this model to measured GRE signal from human subjects demonstrated good agreement. This work has recently been published in NeuroImage [24]. I would like to acknowledge the assistance provided by Dr Sean Foxley and Dr Karla Miller in the MR image acquisition.

5.1 Introduction

Large signal heterogeneity has been previously reported within WM fibers in T_2*-weighted images at 7T [89]. The ability to discern large fiber bundles e.g. between the splenium and tapetum led to postulations of possible sources of this contrast. These include differences in iron concentration [55], myelination [83] and fiber orientation [11, 33, 169]. In particular, the relation between fiber orientation and changes in GRE signal e.g. T_2* and GRE phase has received widespread attention.

Wiggins *et al.* [169] first explicitly demonstrated the orientation dependence of T_2* in WM using a macaque brain at 7T. In their experiment, Wiggins *et al.* showed that signal intensity in T_2*-weighted images of the cingulum changes when the orientation of the WM fiber tract changes with respect to B_0 as the macaque's head position was changed. Schafer *et al.* [132] reported similar effects on T_2* in the human brain. In addition, frequency shifts were investigated and geometric modeling of the white matter fiber bundles as solid cylinders was performed to simulate the frequency shift. In a study at 1.5T, Henkelman *et al.* [62] reported that T_2* in the white matter does not depend on orientation to B_0, which may reflect weaker susceptibility effects at low field strength. Interestingly, Li *et al.* reported no observable dependence of T_2* on orientation at 7T [88] by changing the orientation of the human brain through the tilting of the head at an angle of about 27°. This lack of difference may partially be attributed to insufficient deviation in the orientation of the WM fiber tract of interest [11]. In another study, Cherubini *et al.* [25] observed differences in T_2* between clusters of WM voxels oriented parallel and perpendicular to B_0. However, it was also observed that nearby fibers having the same orientation can have large variations in relaxation rates. Also, for

fibers with different orientations, similar relaxation rates have been observed. More detailed studies have been recently performed to look at this orientation dependence effect in WM. Bender *et al.* [11] looked at the whole brain correlation of WM fiber orientation obtained using DTI with measured R_2* and concluded significant effect of orientation on R_2*. An additional experiment looking at head tilting to achieve orientation changes of up to 45° also reported significant differences between R_2* at different head positions. Denk *et al.* [33] used a similar method to correlate R_2* with fiber orientation obtained from DTI and reported similar trends.

Dependence of GRE phase contrast in WM on orientation to B_0 is less studied. GRE phase contrast in WM has been recently proposed by He *et al.* [60] to be orientation dependent. To explain for the lack of phase contrast between WM and CSF in the motor cortex despite significant differences between their magnetic susceptibilities, He *et al.* introduced a concept of a Lorentz cylinder to incorporate the effects of longitudinal magnetic field perturbators e.g. filaments and myelin sheaths. This concept introduces an orientation dependence to the microstructural magnetic field perturbation. In the study performed by Denk *et al.* [33], GRE phase was also correlated to fiber orientation in addition to R_2*. Lee *et al.* [82] investigated the orientation dependence of GRE phase using *ex vivo* WM fiber tracts. By negating bulk shape contribution from their experimental setup, Lee *et al.* observed a non-local effect from the rotated WM fibers and proposed that susceptibility anisotropy was responsible for the orientation dependence.

Several mechanisms have been proposed to explain the observed signal properties. These include approximating GRE signal decay using a parallel infinite cylinders model [172] ,which is characterized by low perturbator volume frac-

tion and single compartment signal contribution, and attributing GRE phase changes to Lorentz cylinder effect [60] or susceptibility anisotropy [82, 91]. These models generally attributed the orientation dependence effects to the microenvironment, but without explicitly modeling the microstructure. While being able to provide closed-form expressions for the orientation dependence of signal phase, these models were designed to explain a limited range of signal behaviors.

In the previous chapter, we introduced an explicit multi-compartmental geometric model of the WM, which encapsulates magnetic and geometric properties of the underlying tissue microstructure, that can be used to investigate the contribution of the tissue micro-architecture in modulating GRE signal properties. The power of this approach is that it predicts the entire frequency distribution contained within a voxel, capturing the full richness of information in this distribution, thus providing a simple but powerful approach to predict the full spectrum of GRE signal characteristics (i.e. both low- and high-order moments [109, 155])

In this chapter, we study the dependence of WM GRE signal (both phase and magnitude) on orientation of the underlying WM fiber to B_0 in human volunteers at 3T. A method similar to Bender *et al.* [11] and Denk *et al.* [33] is used to complement GRE results with orientation information obtained from DTI. We investigate both low-order moments of the GRE signal (e.g. R_2* and resonance frequency) and higher-order moments such as non-linear phase [131, 136, 164] and non-mono-exponential magnitude time courses [155]. The WM model is then used to predict the dependence of the full GRE signal behaviour.

5.2 Methods and materials

5.2.1 Geometric model simulation

The geometric WM model described in Chapter 4.4 was used to simulate the frequency perturbation at a range of orientations (θ) with respect to B_0 (by rotating B_0 relative to the simulated 2D plane). The magnetic susceptibility of the reference medium was set to be the same as that of the extra-axonal compartment (i.e. $\Delta\chi = 0ppm$), thereby assuming a cylindrical bulk shape for the WM fiber bundles [33, 60]. A forward model using parameters from literature is used in the geometric model to show that the geometric model can be used to generate similar trends observed in experiments. See Table. 2(page 75) for a summary of important parameters used in the model.

5.2.2 MRI acquisition and data processing

Seven healthy volunteers were scanned using a 3T Siemens Trio MRI scanner with a 12-channel head coil. A 2D multi-echo GRE pulse sequence was used to obtain phase and magnitude images at 128 echo times (FOV $192 \times 192mm^2$; matrix 96×96; 5 axial slices with $12mm$ separation; flip angle 10 °; TR $1.5s$; TE $4 - 260ms$; ΔTE $4ms$; scan time $25mins$). The R_2* value was estimated with least-squares linear fitting to the logarithm of the magnitude images for echoes from 4 to $148ms$. Unwrapping of the signal phase was performed on a voxel-by-voxel basis in 1D (Matlab) on echoes acquired from 4 to $60ms$, and fed into least-squares linear fitting to determine voxel mean frequency. Background field variation was removed by subtracting a low pass filtered phase image from the original phase image (5×5 mean filter). DTI data ($2 \times 2 \times 2mm$, b=$1000s/mm^2$, 30 directions) was acquired in the same session

and used to determine the orientation of WM fibers relative to B_0, and to create a WM mask (FA>0.3). Eleven bins were used to classify the orientation of the WM fibers with bin-width proportional to $sin\theta$ (to avoid a paucity of voxels contribution at the lowest angles). To characterize the signal evolution over time, the deviation from linear phase and mono-exponential magnitude decay were calculated by subtracting off the fitted linear phase and R_2* decay from the phase and magnitude time courses, respectively. This was calculated separately for the average time courses corresponding to approximately parallel $(0° - 15°)$ and perpendicular $(75° - 90°)$ WM fibers.

We compared several model predictions to GRE signal measured in seven volunteers at 3T. In the first instance, we considered the orientation dependence of resonance frequency and R_2* . The predominant angle of WM fibers to B_0 was extracted from diffusion tensor imaging (DTI) data acquired in the same scan session (see Fig. 28). We also studied the time evolution of the signal phase and magnitude [131, 136, 155, 164]. Model predictions for the temporal deviation from linear phase and mono-exponential decay were compared to measurements.

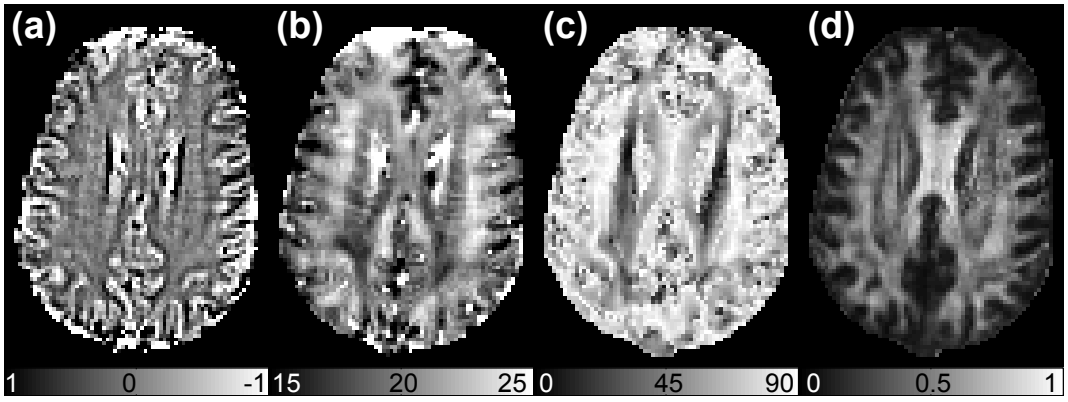

Figure 28: *In vivo dependence of resonance frequency and R_2* on orientation of WM fibers to B_0. (a) Frequency map. (b) R_2* map. (c) Map of angle between principle eigenvector with B_0 from DTI. (d) Fractional anisotropy (FA) map.*

5.3 Results and discussion

5.3.1 Frequency modulation with orientation

Significant difference ($P < 0.001$) between the mean resonance frequency for each group of WM pixels was obtained using a one-way ANOVA test. Fig. 29 shows the measured and simulated dependence of the signal resonance frequency on orientation to B_0. The measured resonance frequency of WM fibers approximately perpendicular to B_0 ($\theta \approx 90°$) is positive relative to WM fibers approximately parallel to B_0 ($\theta \approx 15°$), in agreement with previous studies [25, 33, 82]. The resonance frequency increases with θ up to a peak between $45° - 65°$, and then decreases after the peak (Fig. 29a).

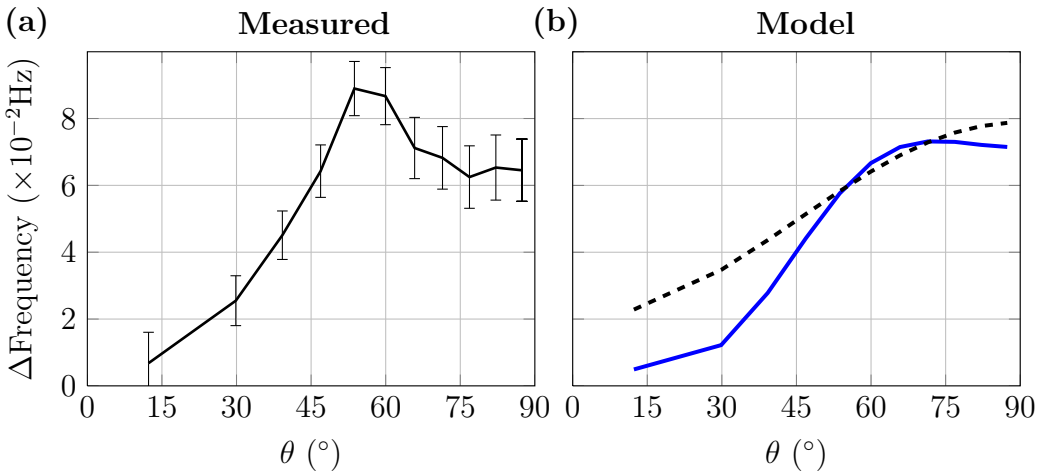

Figure 29: *Frequency modulation with orientation to $B_0(\theta)$. (a) Measured frequency modulation. Error bars denote standard error. (b) Simulated frequency modulation. Blue line shows the simulated frequency modulation from the geometric WM model. Black dashed line shows the best fit $sin^2\theta$ of the measured data.*

A similar trend was reported previously by Denk *et al.* [33]. They reported a GRE phase change of 0.02 rad at a TE of 20ms which translates to a frequency change of about 0.16Hz which is about twice of our measured frequency

change of 0.08Hz. Discrepancies can be attributed to difference in the phase processing procedure (e.g. background phase removal procedure) and acquisition procedures (e.g. resolution of scan and the brain FOV).

The orientation dependence of resonance frequency predicted from our model (blue line in Fig. 29b) exhibits a similar peak, albeit less pronounced and at a slightly larger angle $65° - 75°$. Most strikingly, this forward model (using parameters taken from literature) predicts a comparable range of frequencies as the measured data.

Two models have been proposed for orientation dependence of GRE signal phase: the generalized Lorentz cavity [60] and susceptibility anisotropy [82]. The generalized-Lorentz model predicts a $sin^2\theta$ dependence induced by the presence of cylindrical, susceptibility-shifted inclusions. Denk *et al.* used this generalized-Lorentz model to fit their data but they required an ad hoc scaling of the frequency axis to account for the observed phase peak [33]. Denk *et al.* attributed this deviation from $sin^2\theta$ dependence to the averaging of signal phase over multiple brain regions. In our model, the deviation from $sin^2\theta$ can be explained in terms of the presence of multiple susceptibility shifted compartments. In the generalized-Lorentz model, signal from a single compartment is considered (i.e .outside the magnetic field perturbators). In our model, there is signal contribution from frequency shifted myelin water. This signal interferes with the signal from the axonal and extra-axonal water leading to this deviation from $sin^2\theta$ dependence.

The susceptibility anisotropy model assumes an orientation dependence of the magnetic susceptibility itself, which can occur in certain biological structures like membranes, and also follows a $sin^2\theta$ dependence. Fitting a $sin^2\theta$ dependence to the experimental data produces a poor fit (R^2=0.584, black dashed

line in Fig. 29b). Both the generalized-Lorentz and susceptibility-anisotropy models calculate the phase orientation dependence for a single compartment, which may in general contain fractional contributions from multiple species with varying susceptibility. Other than accounting for contributions from multiple microstructural compartments, our WM model also explicitly incorporates the micro-geometry of the WM compartments to provide a more accurate description of the orientation dependence effect.

5.3.2 R_2* modulation with orientation

Significant difference ($P < 0.001$) between the mean R_2* for each group of WM pixels was obtained using a one-way ANOVA test. Fig. 30 shows the measured and simulated dependence of R_2* on orientation to B_0. The experimental R_2* results exhibit a roughly sinusoidal increase with θ (Fig. 30a) spanning about 2 Hz which is in good agreement with other studies (2.8 Hz and 1.8 Hz reported by Bender *et al.* [11] and Denk *et al.* [33] respectively).

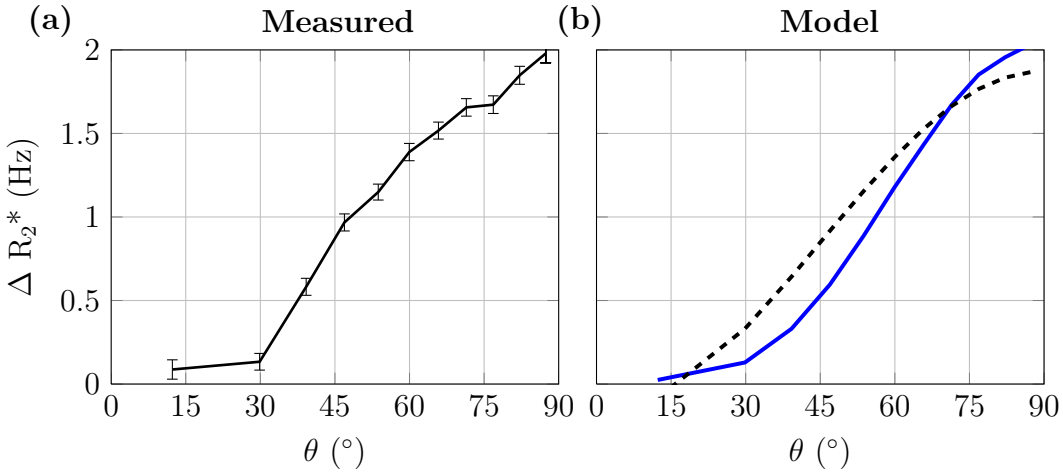

Figure 30: *R_2* modulation with orientation to $B_0(\theta)$. (a) Measured R_2* modulation. Error bars denote standard error. (b) Simulated R_2* modulation. Blue line shows the simulated R_2* modulation from the geometric WM model. Black dashed line shows the best fit $sin^2\theta$ of the measured data.*

The model simulation matches quite well with the experimental results (blue line in Fig. 30b). According to Yablonskiy *et al.* [172], parallel cylinders of susceptibility-shifted material are predicted to have a $sin^2\theta$ dependence (with the underlying assumption of low volume fraction), which produces a good fit to our data (adjusted $R^2 = 0.976$, black dashed line in Fig. 30b). However, at the smaller angles ($< 30°$) the change in R_2* with respect to angle as predicted by the $sin^2\theta$ trend is larger than our experimental data. The $sin^2\theta$ trend typically considers only the extra-cylinder component and at 0°, no signal decay due to magnetic field inhomogeneity would be expected . In our simulation, even at 0° the presence of susceptibility shifted frequencies cause an interference pattern that drives signal changes. Previous work on fixed brain at 7T has reported a $sin^4\theta$ dependence, which was attributed to myelin magnetic anisotropy [84]. Fitting a $sin^4\theta$ dependence corresponds to an adjusted R^2 value of 0.977. A p-value of 0.792 was obtained from a F-test comparing the fit with and without an additional $sin^4\theta$ dependence suggesting that our data at 3T does not display a significant $sin^4\theta$ dependence.

The simulated baseline R_2* value at $\theta \approx 15°$ is smaller than what was measured from the experiments (16Hz from our simulation vs 18.5Hz measured from our experiments), which likely reflects additional sources of signal decay which were not considered in our simulations (e.g., imperfect shim). In addition, the contributions from other substructures such as iron-rich oligodendrocytes and hemoglobin-bearing blood vessels were not explicitly modeled in our model. The inclusion of these structures would contribute further magnetic field perturbations, thereby shifting the baseline of R_2*, but is not expected to introduce orientation dependence. The approximately spherical shapes of the oligodendrocytes [119] suggest that their contribution would gen-

erate orientation-invariant magnetic field perturbations [54]. WM vasculature is generally aligned with the WM fibers, but has been reported to have insignificant contribution to phase contrast due to the low volume fraction [81,104,160].

5.3.3 Signal phase evolution

We investigated how the signal phase evolution deviates from linear phase accrual [136, 164]. Analysis of the experimental phase evolution against time revealed significant deviation of the measured phase from a linear relationship with echo time. The phase residuals (after subtraction of the linear fit) are approximately quadratic forms, with negative and positive coefficients for perpendicular and parallel WM fibers respectively (Fig. 31a). The geometric model predicts very similar trends with echo time, and replicates the difference between parallel and perpendicular WM fibers (Fig. 31b).

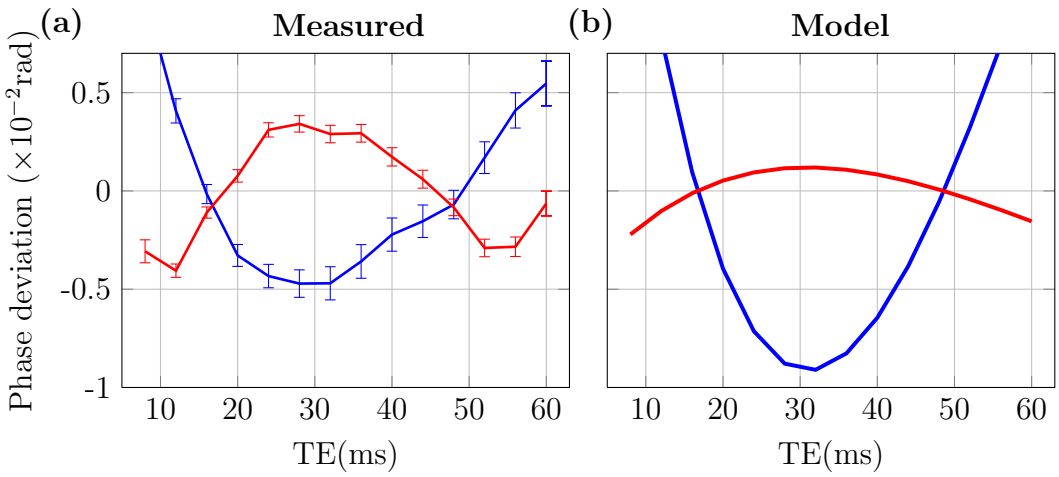

Figure 31: *Experimental and simulated deviation from linear phase evolution (signal phase minus linear fit). (a) Measured deviation. (b) Simulated deviation. Blue and red lines represent parallel and perpendicular WM fibers respectively.*

Linear phase evolution implies that there exists a central frequency about

which signal from positive and negative frequency offsets cancels at all time points. Deviations from this behavior indicate this cancellation does not happen, either because the frequency distribution is not symmetric or because R_2 signal decay correlates with frequency, either of which implies compartmentalization. Compartmentalization of R_2 (e.g., in myelin) will influence the shape of the signal phase evolution; however, the dependence on orientation indicates that susceptibility also plays a role in this effect (since R_2 is orientation independent [62]). This phenomenon illustrates an important difference between our model and the simpler approach of approximating the distribution from the field generated outside of a single cylinder characterized by a mean magnetic susceptibility: the latter model predicts a linear phase evolution, while ours encapsulates non-linear evolution.

Frequency difference mapping The presentation of non-linear phase evolution as the residual of a linear fitted line to the actual measured phase evolution shown above is a convenient way of observing deviation of the phase evolution from linearity, similar to observing deviation of the magnitude decay from mono-exponential decay. Alternate representations of this effect have been proposed by other groups in the form of frequency difference mapping [131, 136, 164, 165], which involves linear fitting phase corresponding to TE_1 with TE_2 to TE_n to form $(n-1)$ frequency readings. The frequency difference is then obtained by subtracting the first frequency (calculated from TE1 and TE2) from all the frequencies (calculated from TE1 and the later echoes). For a homogeneous sample in which no deviation from linear phase evolution is expected, the frequency difference across the different TEs are expected to be the same giving rise to a horizontal line. For non-linear phase evolution, deviation from a constant is expected.

5.3.4 Signal magnitude evolution

The residual time course of the signal magnitude (subtracting the R_2* fit) revealed significant deviation from mono-exponential decay (Fig. 32a), with different characteristic shapes for parallel and perpendicular WM fibers. Simulated results predicted similar trends (Fig. 32b).

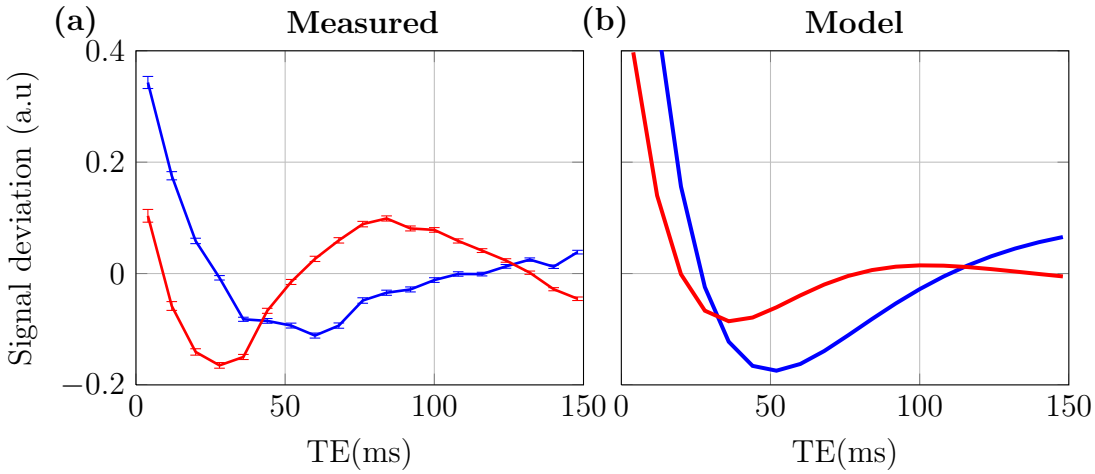

Figure 32: *Experimental and simulated deviation from mono-exponential decay (signal magnitude minus R_2* decay fit). (a) Measured deviation. (b) Simulated deviation. Blue and red lines represent parallel and perpendicular WM fibers respectively.*

Non mono-exponential behavior of GRE signal decay in WM has been previously reported [35, 155]. An early study attributed this behavior to the presence of a myelin water pool with a short T_2 and a larger water pool with longer T_2 corresponding to intra- and extra-axonal water [100]. More recently, it has been suggested that these water pools are also frequency shifted with respect to each other [155]. In our experiments, parallel and perpendicular WM fibers exhibit distinct oscillatory behaviors that are consistent with the presence of compartments with magnetic susceptibility differences. With respect to signal inflection points, the deviation curve for parallel WM fibers are

expanded in time relative to the perpendicular WM fibers, which may reflect a narrower frequency separation. Signal inflection points have also been shown previously to occur at shorter echo times as field strength increases, consistent with a susceptibility-driven effect [155]. The simulated signal decay from each individual compartment exhibits Gaussian-like decay at the early time points [172], which contributes to the deviation from mono-exponential decay, but is not the primary factor driving the shape of these curves (as indicated by a poor fit to a Gaussian). Low spatial frequency background gradients caused by poor shim and macroscopic susceptibility differences interfaces could have contributed to deviations from mono-exponential decay but there should not be any preferential modulation towards GM or WM.

5.3.5 Susceptibility anisotropy

Previous work has considered susceptibility anisotropy as a bulk property to explain orientation dependence [82, 83, 92]. Within our geometric model, this effect would operate at a compartmental level, most likely in the myelin [82]. We incorporated susceptibility anisotropy in the myelin compartment. Here, we assume the most basic form of susceptibility anisotropy which corresponds to a cylindrically symmetric susceptibility tensor with principal axis along the long fiber axis, which can be written as $\chi_{my}(\theta) = \chi_{iso} + \chi_{aniso} \times sin^2(\theta)$ [82], with $\chi_{aniso} = -0.04ppm$ (which is the susceptibility anisotropy measured on lecithin membranes using phase contrast microscopy [17]) and $\chi_{my}(90°) = -0.08ppm$. Susceptibility anisotropy results in a frequency modulation with a slightly reduced range of values, but the general trend remains, including the frequency peak between $65° - 75°$ (Fig. 33a). The resultant R_2* modulation is again similar, with susceptibility anisotropy altering the specific shape but preserving

the overall trends (Fig. 33b). These simulations suggest that, while susceptibility anisotropy is not inconsistent with our results, neither is it required to generate the general effects seen in the experimental data.

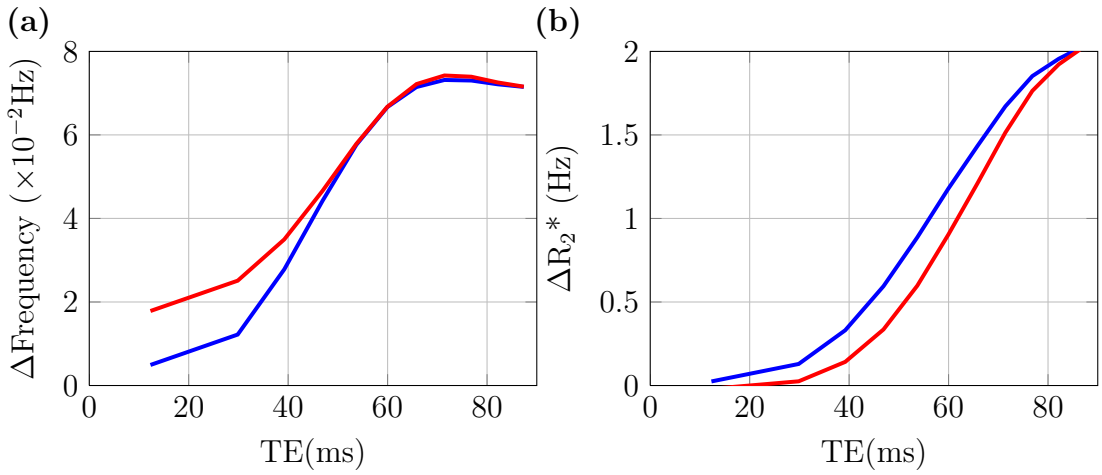

Figure 33: *Effects of susceptibility anisotropy on orientation modulation. (a) Simulated frequency modulation. (b) Simulated R_2* modulation. Blue line represents simulation without susceptibility anisotropy while red line represents simulation with susceptibility anisotropy.*

Recently, various authors have used more realistic representation of the susceptibility anisotropy in the myelin by considering the radial arrangement of the long lipid chains in the myelin sheath [131, 164]. This more realistic representation has not yet been implemented in our model and warrants future investigation into the effects of this form of susceptibility anisotropy on our simulated signal behaviour.

Quantitative Susceptibility Mapping The quantitative use of GRE phase measurements is limited due to the non-local effects of phase images. Quantitative susceptibility mapping (QSM) has been proposed to calculate the susceptibility distribution from frequency maps. This susceptibility map should provide a more local representation of the magnetic property of the underlying

tissue. This is achieved by performing the inverse of the 3D Fourier method to calculate the susceptibility distribution that can create a particular magnetic field perturbation. However, there is an underlying assumption that the Lorentz sphere assumption holds in the investigated volume. The orientation dependence of MR phase is thus translated to a change in susceptibility of the tissue, implying susceptibility anisotropy in WM tissue. It can be seen from our discussion (Chapter 5.3.6, page 105) that the orientation of longitudinal microstructures can modulate signal phase as well. The exclusion of the effects of such mechanism in QSM would require researchers to be mindful of such effects when interpreting QSM results in different WM regions.

5.3.6 Anisotropic cellular structure vs anisotropic susceptibility

Both anisotropic cellular structure and anisotropic susceptibility can lead to changes in resonance frequency that depend on orientation to B_0. However, their spatial effects are different. To demonstrate this we can look at the magnetic field perturbation resulted from cubes that represent the different mechanisms (Fig. 34). The magnetic field perturbation from the simulated cubes were calculated using the 3D Fourier method over a matrix size of 400x400x400 grid points.

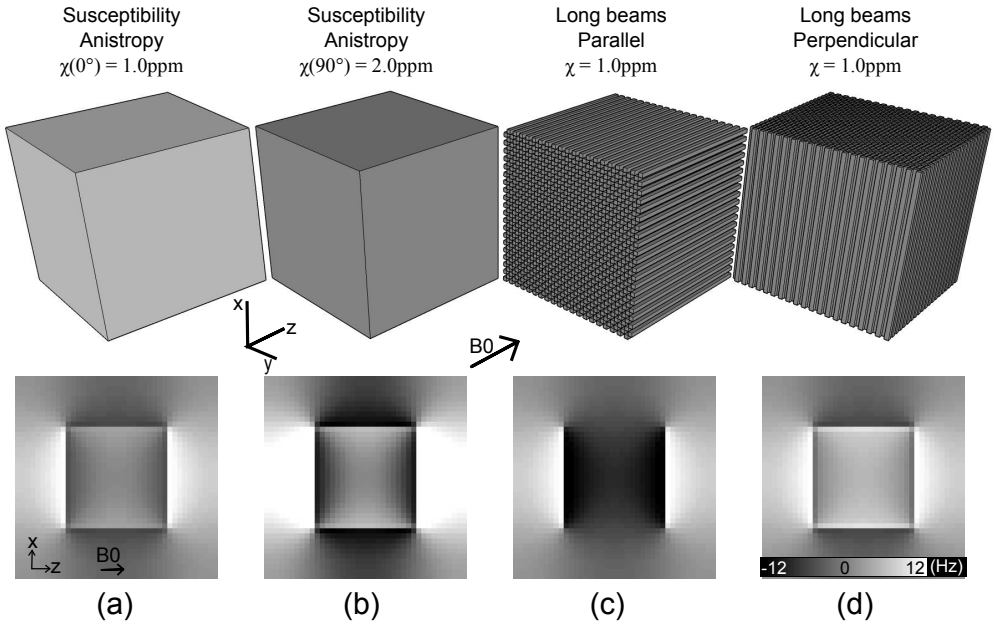

Figure 34: *Simulating frequency changes due to susceptibility anisotropy and microstructure. Solid cube with susceptibility anisotropy at (a) 0° and (b) 90°. Heterogeneous cube with long beams (c) parallel and (d) perpendicular to B_0. Upper row shows a 3D representation of the simulated volumes, bottom row shows corresponding simulated frequency maps.*

To demonstrate the effects of susceptibility anisotropy, we consider a solid cube (Fig. 34a,b) that is made of a material that displays magnetic susceptibility

anisotropy according to :

$$\chi(\theta) = \chi(0^\circ) + \chi_{aniso} \cdot sin^2\theta \tag{36}$$

where $\chi(0^\circ) = 1.0ppm$, $\chi_{aniso} = 1.0ppm$ and θ is the angle between principal susceptibility axis with B_0(susceptibility is assumed to occur in a single axis along an edge of the cube). This gives us a susceptibility value $\chi(90^\circ) = 2.0ppm$ (Fig. 34b) . We simulate changes in the frequency map when the susceptibility axis is oriented 0° to B_0 and when it oriented 90° to B_0. A line plot (Fig.35) across the midline of the frequency map shows that when the susceptibility value changes due to anisotropy, the frequencies both outside and inside the cubes changes. This change is not a constant shift but is a scaling of the frequency profile (Blue solid line vs blue dashed line).

To demonstrate the effects of anisotropic microstructure, we consider a cube made of smaller parallel long square beams (assumed not to contribute any signal) arranged in a regular alternate hexagonal pattern with a volume susceptibility $\chi = 1.0ppm$. Similarly, we simulate changes when the long axis of the beams are parallel (Fig. 34c) and when they are perpendicular (Fig. 34d) to B_0. By looking at their line plots, there is no change in the frequency pattern outside of the cubes which is expected since they have the same bulk shape and volume susceptibility. Within the cube, there is a constant shift in frequency. The amount of frequency shift is dependent on the actual geometry and arrangement of the microstructures, which in this case corresponds to a regular hexagonal packing of square beams.

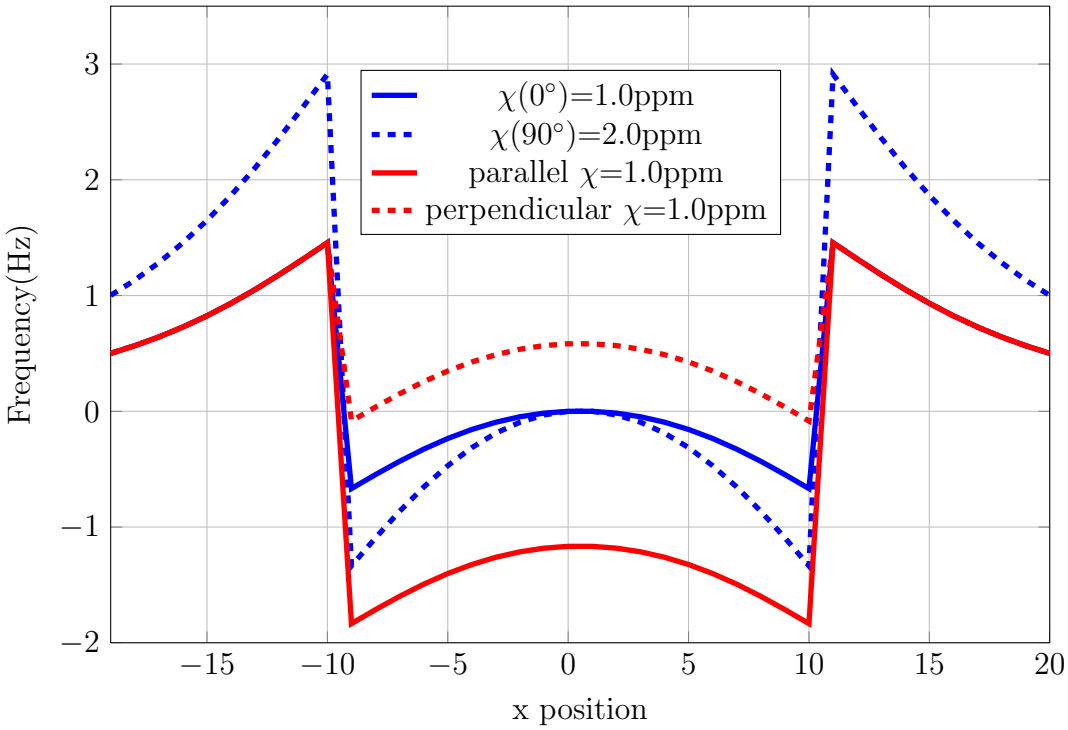

Figure 35: *Line plots of the frequency maps corresponding to the simulated volumes.*

Through our simulations, it can be clearly seen that the magnetic field perturbations caused by anisotropic cellular structure and anisotropic susceptibility result in distinctly different pattern of frequency modulation. Specifically, anisotropic cellular structures cause frequency shifts within the object only while anisotropic susceptibility causes frequency shifts within and beyond the object (i.e. non local). These simulations were designed such that we see the change caused by each individual mechanism separately. In real life, it is difficult to attribute the source of frequency shifts to either mechanism e.g. to distinguish between local frequency shifts from non local ones, although very careful experiments have been carried out *ex vivo* to look at changes in specific WM tract specimens [82]. It is also highly likely that both mechanisms coexist to modulate the observed frequency changes.

5.3.7 Contribution from other sources

In order to study the orientation dependence phenomenon, it is ideal to focus on the same tissue region and change the orientation of B_0 with respect to the tissue. Since B_0 is static in the scanner and the direction cannot be changed, it would be instinctive to change the orientation of the tissue instead. However, owing to the restricted space in the scanner, this is not practical especially when using small head coils. Instead, we looked at the R_2* and resonance frequency at various locations and correlated them with the corresponding orientation information from DTI.

We have shown using our simulations how the orientation of white matter fibers can modulate R_2* and resonance frequency. However, it can be seen that the presence of any other susceptibility sources that have an anisotropic arrangement can potentially contribute to this orientation dependence. Cylindrical blood vessels in the white matter have been reported to run primarily along the same direction as the fiber bundles [23]. Spherical iron-rich oligodendrocytes have been observed to be arranged in rows in an axis again along the long fiber axis [29, 87]. These parallel structures should modulate the signal in a similar trend as the simulated WM fibers. In our model, the contribution from blood vessels and oligendrocytes have been assimilated into the extra-axonal compartment. Considering their relatively low volume fraction, their contribution is not expected to be significant.

In this study, we linked orientation information from the brain using DTI to R_2* and resonance frequency measurements. The underlying assumption is that the sole difference between the different regions is the orientation of the WM fiber to B_0. However, it can be seen that different regions may express

differences other than orientation of WM fibers. Differences in local concentration of non-heme iron has been found to be the underlying cause for R_2* and resonance frequency differences in deep gray matter such as putamen and globus pallidus. However, it has been reported that iron concentration in the white matter is low [57]. A study by Li *et al.* [90] reported insignificant differences in total iron content (determined by chemical analysis) in WM regions with large R_2* differences. These indicate that iron does not play an important role in modulating the signal change in WM. The distribution of myelin in WM is however more variable. In the same study by Li *et al.* [90], difference between the T_2* in superior region of corona radiata and cingulum has been attributed to differences in amount of myelination observed via histological staining and electron microscopy.

5.4 Conclusion

The relationship between GRE signal behaviour and the orientation of WM fibers to B_0 has been investigated. We have not only seen how resonance frequency and R_2* vary with orientation but we have also observed higher order signal properties that change with orientation such as deviation of R_2* decay from mono-exponentiality and deviation of GRE phase from linear phase evolution (see Fig. 36 for a summary of results). Conventional GRE signal models are unable to account for several aspects of the experimentally observed GRE signal behaviours such as a deviation of relationship between resonance frequency and orientation to B_0 from a $sin^2\theta$ trend and the presence of higher order signal properties. On the other hand, such behaviours are predicted by the geometric WM model that explicitly models the different compartments of the WM microstructure.

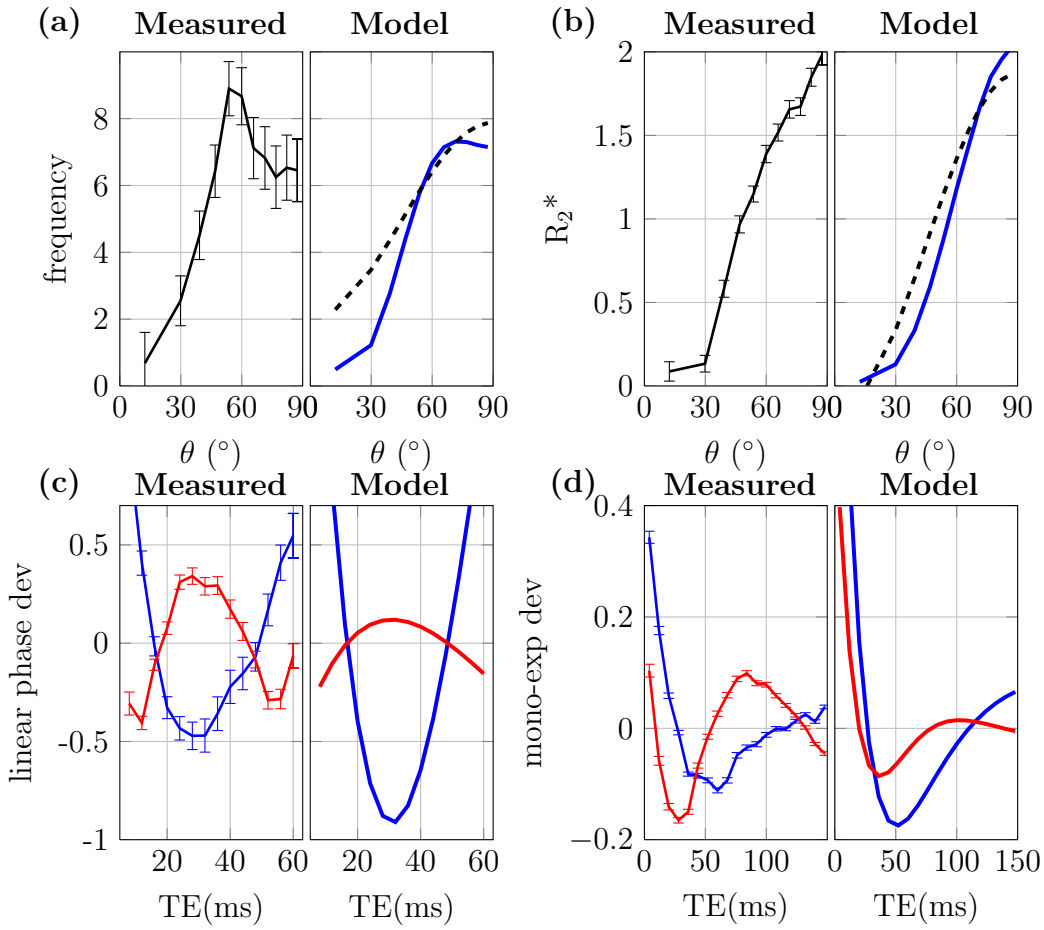

Figure 36: *Summary of frequency and R_2* modulation with orientation to $B_0(\theta)$. (a) Frequency modulation (b) R_2* modulation. Dashed line represents best fit $sin^2\theta$ dependence. (c) Deviation from linear phase evolution. (d) Deviation from monoexponential decay. Red and blue lines represent perpendicular and parallel fibers respectively. Error bars denote standard error.*

Importantly, this forward model uses parameter values based on literature rather than fitting the model to the experimental results. The success of this simple model in predicting a broad range of signal properties provides confidence that signal behaviour is, in fact, driven by the modelled microstructure. The power of this approach is in generating the entire frequency profile, rather than simply the low-order moments, leading to a much richer description of signal in the presence of microstructural changes.

6 Myelin effects

In this chapter, the effect of myelination on GRE signal behaviour is studied. A cuprizone model of demyelination, which involves feeding C57BL/6 mice a special diet containing the neuro-toxin cuprizone, was first used to induce different amount of demyelination in the mouse brain. After which we studied the relationship between *ex vivo* GRE contrast (R_2* and frequency) with the histologically determined amount of myelination in the corpus callosum (CC). Geometric modeling was performed to simulate hypothetical cases of myelin loss and compared with our *ex vivo* results. Furthermore, an *in vivo* longitudinal study was performed to track GRE signal changes in the CC over a 6 weeks period of cuprizone-induced demyelination followed by a subsequent 6 weeks of remyelination after termination of the cuprizone treatment.

6.1 Introduction

Cuprizone, also known as bis(cyclohexanone)oxaldihydrazone, is a copper chelator commonly used in spectrophotometry [123]. Introducing cuprizone into the diet of young adult mice causes copper deficiency, which upsets the energy metabolism in oligodendrocytes and results in specific damages to oligodendrocytes followed by extensive breakdown of the myelin sheaths [158]. This demyelination is characterized by an intact blood-brain barrier with a consequent lack of T cells thus negating confounding contributions from the immune system [8]. The time course for the demyelination is highly predictable and complete demyelination was reported at the end of 6 weeks of feeding [106]. In addition, the region of demyelination is highly localized to specific brain tracts (e.g. CC and superior cerebellar peduncles) [14, 96] while seemingly not affecting other brain tracts, thereby allowing easier assessment of specific regions of the brain. The removal of cuprizone from the diet induces spontaneous remyelination [15], allowing for the investigation of the remyelination process. Chronic demyelination [96] can also be induced by extending the feeding period to 12 weeks with limited remyelination occurring after stopping cuprizone feeding. These characteristics make the cuprizone model an excellent model to look at the demyelination and remyelination process.

Various studies have used animal models of myelin deficiency to show that myelin is a major contributor to GRE phase and T_2* contrast between gray and white matter. Baxan *et al.* [10] reported that mice scanned after 12 weeks of cuprizone diet showed significant reduction in gray-white matter contrast in GRE phase images. A similar cuprizone induced demyelination study by Lee *et al.* [83] reported that both GRE phase and T_2* contrast were reduced after 6 weeks of cuprizone diet. Liu *et al.* [92] and Lodygensky *et al.* [93]

compared the GRE phase of control and shiverer mice and showed significantly reduced gray-white matter contrast in the shiverer mice.

The aim of this study is to better understand the relationship between myelination and observed GRE signal characteristics. With the cuprizone model of demyelination, we can induce different amount of myelination in the mouse brain by varying the duration of the cuprizone diet that an animal undergoes [106]. We focus specifically at changes in the CC since this is one of the most studied region of the cuprizone mouse model [106]. We can then perform *ex vivo* scanning of these mouse brains and correlate the GRE signals with histological measures of myelination to get a more accurate relationship between myelination and GRE signals. Unlike the previously mentioned studies [10, 83, 92, 93] that used only two time points to look at the difference between totally myelin deficient brains with normal brains, our investigation on different degrees of myelination should provide additional insights into how the demyelination process affect the GRE signal.

To ellucidate the potential mechanisms that can modulate the GRE signals, we simulated hypothetical cases of the demyelination processes to investigate the effects of geometry and composition of the WM compartments on GRE signal. This is especially important since most of the studies on the effects of myelination on GRE signal have considered a general bulk loss of myelin from the white matter [83,92,93] and do not consider the actual morphological and biochemical changes of the myelin compartment.

Finally, we explored the use of resonance frequency and R_2* to monitor the process of demyelination and remyelination *in vivo* in a longitudinal study.

6.2 Materials and Methods

Ex vivo and *in vivo* studies were carried out on two separate sets of animals. The *ex vivo* study looks at quantifying different degrees of demyelination by feeding animals cuprizone for various durations (up to 6 weeks). The *in vivo* study looks at longitudinal changes over 6 weeks of demyelination due to cuprizone feeding and a subsequent 6 weeks of remyelination following the cessation of cuprizone feeding.

6.2.1 Animal preparation

Cuprizone diet Normal mice chow (Harlan Laboratories, Inc) was grounded into fine powder using an electric grinder. For every 100g of powdered mice chow, 0.2g of cuprizone powder (Sigma-Aldrich Co. LLC.) was added and mixed well to obtain a 0.2% (by weight) cuprizone diet. Fresh powdered diet was prepared every two days. In order to ensure that the powdered chow is not contaminated by animal waste, custom mice chow feeding structures constructed from polyvinyl chloride (PVC) sheets were used for feeding. The feeding structure (Fig. 37) consists of a feeding trough to hold the powdered chow and a cover sheet with a long slit which the mice can access the powdered chow only with their mouth.

Feeding schedule For the *ex vivo* study, 9 C57BL/6 mice (8-weeks old) were fed 0.2% cuprizone diet *ad libitum* for different periods of time ranging from 0 to 42 days to induce varying degree of demyelination in the mouse brain. Feeding starts at different time points such that the final time point for all mice coincided (See Fig. 38). The animals were monitored daily and

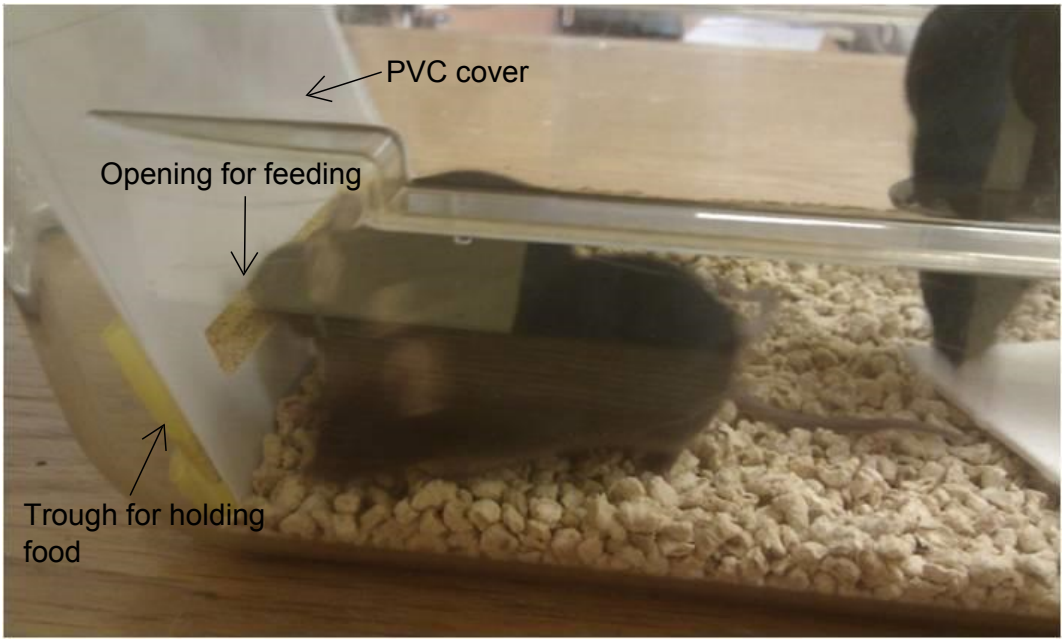

Figure 37: *Custom-made cuprizone diet feeder*

their weights were measured weekly to ensure their well being. For the *in vivo* study, 5 C57BL/6 mice (8-weeks old) were fed 0.2% cuprizone diet for a total of 6 weeks followed by a normal diet for another 6 weeks.

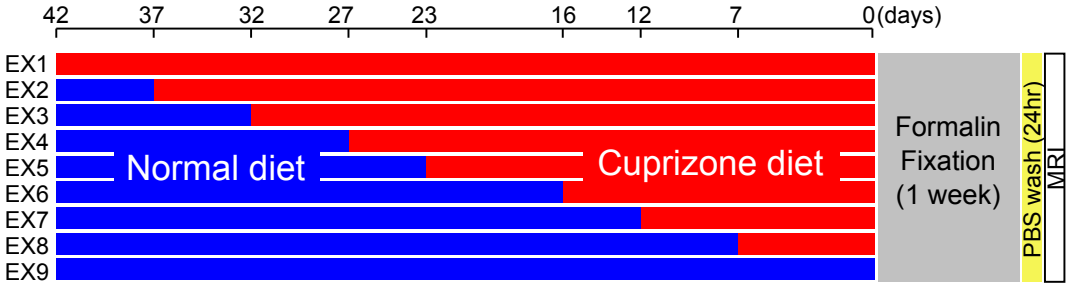

Figure 38: *Ex vivo experiment schedule. 9 mice were fed for various durations for a maximum of 42 days. Mice brain were then extracted and soaked in formalin for 1 week, followed by 24hr of PBS. Mice brain were then placed in FC40 fluorinated solution filled tube and scanned using MRI.*

Brain extraction and fixing For the *ex vivo* study, after the last day of feeding, all mice were perfused intracardially with saline solution followed by

10% neutral buffered formalin (NBF). The brains were then removed from the skull and stored in 10% NBF and fixated for 1 week. After 1 week, excess NBF was removed by washing with phosphate buffered saline (PBS) thrice and then soaked in PBS for 1 day. Next, the brain was placed in the mid point of a tube filled with fluorinated oil (FC40, 3M, Inc) and sealed. Care was taken to ensure that no air bubbles were trapped in the oil.

6.2.2 MRI

A 7T animal MRI scanner (Bruker Clinscan, Ettlingen Germany) was used in this study. A multiple echo GRE sequence was used to obtain 14 even echoes. Only signal at the even echoes were acquired while the duration of the odd echoes was minimized (by increasing the gradient strength) to reduce the inter-echo time. For each brain, 3 coronal slices were obtained at the following location with respect to Bregma: 0mm, 0.4mm and 0.8mm (Franklin and Paxinos, 2007). The acquisition parameters for the *ex vivo* scans were as follows : TEs = 3,7,11....55, ΔTE = 4ms, TR = 1500ms, flip angle = 70°, matrix size = 128 x 128, FOV = 10mm x10mm, slice thickness = 0.3mm, slice gap = 0.1mm and number of measurements = 10. The parameters for the *in vivo* scans are the same except for matrix size = 192 x 192 and FOV = 15mm x 15mm. Each scan takes about 1.5hr.

For the *in vivo* study, all animals were scanned once before the start of the cuprizone diet and then weekly for an additional 12 weeks. Animals were first anaesthetized using 3% isoflurane with oxygen and medical air and placed in a prone position on a standard mouse holder with the head of the animal tightly secured using a tooth bar and ear bars. Rectal temperature was maintained at 37°c using a hot air blower with feedback control. A 4 channel head coil

was used for signal reception while a body coil was used for excitation.

MR image processing GRE phase and magnitude images were reconstructed directly on the scanner. Each R_2* map was obtained by first taking the log of the 14 magnitude images (corresponding to the 14 echoes in ascending order of TE) and then performing a linear fitting on each individual voxel in these log magnitude images. The negative of the slope of the fitted line would give the R_2* value at each voxel. Each resonance frequency map was obtained by first performing a 1D phase unwrap followed by a linear fitting on individual voxels across the 14 GRE phase images. The slope of the fitted line will give the resonance frequency at each voxel.

6.2.3 Histology

Luxol fast blue myelin staining Luxol fast blue (LFB) myelin staining was used to obtain brain slice images that would indicate the relative amount of myelination present at the different brain locations. The brains were first embedded in paraffin and sectioned at Bregma 0mm, 0.4mm and 0.8mm (Franklin and Paxinos, 2007) and then stained with LFB using a standard staining protocol [74]. LFB reacts with the lipoproteins present in the myelin sheath to give a dark purple stain under a light microscope. All histology work was performed externally by the Advanced Molecular Pathology Laboratory, IMCB, A*STAR, Singapore.

Measuring myelination A common method of measuring the amount of myelination from LFB images is to assign scores to each image slice based on individual observations [51] (e.g. a score of 0 for total demyelination and 3 for

no demyelination). This method is subjective and only provides a limited range of values to describe the underlying myelination. We use normalized stain intensities to provide a more objective semi-quantitative measure of myelination.

Intensity normalization The raw LFB image in red-blue-green (RGB) format is first converted to gray-scale [110] such that the image intensity reflects the amount of myelination. A visual inspection on individual brain slice images revealed negligible intra-slice inhomogeneity. However, there was inconsistent brightness and contrast level across different slices of the same brain and also across different brains (Fig. 39), which is due to the staining procedure [99]. Each individual histology slice was normalized using a mean-standard deviation normalization algorithm [156,175]. Two GM ROIs were first drawn in the left and right cortical GM regions above the CC. Each image is individually normalized by subtracting the mean intensity of the GM ROIs and dividing by the standard deviation of the intensities within GM ROIs. This normalization scheme assumes that all cortical gray matter regions are not affected by the cuprizone diet and thus should stain equally for myelin. Although recent studies have reported subtle changes in the gray matter regions after cuprizone diet, it was reported that LFB staining does not have the sensitivity to detect such changes [142]. As such, the above assumption can be justified. The contrast of the myelinated region in the normalized image is reversed so that myelin appears brighter (Fig. 39).

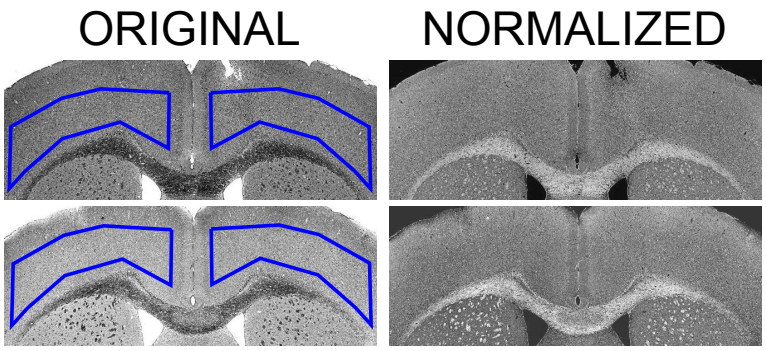

Figure 39: *Intensity normalization. The left column shows 2 original LFB slices from different mouse brains. The right column shows the same images after normalization. The blue polygons denote the GM ROIs used in the normalization.*

6.2.4 *Ex vivo* analysis

In the *ex vivo* study, we looked at the variation of the mean WM R_2* and resonance frequency from each MR image slice with the mean WM intensity in the corresponding normalized LFB image slice. For each pair of R_2* and resonance frequency maps in each slice, a ROI of the CC region was manually drawn on the R_2* image using the image processing software AMIDE [94]. The mean WM R_2* and resonance frequency in this ROI was calculated. A corresponding ROI was also manually drawn on the normalized LFB image to obtain a mean stain intensity. The mean R_2* and resonance frequency from each ROI in each slice were then correlated with the mean normalized LFB stain intensity.

In addition, we investigated the variations within a single image slice. A single brain slice that displayed partial demyelination was selected. Manual registration of the high resolution LFB image to the R_2* map was performed using the image processing software AMIDE [94]. The registered LFB image was then down sampled to the same resolution as the GRE images. We remove

pixels with partial WM volume from the down sampled LFB image and then looked at the voxel-wise correlation between the LFB stain with WM R_2* and resonance frequency (Fig. 43).

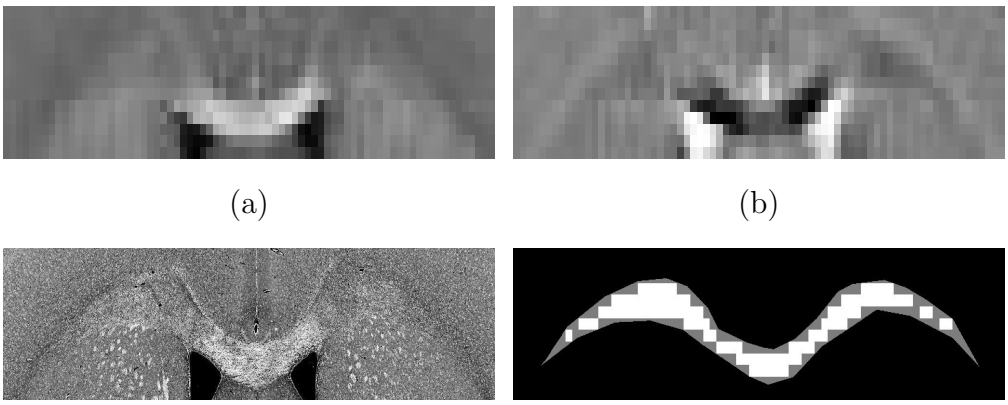

(a) (b)

(c) (d)

Figure 40: *Single slice GRE and LFB intensity images. (a)R_2* map (b)Frequency map (c) Normalized LFB image (d) shows the manually drawn white matter ROI where the gray outline is the ROI drawn on the higher resolution histology image and white area is the downsampled ROI with the removal of regions with possible partial volume. Partial myelination pattern is observed with lesser myelination at the sides of the CC compared with the middle region.*

6.2.5 *In vivo* analysis

In the *in vivo* study, we followed changes in the resonance frequency and R_2* in the CC of 5 mice during 6 weeks of demyelination followed by 6 weeks of remyelination. From the 3 image slices acquired during each scan, we selected a single R_2* image slice that best corresponds to the same location across all time points. Therefore, for each subject we will have a total of 13 image slices. Using the first image slice (corresponding to week 0) as the reference, the other image slices were registered manually onto the first image using AMIDE [94]. A WM skeleton ROI was drawn over the CC on the reference image and propagated to the other image slices. We then looked at changes

in the R_2* and resonance frequency values in the ROI across a total of 12 weeks. To quantify changes in R_2* and resonance frequency, we first perform a 1-way ANOVA test on the mean R_2* and frequency values from the five subjects over 13 time points (starting from week 0 to week 12) to test if there is significant deviation of the mean R_2* and frequency over time. If significant deviation ($p<0.05$) was detected by the ANOVA test, the Tukey's test was used to determine significant differences between time points. Statistical tests were performed using GraphPad Prism (GraphPad Software, Inc, CA, USA). Specifically, we were interested to see when does observations of demyelination and remyelination become statistically significant.

6.2.6 Demyelination simulations

Three different hypothetical scenarios of demyelination were simulated (Fig. 41) by making corresponding changes to the geometric WM model. For each scenario, myelin damage was assumed to start from the outside and progresses inwards, causing the thinning of the myelin sheaths and a progressive change in myelin volume fraction from 0.4 to 0 (total demyelination).

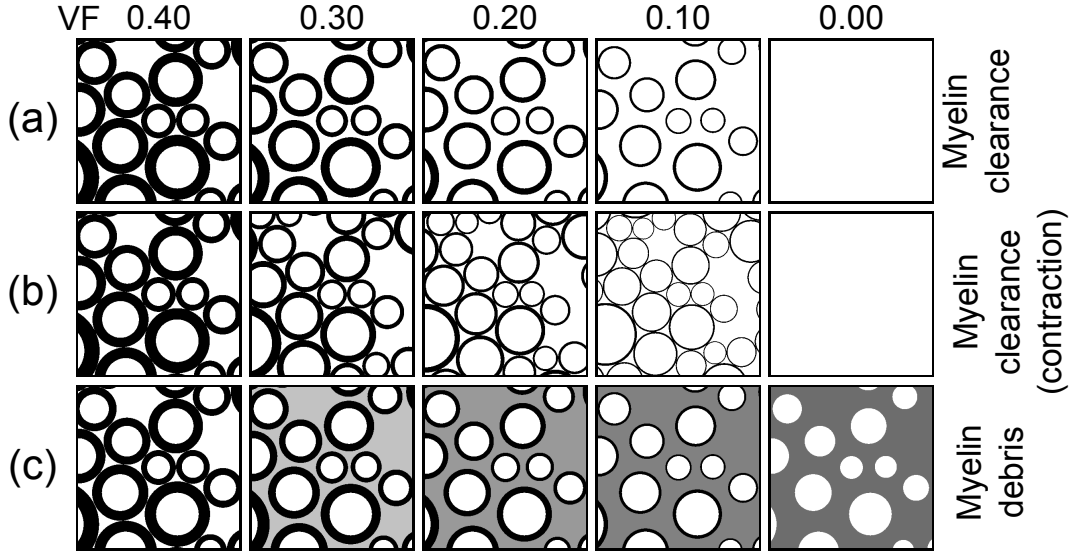

Figure 41: *Simulating demyelination changes. Rows (a) to (c) show 3 different scenarios of demyelination. Each column represents a specific volume fraction of myelin ranging from 0.4 to 0 (total demyelination) (a) shows thinning of myelin sheath without reduction in intra-axonal distance. (b) shows gradual thinning of myelin sheath accompanied by a reduction in the distance between axons. (c) shows a similar change as (a) but with an erosion of myelin materials into the extra-axonal space thereby changing the compartment's magnetic susceptibility.*

In the first scenario (Fig. 41a), as the myelin sheath gets thinner, the gaps left behind by the degenerating myelin is replaced by extra-axonal space and the removed myelin is assumed to be cleared rapidly from the extra-axonal space resulting in no change of chemical composition and hence magnetic suscepti-

bility of the extra-axonal compartment. We term this first scenario as myelin clearance.

In the second scenario (Fig. 41b), as the myelin sheath gets thinner, the axons becomes closer together to fill up the gap. The removed myelin is also assumed to be cleared rapidly from the extra-axonal space. This scenario is termed myelin clearance with contraction.

In the third scenario (Fig. 41c), geometric changes are the same as in the first scenario but the chemical composition of the extra axonal compartment is assumed to change due to the accumulation of myelin materials. The myelin debris is assumed to be evenly distributed in the extra-axonal compartmental leading to a uniform change in the magnetic susceptibility of the extra-axonal compartment but the mean magnetic susceptibility of the whole region is constant. This scenario is termed myelin debris.

The magnetic field perturbation maps are then simulated for each of the different scenarios and the GRE signal is calculated as discussed previously. For these simulations, the T_2 of the extra-axonal and axonal compartments were both reduced from 75ms to 50ms [122] to correspond the increase in field strength from 3T in the orientation dependence study to the 7T used in the myelination studies.

6.3 Results

6.3.1 Animal model

Histology LFB staining confirmed successful demyelination in the cuprizone fed mice as can be seen from the almost absence of contrast between the CC in the mice fed cuprizone for 6 weeks (Fig. 42a) as compared to the strong contrast present in the control mice (Fig. 42b).

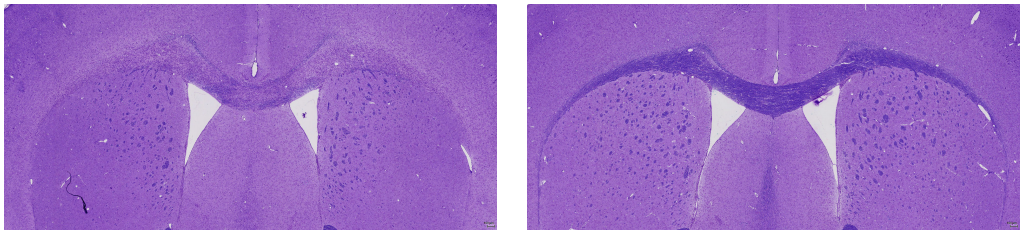

(a) (b)

Figure 42: *LFB results (raw images before normalization). Myelinated regions shows a dark purple staining. (Reversed contrast is shown in our normalized images) (a) shows extensive demyelination after 6 weeks of cuprizone diet while (b) shows normal myelination in a normal diet animal.*

Animal health Significant weight loss from 25.5±1.9 to 23.2±1.4 (paired t-test, $p < 0.005$) was observed immediately in the week following the introduction of the cuprizone diet. The mean weight loss of all animals at the end of the 6 weeks of feeding is about 14%. Despite the significant weight loss, animals were observed to be relatively normal. Animal survival rate was 100% and no significant immobility or handicap developed in the animals.

6.3.2 *Ex vivo* study

In the *ex vivo* study, significant changes can be seen in both frequency and R_2* images (Fig. 43). Similar changes can also be identified in the corresponding normalized LFB stain intensity. There is a general reduction in the gray-white matter contrast with increasing duration of cuprizone diet seen with in all three types of images.

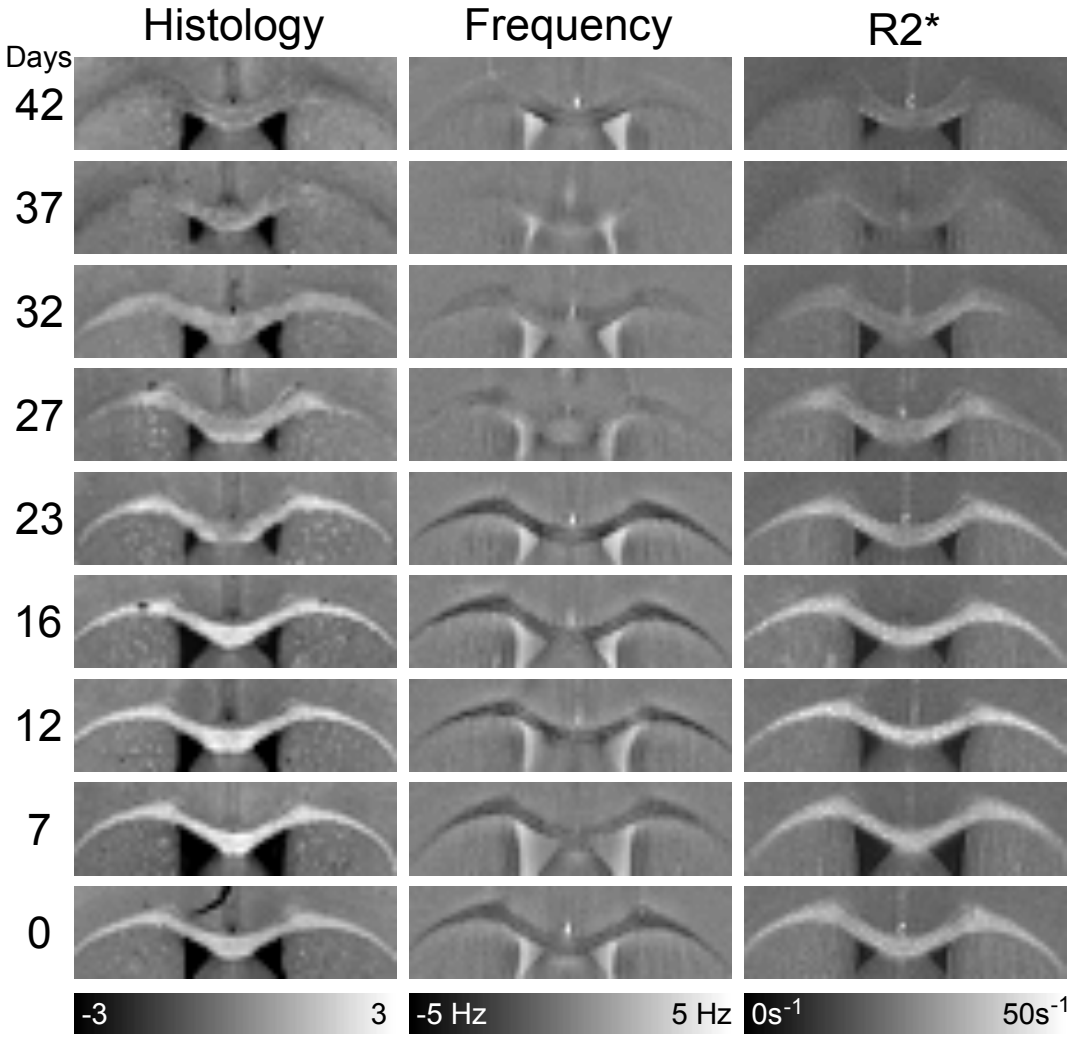

Figure 43: *Ex vivo study. Column 1 shows normalized histology images, column 2 and 3 show corresponding phase andR_2* images respectively. Each row corresponds to a different cuprizone diet duration.*

ROI analysis By correlating the mean ROI change across all image slices at all time points, a strong correlation (r = 0.930) was obtained between the R_2* and the normalized intensity from the LFB stained images (Fig. 44). Since the intensity of the LFB images is directly proportional to the underlying myelination, this can be construed as an increase inR_2* with an increase in myelination. From the scatter plot, the distribution of clusters of data points that have been color coded to represent similar durations of cuprizone treatment shows a general decrease in R_2* and normalized stain intensity as the duration of cuprizone diet increases.

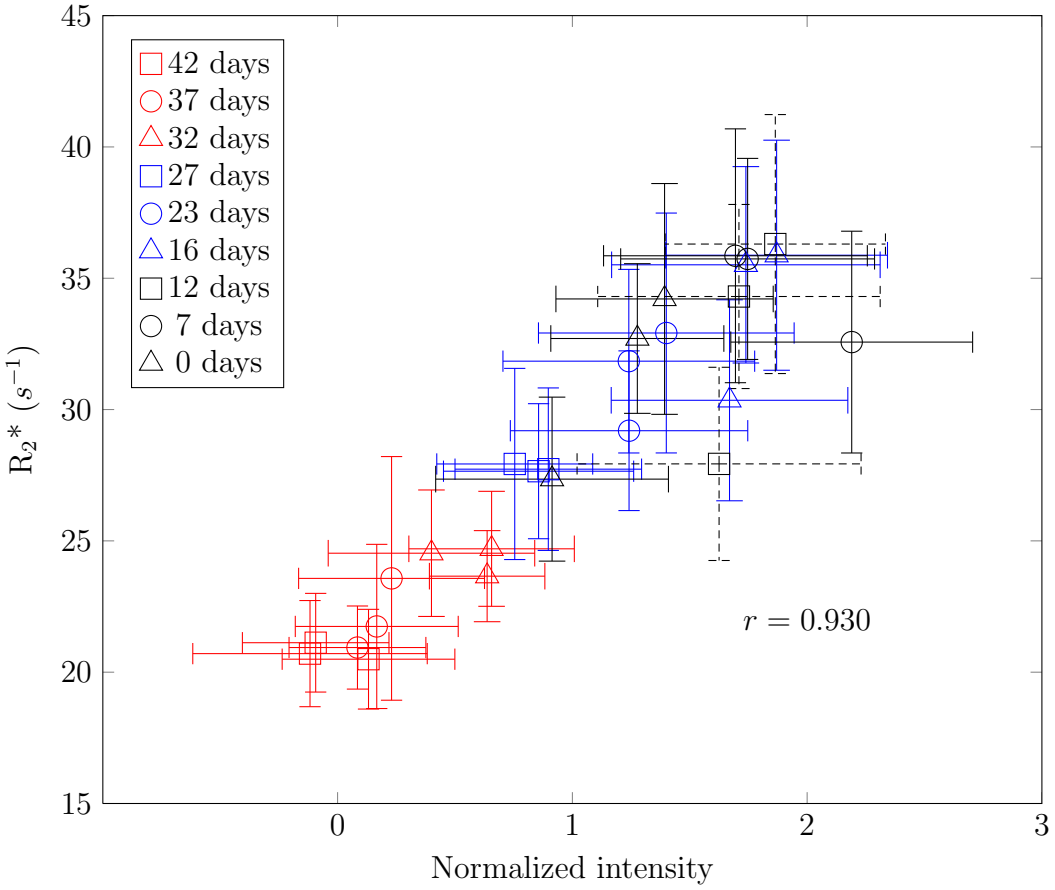

Figure 44: *Ex vivo correlation between ROI averaged R_2* and histology intensity. Error bars represent the standard deviation within each ROI.*

There is also a weaker correlation (r=-0.656) between the measured frequency

and normalized intensity (Fig. 45 b). The weaker correlation with frequency may be due to the non-local characteristics of phase images. The non-local characteristics may be amplified when looking across different subjects and slices, resulting in an even weaker correlation.

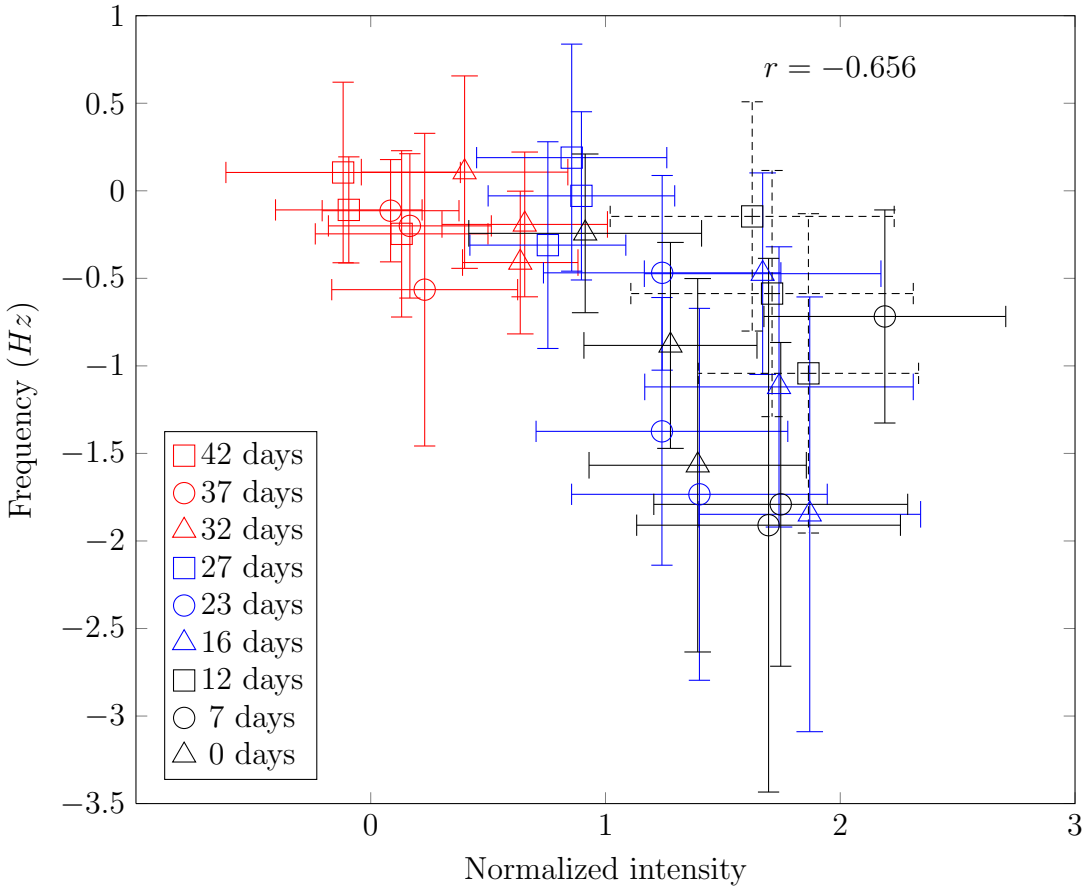

Figure 45: *Ex vivo correlation between ROI averaged frequency and histology intensity. Error bars represent the standard deviation within each ROI.*

The correlations presented here suggest that R_2* and resonance frequency are strongly affected by myelination but they do not necessarily imply the presence of a simple direct linear relationship between R_2* and frequency with myelination. We will show using our geometric model that the relationship is not as straight forward and can be affected by various factors such as volume fractions of compartments, packing patterns etc.

Voxel-wise analysis We have looked at the correlation between the ROI averaged resonance frequency and R_2* with normalized histology intensity across multiple subjects and brain slices. It is informative to look at deviations that can occur in each voxel within a single brain slice. It can be noted here that while error associated with LFB image normalization can affect the ROI analysis correlation results by increasing the dispersion of data points within the scatter plot, the voxel-wise study within the same slice is not affected by the normalization. In this voxel-wise analysis, a strong correlation (r = 0.862) was obtained between the R_2* and the normalized intensity from the LFB stained images (Fig. 46). It is surprising that the voxel-wise correlation coefficient of 0.862 is lower than the 0.930 obtained from the ROI analysis if we take into consideration the error involved with intensity normalization across multiple ROIs. A possible explanation for this discrepancy is the non linear relationship between R_2* change with myelination which will be discussed in more details later on.

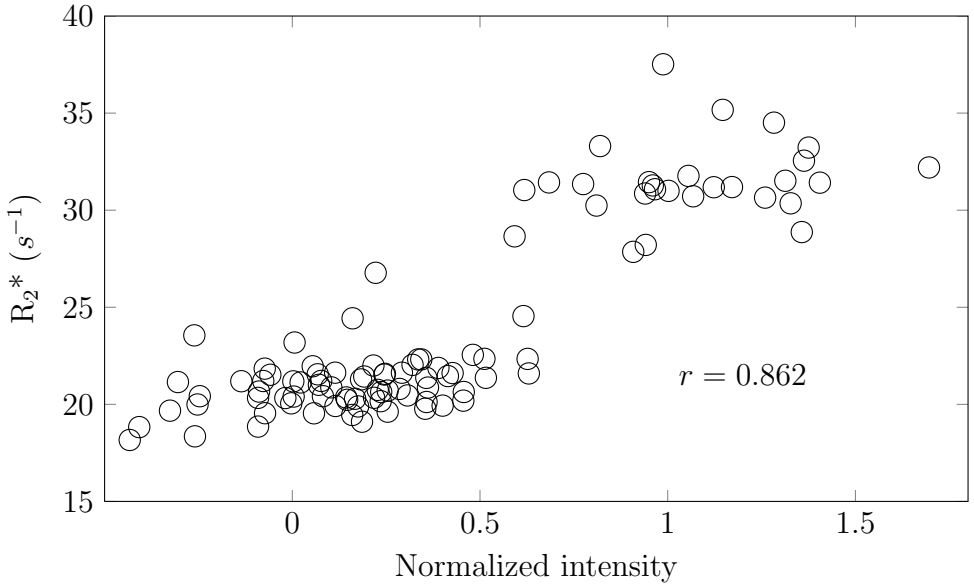

Figure 46: *Voxel-wise correlation between R_2* and normalized intensity in a single image slice.*

There is a strong correlation (r=-0.828) between the measured frequency and normalized intensity (Fig. 47). This correlation coefficient of -0.828 is stronger than the -0.656 reported in the ROI analysis. This can be mainly explained by the reduction in error involved with intensity normalization across multiple subjects and brain slices.

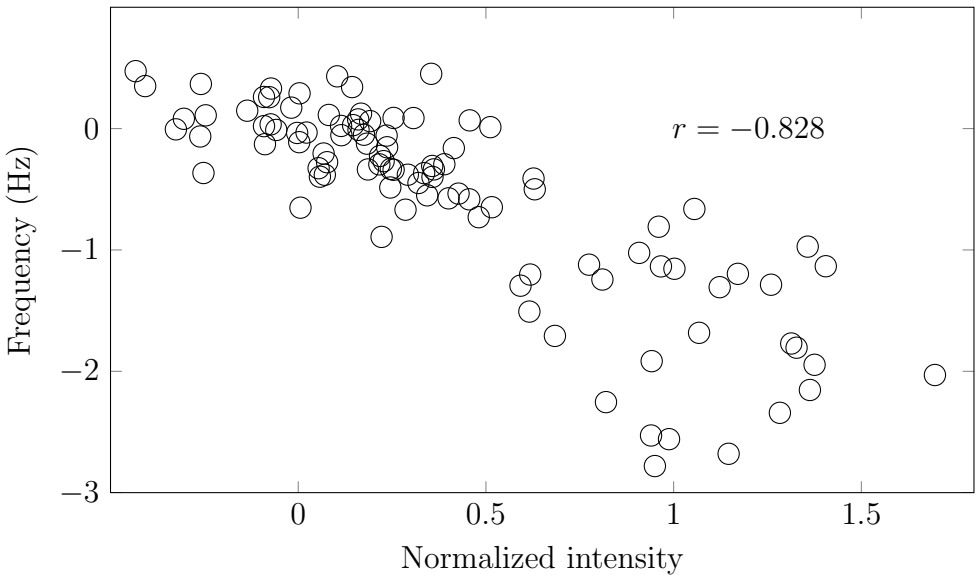

Figure 47: *Voxel-wise correlation between resonance frequency and normalized intensity in a single image slice.*

Deviation curves Deviation of the GRE magnitude decay from mono-exponentiality has been observed. Fig. 48 shows the deviation curves from 2 mice brains, one that has gone through 42 days of cuprizone diet and another that has not gone through any cuprizone diet. The residual from a mono-exponential fit on the decay curves of WM revealed negative trends in the deviation residuals. The deviation from mono-exponentiality is greater in the non-cuprizone diet mouse brain. Deviation from linear phase evolution has also been observed. The cuprizone diet mouse shows a positive quadratic trend while the normal diet mouse shows a negative quadratic trend.

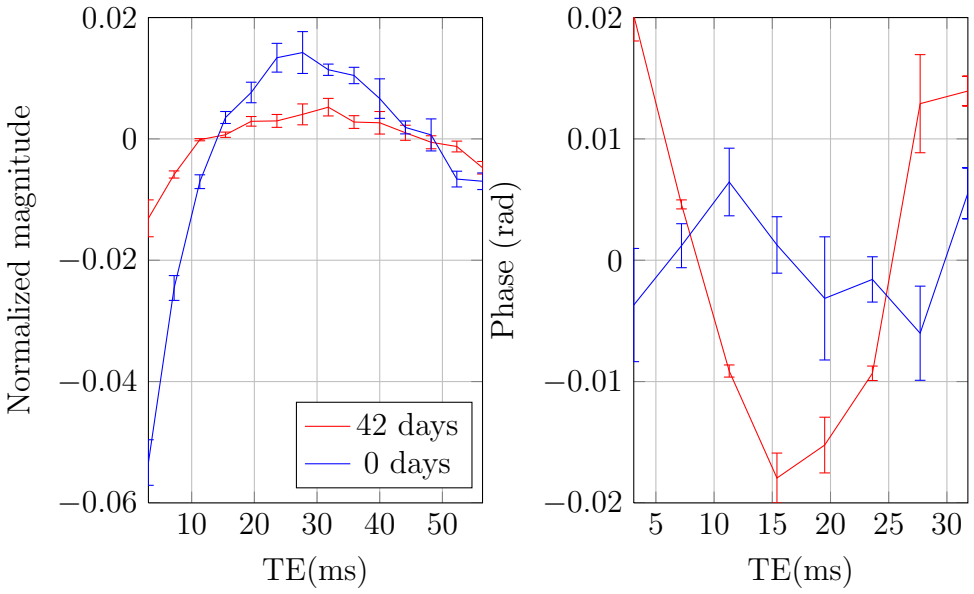

Figure 48: *Deviation from normal GRE signal characteristics. (a) shows deviation of GRE signal magnitude from mono-exponential decay. (b) shows deviation of resonance frequency from linear phase evolution. Blue line represents mice fed with normal diet while red line represents mice that has gone through 42 days of cuprizone diet. Error bars represent standard error.*

6.3.3 Simulation results

R_2* changes The simulation results show different trends of R_2* for the 3 scenarios (Fig. 49). For both scenarios of myelin clearance (i.e. with and without contraction) in which there was no change in the magnetic susceptibility of the extra-axonal compartment, there is a monotonic decrease in R_2* as the myelin volume fraction decreases. On the other hand, the myelin debris scenario shows an initial decrease in R_2* which then increases back to almost the same level before demyelination. The trends of the two myelin clearance scenarios do not follow the same path in the course of demyelination with the decay rate for myelin clearance without contraction (black line) being higher than that of myelin clearance with contraction (blue line) for the same myelin volume fraction.

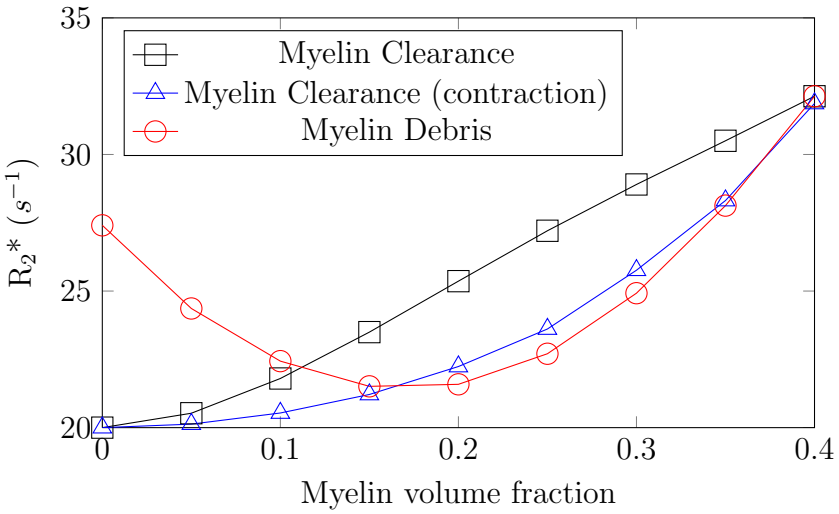

Figure 49: *Simulated change in R_2* with amount of myelination.*

To better understand the differences in R_2* despite the same myelin volume fraction, let us look at the frequency histograms for all scenarios when the myelin volume fraction corresponds to 0.25 (Fig. 50). An obvious difference between the frequency distributions of the myelin clearance scenarios (with-

out vs with contraction) is the volume fraction of the axonal and extra-axonal compartments. Myelin clearance without contraction has a larger extra-axonal space volume fraction and a corresponding smaller axonal volume fraction (keeping in mind that myelin volume fraction was kept constant) (Fig. 50a). The widths of frequency distributions within the axonal space are the same but the width of the frequency distribution in the extra-axonal space is larger in myelin clearance without contraction. Therefore, the higher extra-axonal volume fraction in myelin clearance without contraction which has a larger frequency spread results in the larger overall frequency spread leading to a faster decay rate. Myelin debris shows a very different frequency histogram with frequency shifts between the axonal and extra-axonal compartments (Fig. 50c).

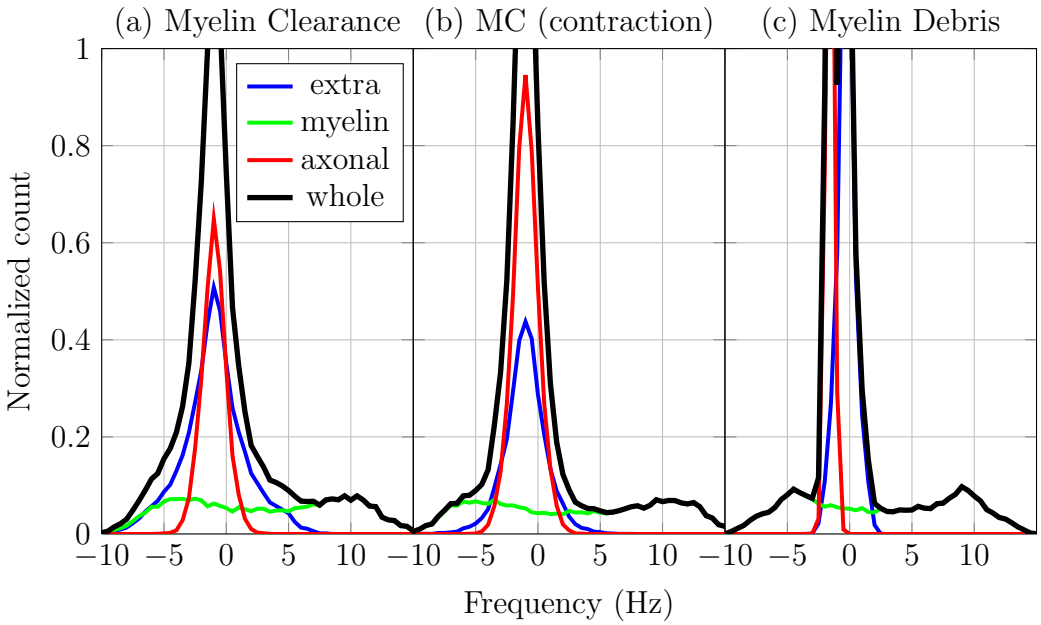

Figure 50: Simulated frequency histograms when myelin volume fraction is0.25. (a) Myelin clearance without contraction (b) Myelin clearance with contraction (c) Myelin debris

Comparing the R_2* changes in the single slice study with our simulation results. We found a close resemblance between the experimental data with our scenario

of myelin clearance with contraction. The two sets of data are displayed on the same figure in Fig. 51. The trend of the experimental R_2* seems to agree well with the non linear trend predicted by the simulation.

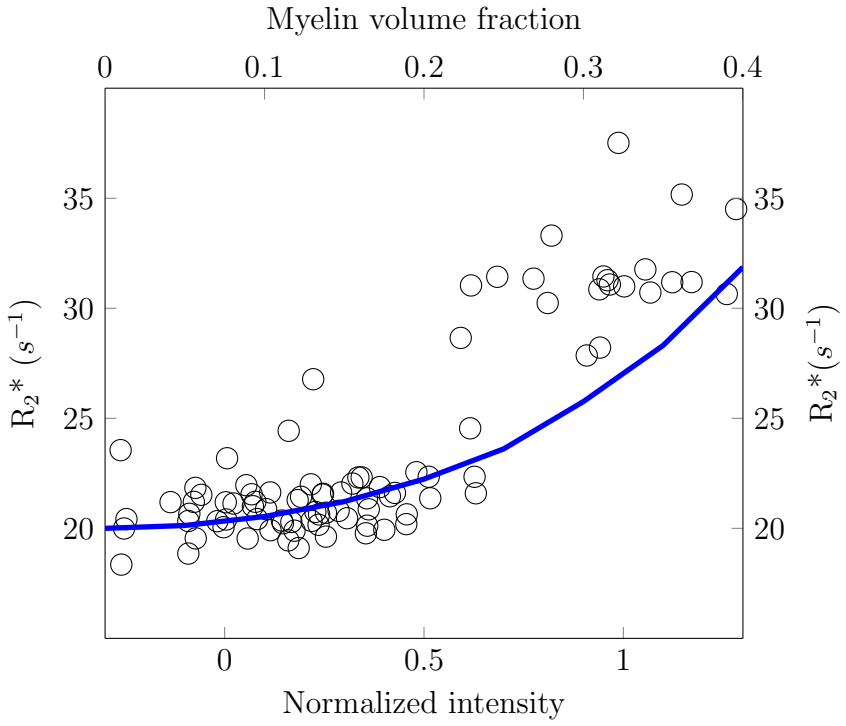

Figure 51: *Comparison between ex vivo R_2* measurements (single slice study) represented by the black circles with simulated R_2* from myelin clearance with contraction scenario represented by the blue line.*

The simulation predicts a slower change in R_2* with amount of myelination when the myelin volume fraction is relatively low and then a faster change in R_2* when the myelin volume fraction is higher. The data points from the voxel-wise analysis also appear to follow such a trend although a significant amount of data points are clustered at the lower myelin volume fraction. This non linear relationship between R_2* and myelination may also explain the reduced correlation of R_2* with normalized intensity in the voxel-wise analysis (r=0.862) as compared to the ROI analysis (r=0.930) in which averaging across ROIs and subjects may average out the effects of different underlying

demyelination mechanism (e.g. averaging out the curves in Fig. 49 to get a more linear relationship). It is noted here that Fig. 51 does not imply that we are performing a fitting of the simulation results to the experimental data, the main purpose was to show similarities between our simulation and experimental results.

We can also simulate the corresponding change in R_2 by weighing the R_2 of individual compartments by the change in their volume fractions during the demyelination process. The simulated change in R_2 due to a reduction in the myelin compartment is $3s^{-1}$. This value is comparable to $4s^{-1}$ reported by Aharoni *et al.* [3] in EAE mice at 9.4T and the $2.4s^{-1}$ reported by Zhang *et al.* [177] in cuprizone mice at 9.4T.

Resonance frequency changes The frequency response for the two cases of myelin clearance are very similar, showing an almost linear increase from negative frequency to 0 (Fig. 52b). The frequency response for myelin debris shows a monotonic increase but the trend is different from that of the two myelin clearance scenarios. From the gradient of the simulated frequency plots, it can be seen that myelin debris causes a larger initial change of resonance frequency when myelin volume fraction is reduced from 0.4 but the change decreases as the myelin volume fraction decreases.

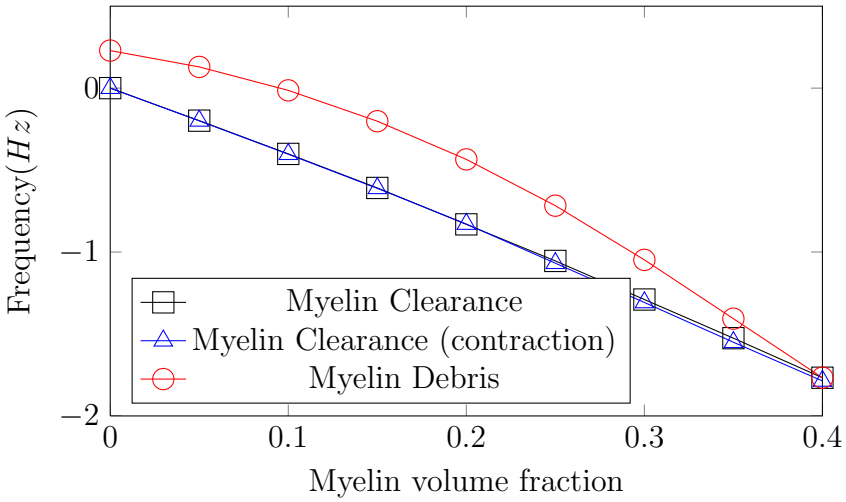

Figure 52: *Simulated change in resonance frequency vs amount of myelination.*

Myelin debris vs clearance may represent different stages of demyelination rather than a fundamental characteristic of demyelinating disease, in which the myelin enters the extra-axonal compartment as debris and is later removed by phagocytosis [28]. This would then imply that during disease progression, early demyelination would be marked by a large phase change, which would be reduced to a more linear resonance frequency change as myelin clearance begins. This difference could be useful, for example, in studying Wallerian degeneration, where myelin clearance is thought to be a key determinant of different time courses in peripheral and central nervous systems [147].

Similar to the comparison of R_2* modulation in the voxel-wise analysis with the simulated myelin clearance with contraction scenario, we can plot the experimental resonance frequency data together with the simulated frequency trend (Fig. 53) using the same mapping of myelin volume fraction to normalized intensity from Fig.51. Slight shifting (without scaling) of the frequency axis, which only shifts the baseline frequency but does not affect the range of signal change exhibited, was performed to obtain a better visual match. The

simulated frequency shows a roughly linear decrease in frequency over a similar range when myelination increases which is similar to the experimental data. However, from Fig. 53, we can see that the frequency trends for the other two scenarios also show a general increase over a similar range. It should be noted here that both Figs.51 and 53 do not imply any form of fitting but rather they show that the experimental and simulation results exhibit similar trends.

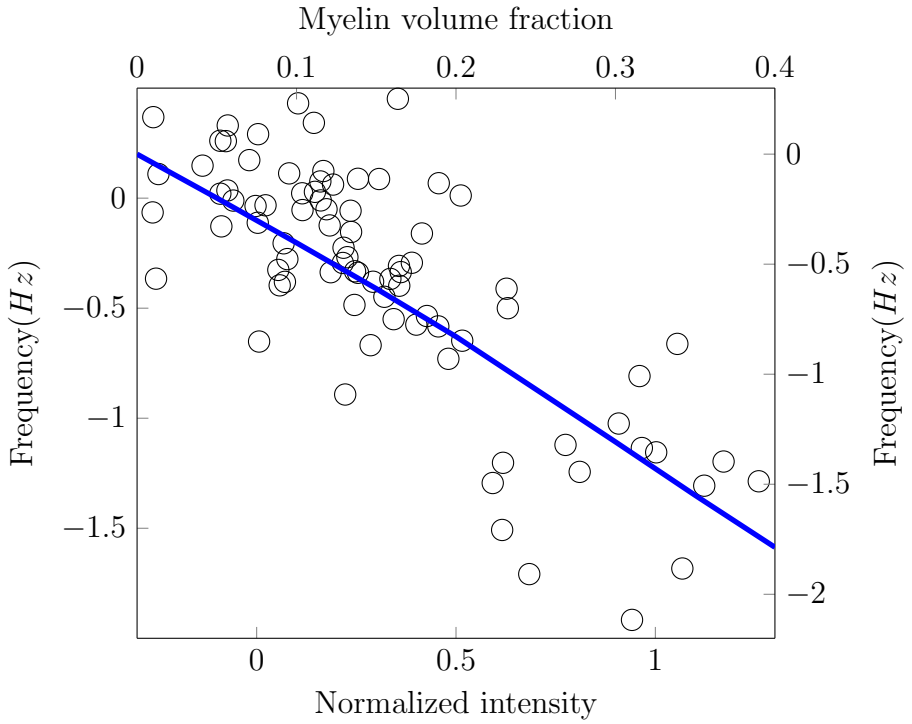

Figure 53: *Comparison between ex vivo resonance frequency measurements (single slice study) represented by the black circles with simulated resonance frequency from myelin clearance with contraction scenario represented by the blue line.*

Deviation curves Deviation curves from our simulations were similar to those obtained from the *ex vivo* studies. Fig. 54 shows deviation curves selected from the myelin clearance with contraction scenario. The deviation from mono-exponential magnitude decay shows very similar trends. The negative value of the simulated magnitude deviation curve agrees with the experimental

deviation curve. This interesting observation from our data shows that due to the presence of frequency shift, the decay curve does not necessary contain an observable fast decaying component on the decay curve (i.e. the decay over the first few echoes being faster than the decay over the later few echoes). Deviation from linear phase evolution shows that the more myelinated subject shows a more negative quadratic trend while the less myelinated subject shows a more positive quadratic trend. The difference between the more myelinated trend and the less myelinated trend from the simulation shows a range similar to the experimental results but the actual deviation curves are different. This difference may represent sources of nonlinear phase which were not accounted for.

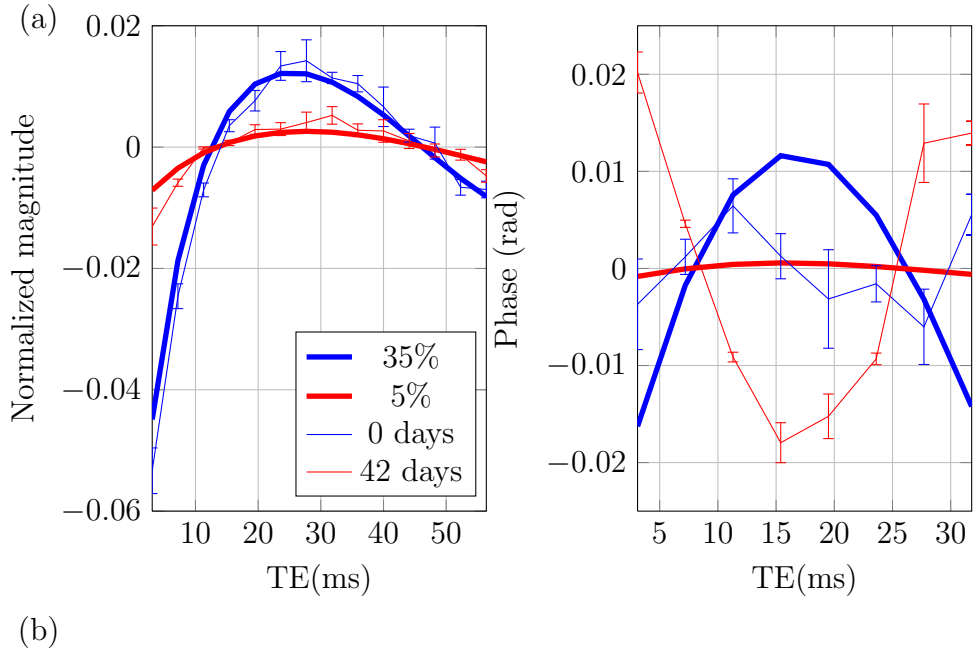

Figure 54: *Simulated deviation curves vs experimental deviation curves. (a) shows deviation of GRE signal magnitude from mono-exponential decay. (b) shows deviation of GRE phase from linear phase evolution. Thick red and blue lines represent 5% and 35% myelin volume fraction respectively. Thin red and blue lines represent 42 and 0 days of cuprizone diet from Fig. 48*

It is interesting to note here that the same set of parameters were used in the geometric model except for the reduced T_2 of the extra-axonal and axonal compartments. This forward model was able to predict a largely similar trend as observed in the experimental data at 7T which gives us confidence in the ability of the model to explain the effects of myelin on GRE signal characteristics.

6.3.4 *In vivo* study

We have established strong correlations between amount of myelination (determined by LFB stain intensity) with resonance frequency and R_2* *ex vivo*. Here, we look at the use of resonance frequency and R_2* in detecting longitudinal changes in myelination during the cuprizone induced demyelination and subsequent remyelination after stopping the cuprizone diet.

Visually, obvious reduction in the contrast of the CC can be seen in both R_2* (Fig. 55) and frequency maps (Fig. 56) of all individual subjects during the six weeks of cuprizone feeding. The contrast can then be seen to increase again after termination of the cuprizone diet. Enlarged ventricles can be seen in subject IN2. The *in vivo* images are observed to be of inferior quality compared to the *ex vivo* images, which is likely due to possible motion artifacts during respiration as well as the poor shimming of the mice brain *in vivo*.

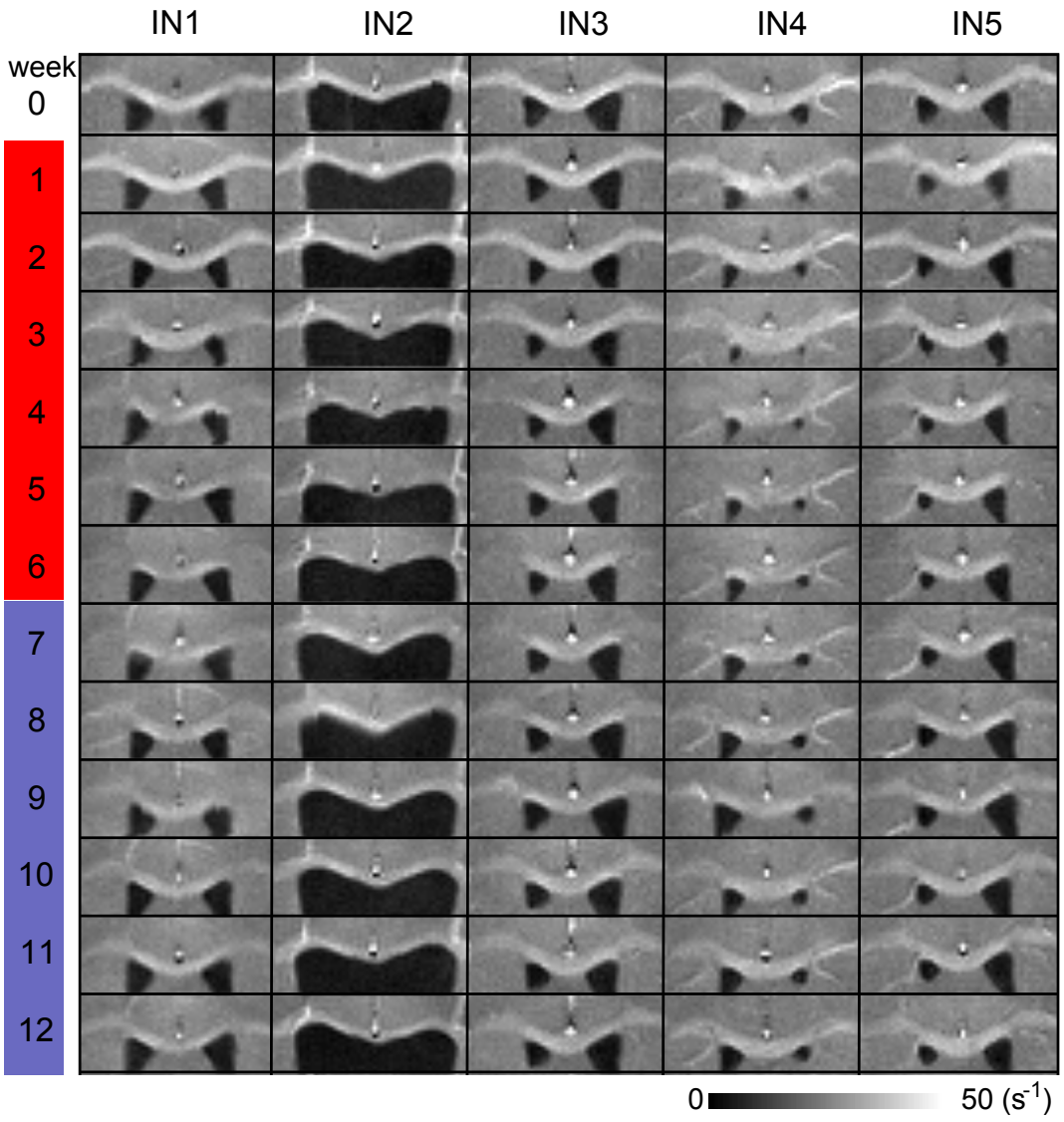

Figure 55: *R_2* change during demyelination and remyelination. Each row shows the R_2* map at each time point in weeks. Time point 0 corresponds to time before starting cuprizone diet, week 1 to 6 corresponds to duration of cuprizone diet, week 7 to 12 corresponds to period of normal chow. Each column corresponds to each of the 5 subjects.*

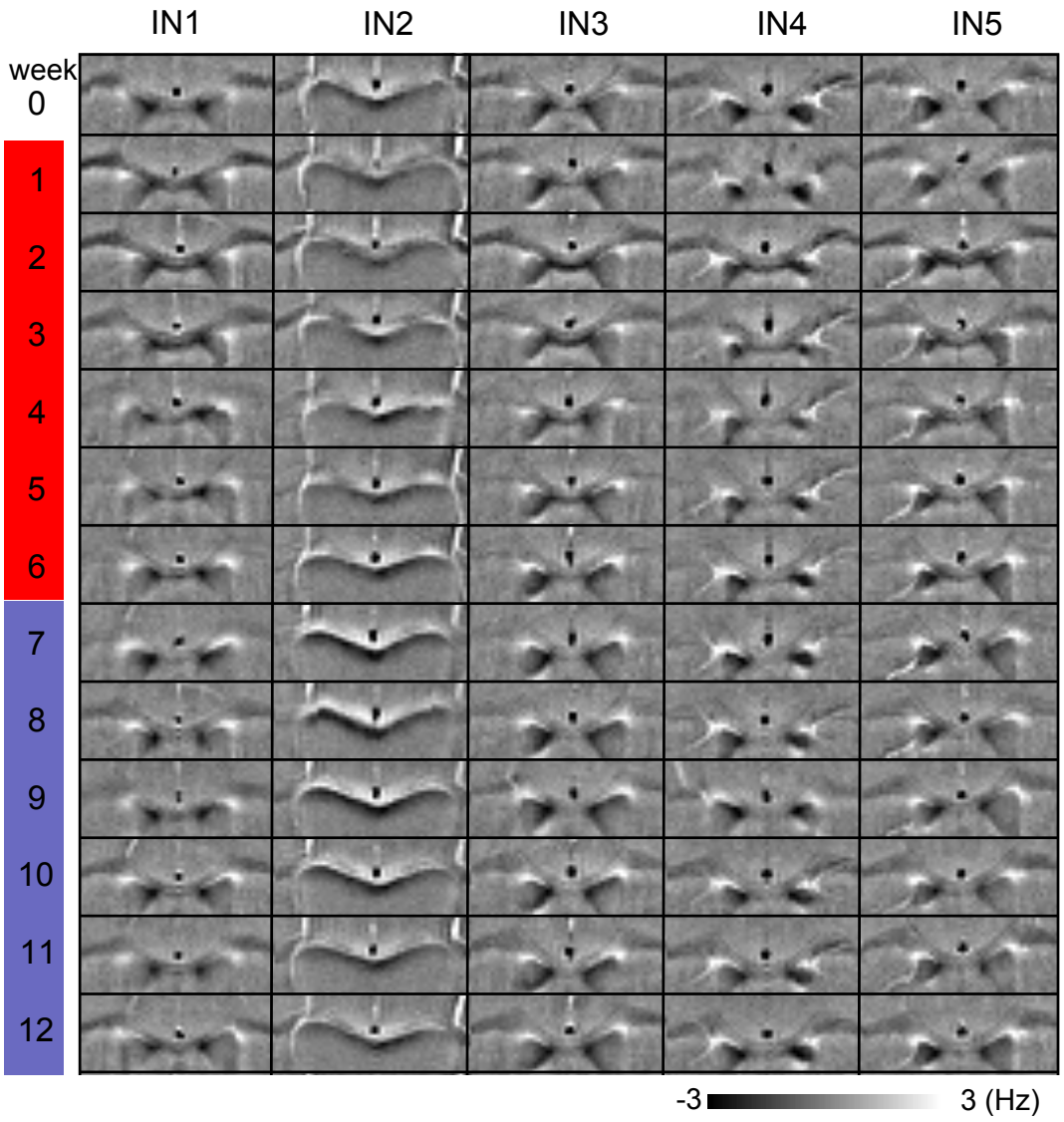

Figure 56: *Frequency change during demyelination and remyelination. Each row shows the frequency map at each time point in weeks. Time point 0 corresponds to time before starting cuprizone diet, week 1 to 6 corresponds to duration of cuprizone diet, week 7 to12 corresponds to period of normal chow. Each column corresponds to each of the 5 subjects.*

R_2* changes Looking at the subject averaged R_2* over the CC at different time points (Fig. 57), R_2* can be seen to decrease from $37s^{-1}$ before the start of the cuprizone diet (i.e. week 0) to a minimum of $28.5s^{-1}$ at the end of week 6 resulting in a total reduction in R_2* of $8.5s^{-1}$. Significant reduction of R_2* is first seen at week 3 ($p < 0.01$). This observation is similar to histological studies which also indicated seeing significant changes in myelination from week 3 of cuprizone feeding [106]. After stopping of the cuprizone diet at week 6, R_2* shows a general increase with significant increase in R_2* achieved 3 weeks after stopping the cuprizone diet (i.e. week 9). R_2* values 6 weeks after stopping cuprizone still shows significant differences as compared to week 0.

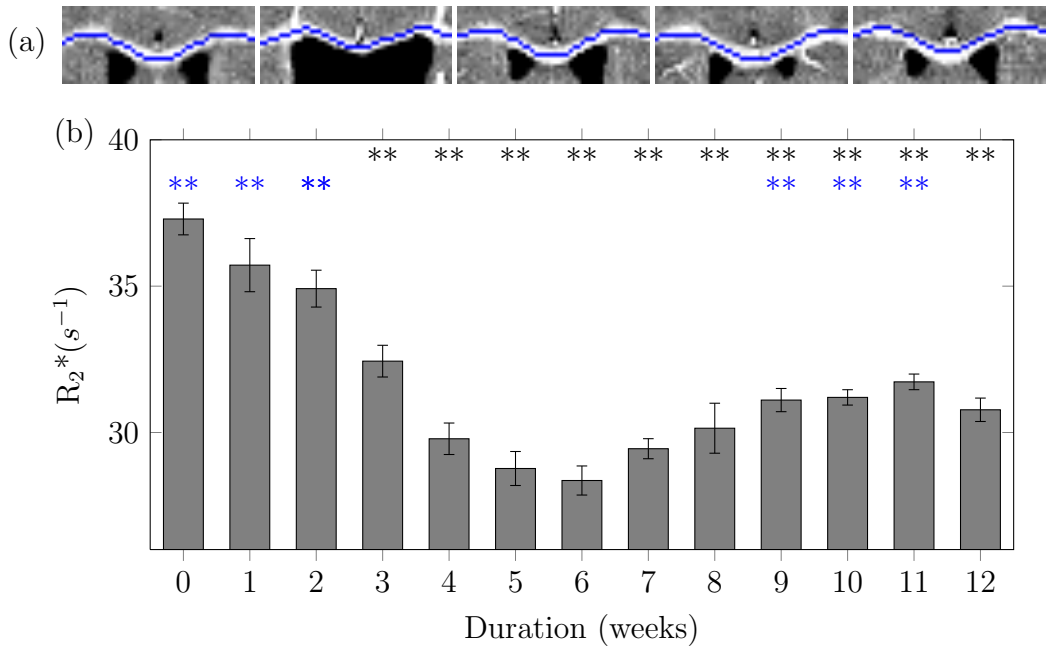

Figure 57: *In vivo changes to R_2* in CC (a) R_2* maps from each subject at week 0. Blue line represents the ROI drawn for the CC (b) shows the average change in R_2* over 12 weeks. Week 0 corresponds to time before starting cuprizone diet, week 1 to 6 corresponds to duration of cuprizone diet, week 7 to 12 corresponds to period of normal chow. Error bars denote the standard error across subjects. ** represents $p < 0.01$. Black represents comparison with week 0 and blue represents comparison with week 6.*

Since the relationship between normalized intensity with cuprizone feeding duration can be obtained from the *ex vivo* study, we can use the change in *in vivo* R_2* with cuprizone feeding duration to obtain a relationship between normalized intensity with myelination *in vivo*. Specifically, at each time point (i.e. from week 0 to week 6), we can plot the *in vivo* R_2* against the normalized intensity from the *exvivo* ROI study. A strong correlation (r=0.862,p<0.05) was obtained from the plot. This indicates that R_2* obtained *in vivo* is a strong indicator of the amount of underlying meylination.

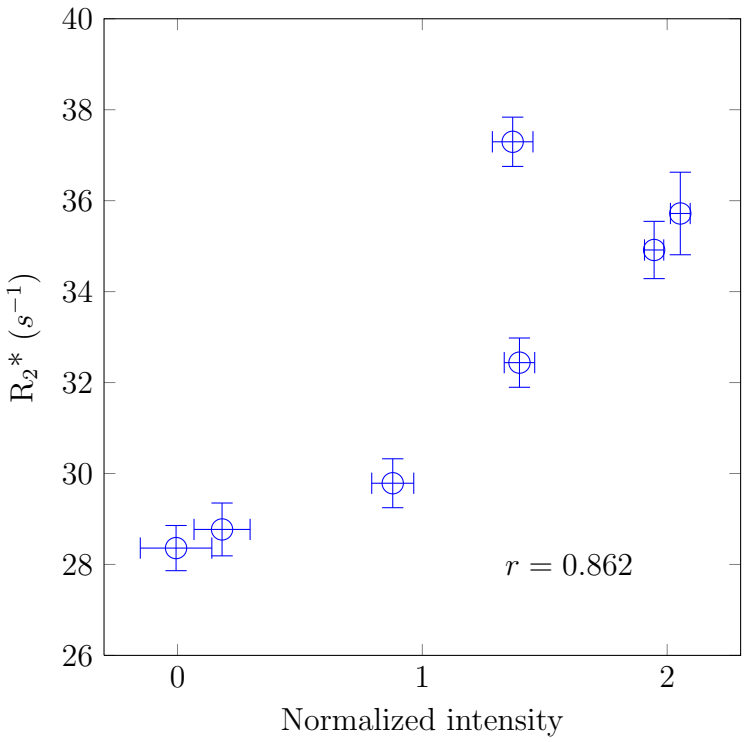

Figure 58: *Correlating in vivo R_2* with normalized LFB intensity from ex vivo data. Each data point corresponds to a single time point (from week 0 to 6) and the error bars indicate standard error.*

Frequency changes Using the same ROIs as the R_2* study, we can see a roughly similar trend as R_2* changes across the different time points (Fig. 60). However, large error bars at each time point can be seen and a one-way ANOVA test yielded no significant difference ($p > 0.05$) between the mean frequencies across all time points. This can be attributed to the presence of non-local artifacts that may be due to both the acquisition process and the phase processing. This is especially significant at the middle of the CC tract which is in close proximity to the ventricles thus rendering this region to be unsuitable for analysis.

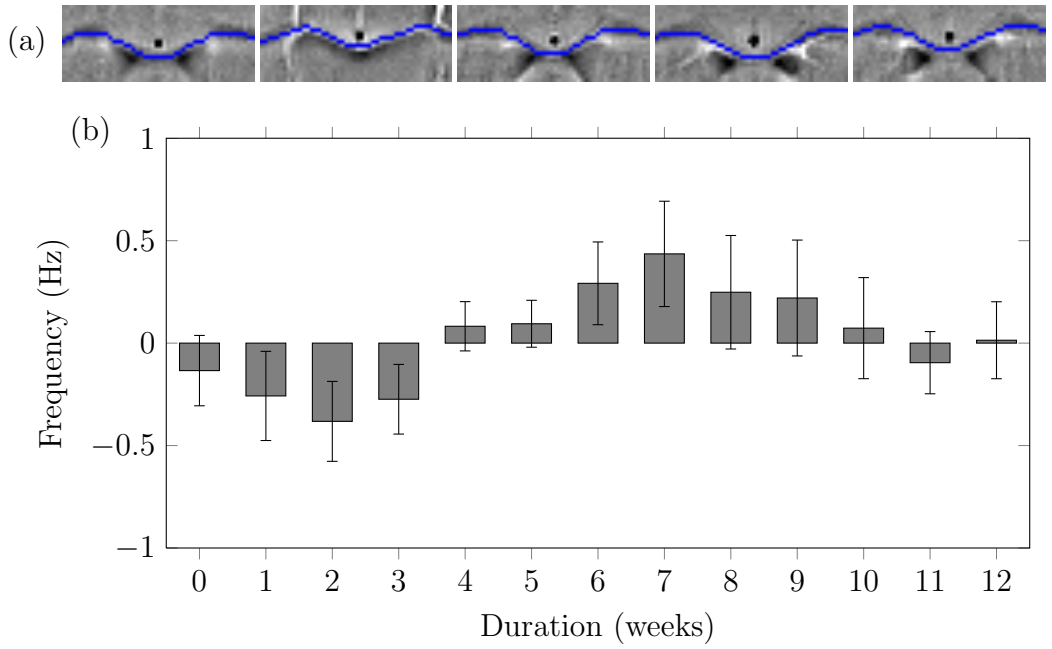

Figure 59: *In vivo changes to frequency in CC (a) Frequency maps from each subject at week 0. Blue line represents the ROI drawn for the CC (b) shows the average change in frequency over 16 weeks. Week 0 corresponds to time before starting cuprizone diet, week 1 to 6 corresponds to duration of cuprizone diet, week 7 to 12 corresponds to period of normal chow. Error bars denote the standard error across subjects. No significant difference was found with a one-way ANOVA test.*

However it can be seen from Fig. 56 that the more lateral portions of the CC seem to be less affected by non-local effects. Therefore, we removed the middle

portion from the original ROIs and repeated the same analysis. Frequency can be seen to increase from $-0.6Hz$ at week 0 to a maximum of $0.2Hz$ at the end of week 6 resulting in a total increase in frequency of $0.8Hz$ (Fig. 60). Significant difference ($p < 0.005$) between the mean frequencies across time points was observed from a one-way ANOVA test. In addition, a Tukey HFD test found significant difference ($p < 0.05$) between frequency at week 0 and week 6. In general, our resonance frequency data *in vivo* does not seem to be as robust as our R_2* data *in vivo*. More advanced post processing procedures [136] especially for removal of background phase contributions may help to improve our GRE phase data.

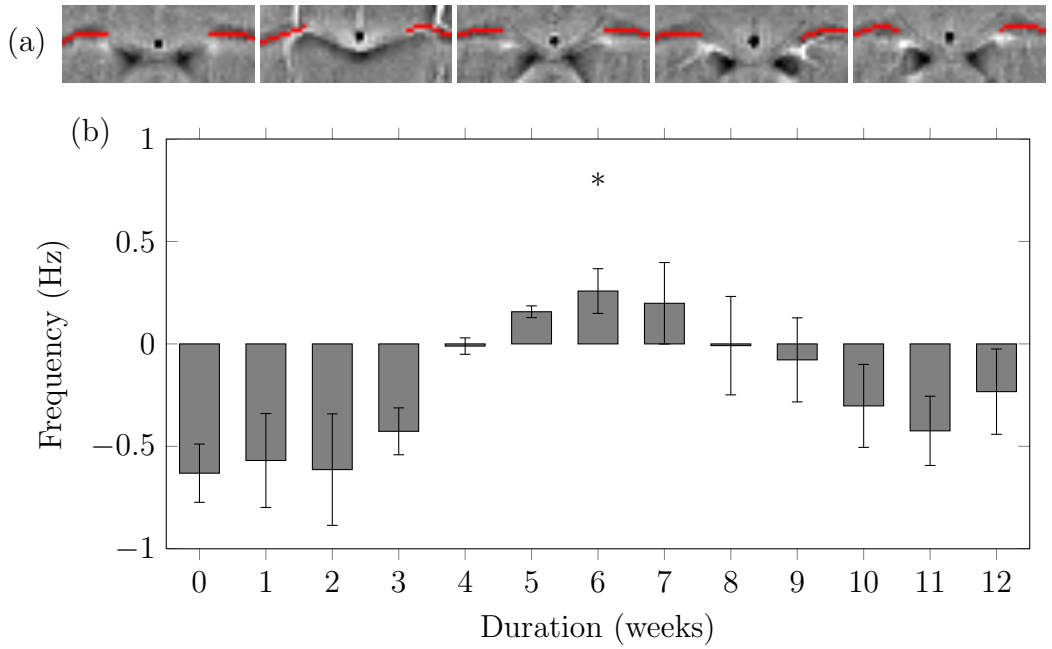

Figure 60: *In vivo changes to frequency in lateral CC (a) Frequency maps from each subject at week 0. Red line represents the ROI drawn for the CC (b) shows the average change in frequency over 16 weeks. Week 0 corresponds to time before starting cuprizone diet, week 1 to 6 corresponds to duration of cuprizone diet, week 7 to 12 corresponds to period of normal chow. Error bars denote the standard error across subjects.* $*$ *represents* $p < 0.05$. *Black represents comparison with week 0 and blue represents comparison with week 6.*

Other than the inferior SNR, the *in vivo* images also suffer from poor temporal

stability. Deviation curves (deviation of the GRE magnitude decay from mono-exponential and deviation of the GRE phase evolution from linearity) produced from *in vivo* images were inconsistent and are not shown or discussed here.

From the R_2* images, it is suggestive that complete remyelination was not achieved 6 weeks after stopping the cuprizone diet. This observation was supported by comparing the normalized intensity of LFB staining from one of the animals sacrificed after the last scan compared with a control animal ($p<0.001$ using a 2 sample t-test) (Fig. 61). Complete remyelination has been previously reported but those studies were looking not at the complete recovery of the original myelin volume fraction but rather the number of axons that have been remyelinated (without taking into consideration the amount of myelin volume fraction recovered) [106]. Mason *et al.* [105] has also reported incomplete remyelination (in terms of mean thickness of myelin sheath) at 6 weeks.

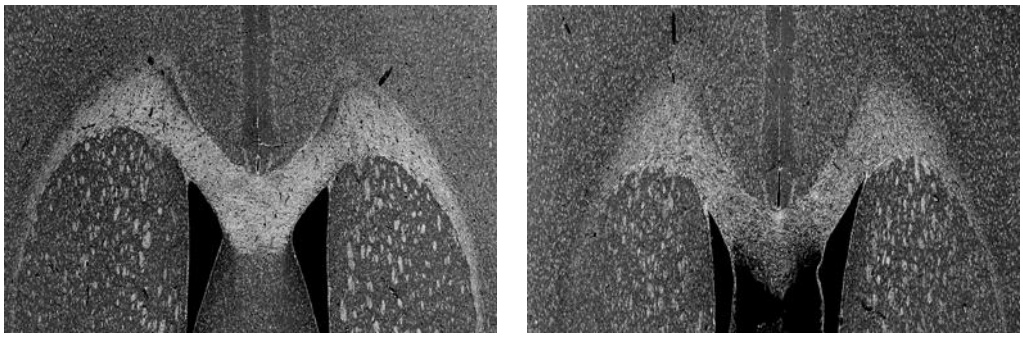

(a) (b)

Figure 61: Incomplete remyelination. Figure (a) shows the normalized LFB stain intensity of a normal control mice. (b) shows the normalized stain intensity of a mice 6 weeks after the stop of the cuprizone diet. The void in between the ventricles in (b) is caused by damage during histology.

6.4 Discussion

6.4.1 Myelin as major contributor to GRE contrast

The results shown so far reinforce the idea that myelin plays an important role in modulating GRE signal. By correlating different amounts of myelination with resonance frequency and R_2* measurements, the effects of myelin on resonance frequency and R_2* contrast was demonstrated. The resonance frequency contribution of myelin can be approximated to be 2.0Hz from the range of *ex vivo* study (Fig. 45). This 2.0Hz agrees well with other studies. Lodygensky *et al.* [93] reported an *in vivo* frequency difference of 0.8Hz and Liu *et al.* [92] reported an *ex vivo* frequency difference of 1.7Hz between Shiverer and control mice, and Lee [83] reported an *ex vivo* 3.0Hz frequency difference and *in vivo* 2.0Hz frequency difference between cuprizone-induced demyelinated mouse and a control mouse. A likely source of discrepancy with these studies is the post-processing procedure to remove the background field contribution.

From our study, an *ex vivo* R_2* change of approximately $15.0s^{-1}$ and *in vivo* R_2* change of approximately $8.5s^{-1}$ can be estimated from Fig. 44 and Fig. 55 respectively. The difference between the *ex vivo* and *in vivo* approximation of R_2* may be partly attributed to the difference in image quality, effects of tissue fixation, temperature etc. For changes in R_2* , Lee *et al.* [83] reported a value of approximately $9.0s^{-1}$ *ex vivo* and $10.0s^{-1}$ *in vivo*. The discrepancy between our results and the results from Lee *et al.* can be partly attributed to the processing of the R_2* maps from each subject. Lee *et al.* registered all the different subjects' images onto the same space and compared the subject averaged R_2* maps of control and cuprizone treated mice. This averaging

may have masked out variations between subjects and resulted in the smaller *ex vivo* R_2* change reported.

The use of both R_2* and resonance frequency data can better distinguish the origins of signal differences originating from WM. For example from our demyelination simulations, myelin clearance with and without contraction displays the same trend in frequency changes but different trend in R_2* changes. Unlike other multi-modality methods that generally require 2 separate scans, for example the use of both T_1 and T_2, a single GRE scan can be used to obtain both R_2* and resonance frequency data.

6.4.2 Morphological changes during demyelination

So far, most of the studies on the effects of myelination on GRE signal have considered a general bulk loss of myelin from the white matter ([83, 92, 93] and do not consider the actual morphological and biochemical changes of the myelin compartment. From our simulations of different scenarios of demyelination, we have also seen how spatial distribution and chemical composition of compartments can affect the frequency distribution and the corresponding GRE signal. Here, we discuss possible morphological changes during demyelination that can affect the micro-architecture.

In our demyelination simulations, myelin loss was simulated as the gradual thinning of the myelin sheath from the outside in. This is similar to the stripping of the myelin layers from the axon by microglias described by Blakemore *et al.* [13, 14] using ultrastructural studies. Several other mechanisms for myelin loss have also been observed by the same authors. Myelin sheaths have been observed to be vacuolated and subsequently phagocytized. Translocation

of the myelin to the side of the axon to leave behind a naked axon has also been observed. In other instances, surrounding myelin disintegrated into large disordered layers or into small vesicles. Direct invasion of the periaxonal space and the surrounding of the myelin by the phagocyte's cell body can also occur. It is likely that a combination of such myelin removal mechanisms exists.

After myelin loss, it has been observed that the demyelinated axon may be surrounded by enlarging astrocytic processes coupled by an increase in the number of microglial cells [63]. In addition, increase in the population of astrocytes has also been reported although this effect on the volume fraction of extra-axonal space is countered by the decrease in the oligodendrocyte population in the cuprizone-induced demyelination [97, 106]. This is similar to our simulation scenarios in which the inter-axonal distance does not decrease following myelin loss (e.g. first and last scenarios).

After the breakdown of the myelin sheath, the myelin lipids are digested by the microglial cells and transformed into neutral lipids [78]. Debris clearance by microglial cells not only tidies up the myelin debris but also encourages repair [113]. Delayed myelin debris clearance has been observed to delay remyelination in the CC of the cuprizone-induced demyelination mouse [141]. The effects of myelin clearance have also been demonstrated in our simulations in which we compared rapid clearance of myelin debris (first simulation) versus the non-clearance of the myelin debris (third simulation).

In our simulations, the axons are not affected by cuprizone (i.e. no change in the geometry and magnetic susceptibility of axons). Mason *et al.* [105] observed only rare instances of necrotic axons in the cuprizone-induced demyelination mouse while Stidworthy *et al.* [146] observed a small but significant population of axonal dystrophy using the same animal model. On the other hand,

axonal swelling has been reported by Song *et al.* [145]. Our model assumes no change in the axons but it can be noted that the effects of axonal changes (e.g. change in size of the axons) can be easily incorporated into our model. In our model, we have modeled the effects of contraction of the axonal spacing with each other which reflects the volume fraction of the extra-axonal water. A decrease in extracellular water associated with axonal swelling has previously been reported [148].

6.4.3 Other factors affecting GRE signal

So far, myelin has been discussed as the major contributor for the observed GRE signal changes. Other sources may yet play a role in modulating the GRE signal. Iron has been previously shown to be a major contributor in GRE signal modulation especially in the deep gray matter such as the globus pallidus and basal ganglia as well as for selected cortical regions [49]. The concentration of iron in these deep gray matter regions is significantly higher than that in white matter (e.g. 213.0 (μg Fe/ g tissue) in the globus pallidus [57] vs 15.0 (μg Fe/ g tissue) in the CC [153]). In contrast, iron concentrations in the cortex and the CC are reportedly very similar [57]. It has also been reported that the concentration is even lower in the CC of mice than in humans [137]. The study by Lodygensky *et al.* [93] has reaffirmed this point by showing that removing iron from the tissues does not affect the contrast between the CC and cortex much. Fukunaga *et al.* [49] also showed that iron extraction does not remove the contrast between gray and white matter thus implying that iron is not the main contributor to gray white matter contrast and that other factors must have contributed to this contrast.

The effects of chemical exchange has so far been neglected. It has been pre-

viously shown that chemical exchange occurring between water and macromolecules found on the myelin bilayers can result in positive frequency shifts [98,140]. The loss of the macromolecules during demyelination would decrease this positive frequency shift contribution i.e. contribute a negative frequency shift. This negative frequency shift due to the decrease in chemical exchange is opposite to the positive frequency shift due to a loss of diamagnetic myelin. If we were to consider chemical exchange in our model, this would imply that a larger susceptibility-induced frequency shift (e.g. a more negative value for the magnetic susceptibility of the myelin compartment) has to be introduced to offset the negative frequency shift.

It is well known that tissue fixation changes T_1, T_2 and diffusion which can be restored by soaking in PBS [138]. For our study, it is observed that the R_2* for fully myelinated WM in both *in vivo* and *ex vivo* scans is around $37s^{-1}$. This gives us the assurance that our preparation procedures (including the soaking of sample in PBS) are effective at mitigating the effects of fixation and restoring water content.

Our simulations have focused on susceptibility-related changes in the WM (e.g. changes in volume fractions and magnetic susceptibilities of compartments) that can bring about changes in the frequency distribution and hence affect GRE signal characteristics. However, it should be noted that the model is not restricted to only frequency distribution changes. Changes brought about in relaxation times e.g. T_2 and even diffusion coefficients can be incorporated into our model and these changes would also cause changes in the observed GRE signal behaviours even in the absence of differences in frequency distribution. In our simulations, it was assumed that water molecules are trapped between myelin sheaths and display negligible diffusion. It is intuitive to think that

this assumption may no longer hold during demyelination as the integrity of the myelin sheaths is compromised and the diffusion coefficient of myelin water may increase significantly.

6.5 Conclusion

We have successfully implemented the cuprizone mouse model of demyelination and used susceptibility based MR in the form of GRE resonance frequency and R_2^* to visualize these demyelination changes both *ex vivo* and *in vivo*. For the *ex vivo* images, excellent image quality was observed and the GRE derived indexes were found to correlate well with normalized LFB stain intensity. Simulated resonance frequency and R_2^* from hypothetical cases of demyelination have not only shown similar range of changes but also demonstrated how GRE signal changes can be affected by geometric and biochemical changes during the demyelination process. *In vivo* images, though of inferior quality, can detect longitudinal changes during periods of demyelination and subsequent remyelination.

7 Conclusion

7.1 Summary

Despite the increased interest in susceptibility based MR contrast in the WM, there is a gap in our knowledge about the source of this MR contrast in WM. Different groups have linked this contrast to the underlying tissue microstructure. Various methods have been used to explain the various signal characteristics (e.g. R_2* and resonance frequency), but most of these methods are designed to explain a single aspect of the signal. Moreover, the underlying assumptions used in these methods may not be applicable to WM e.g. the high volume fraction of magnetic susceptibility inclusions (myelin in our case).

We have introduced an explicit geometric model of white matter based on realistic estimates of parameters from literature. The aim was to bridge the link between actual white matter microstructure with susceptibility based MRI signal such as R_2* and resonance frequency. This method also has the advantage of being able to simulate the whole range of signal behaviour. In addition to resonance frequency and R_2*, simulation results suggested the presence of interesting deviations in WM GRE signal such as deviation from mono-exponential T_2* decay and deviation from linear phase evolution. We have also shown the importance of the spatial arrangement of perturbators in modulating the GRE signal. We validated the use of a geometric model in modeling field changes by studying the signal change in a polypropylene fiber phantom when the long fiber axis changes orientation to B_0. Other aspects of the model were also discussed such as the effects of diffusion and dependence of the accuracy of the model on the estimates of tissue parameters such as T_2 and susceptibility of compartments.

The dependence of WM GRE contrast on orientation to B_0 was investigated by combining fiber orientation information from DTI with GRE phase and magnitude data. Using the geometric WM model in a forward mode (i.e no fitting was performed and parameters were estimated from existing literature), we were able to observe similar trends in the change of GRE phase and R_2* with orientation. Importantly, these trends show deviation from the normal $sin^2\theta$ dependence that is predicted by the generic GRE signal models meant for lower volume fractions. Deviation of GRE signal from mono-exponential decay and linear phase evolution were observed in our experimental data and similar trends were also predicted by our geometric model. These temporal characteristics can be partly attributed to the multiple compartments present in the WM. Most signal models generally assume signal from only a single compartment and thus do not predict such characteristics.

The effects of myelination on GRE contrast was next studied. A toxin based mouse model of demyelination which involves the feeding of young mice with cuprizone was used. This model is able to produce well controlled amount of demyelination in the mouse brain that is dependent on the feeding duration and quantity of cuprizone. We induced different amount of demyelination by feeding the mice 0.2% cuprizone diet for different durations before sacrificing the animals for *ex vivo* scans and myelin staining. Our *ex vivo* study showed high correlation between GRE phase and magnitude to the intensity of myelin staining. An *in vivo* longitudinal study was also conducted to track myelination changes during cuprizone induced demyelination and subsequent remyelination after stopping cuprizone diet. The *in vivo* images were generally of poorer quality but clear trends of demyelination could be observed. An interesting observation was the incomplete remyelination that was seen from

our GRE data and was later verified by comparison of histology of a selected animal with a control. Hypothetical scenarios of changes in WM microstructure was then simulated using our geometric model. It was seen that the R_2* and GRE phase can be used to provide complementary information in characterizing microstructural changes.

7.2 Recommendations for future work

7.2.1 Model Fitting

So far, the geometric WM model has only been used in a forward mode using literature values to predict corresponding signal changes due to microstructural changes. The next progression of this work will be to fit the GRE signal derived from our geometric model to experimental data to obtain important parameters about the underlying WM microstructure. Such an approach has recently been adopted by various groups [131, 164]. However, fitting of the signal from the geometric model to the experimental data is expected to be computationally expensive due to the relatively large numbers of unknown parameters. This would require setting sensible range of values for the fitting. Some of the unknown parameters may also be estimated using other MR methods such as using dual echo spin echo sequences to obtain the T_2 estimates.

7.2.2 Geometric model

Currently, the myelin compartment has been modeled as a simple homogeneous hollow cylinder. It would be interesting to investigate the effects of a more detailed model of this compartment. For example, individual layers of myelin sheaths can be modeled as concentric hollow cylinders with multiple radii. The resultant magnetic field perturbation from such a distribution of susceptibility inclusions is expected to be significantly different than that generated by a single homogeneous hollow cylinder.

In our study, we have only looked at a simple case of magnetic susceptibil-

ity anisotropy in which we considered a cylindrically symmetric susceptibility tensor with principal axis along the long fiber axis. Recently, other groups have reported the use of more accurate representation of the susceptibility anisotropy by using a cylindrically symmetric tensor with radially oriented principle axis [131, 164]. The addition of this susceptibility anisotropy is expected to modulate but not drive the observed signal behaviour.

Exchange processes have so far been neglected in our GRE signal generation. It is known that exchange can cause phase shifts in WM and its effect on the overall GRE signal should be investigated.

The current 2D geometric model can be extended into a 3D model to allow a more accurate representation of the underlying WM microstructure. Non-parallel WM fibers and even crossing WM fibers can be simulated with such a 3D model. Contributions from iron-rich spherical oligodendrocytes may also be simulated. The 3D Fourier method may be used for the calculation of magnetic field perturbation associated with the 3D model [102, 131].

7.2.3 Phase image processing

In this work, basic methods such as mean filtering and 2D polynomial fitting have been used to remove background phase contribution to the phase images. More sophisticated methods such as the SHARP algorithm has been proposed to allow more accurate background phase removal [136]. Future work should investigate the effects of using these more sophisticated methods.

7.2.4 Orientation dependence

The orientation dependence study looked at different WM fiber tracts that may not only differ in their orientation to B_0 but also other forms of microstructure e.g myelination. It would be desirable to concentrate on the same WM fiber tract and change its orientation to B_0 . This is highly restrictive in human imaging due to the restricted space in the magnet but it is possible using small animals such as macaque or mice. This will allow us to better focus on the source of microstructural changes. Another option would be to use brain samples *in vivo* in which case it will be easier to remove any dependence on the bulk shape orientation to B_0 .

7.2.5 Demyelination

A semi-quantitative approach using myelin stain intensity was used to correlate with the GRE data. The intensity normalization scheme was based on a simple mean - standard deviation method, which assumes relative homogeneity of staining intensity within the same brain slice and also non-saturation of the stains. More sophisticated normalization scheme could be explored to obtain better intensity normalization. Alternatively, a quantitative measurement of the myelin content from each corresponding slice in each subject would provide a better link between the actual myelin content with the GRE data. Myelin can be isolated with a high degree of specificity from the brain and then its total volume can be measured to get the volume fraction of myelin present [115].

The *in vivo* GRE phase and magnitude images are inferior to the *ex vivo* images giving rise to poor quality R_2* and resonance frequency images. This is probably due to the presence of bulk magnetic field inhomogeneity and also the

presence of motion artefacts from the respiratory motion of the anaesthetized animal. Susceptibility artefacts leading to inhomogeneous signal drop offs can be reduced by the use of gel caps [2]. Respiratory motion is another cause of concern for poor image quality especially in the presence of a long TR. The purpose of the long TR was to ensure that the transverse magnetization has completely decayed. This long TR of 1.5s could essentially be reduced significantly due to the presence of gradient and RF spoiling. A shorter TR would then allow respiratory gating to be used to reduce motion artefacts.

In our study, we have focused on the cuprizone mouse model of demyelination that is excellent for looking at myelin changes in the WM . However, the cuprizone model is physiologically different from human demyelination diseases such as MS. For example, the myelin loss in the cuprizone model is secondary to damage to myelin-maintaining oligodendrocytes and there is also a lack of overall immune response (e.g. from the T cells) [106]. It would therefore be interesting to look at other models of demyelination which are physiologically closer to human demyelination diseases such as MS such as the experimental allergic encephalomyelitis model which can produce similar immune response involving T cells and production of antibodies [32] and the Theiler's murine encephalomyelitis model which uses virus to induce direct damage to the myelin sheaths [152].

This is a blank page.

References

[1] Aboitiz, F., Scheibel, A. B., Fisher, R. S., and Zaidel, E. Fiber composition of the human corpus callosum. *Brain Research 598*, 1-2 (1992), 143–53.

[2] Adamczak, J. M., Farr, T. D., Seehafer, J. U., Kalthoff, D., and Hoehn, M. High field BOLD response to forepaw stimulation in the mouse. *NeuroImage 51*, 2 (2010), 704–712.

[3] Aharoni, R., Sasson, E., Blumenfeld-Katzir, T., Eilam, R., Sela, M., Assaf, Y., and Arnon, R. Magnetic resonance imaging characterization of different experimental autoimmune encephalomyelitis models and the therapeutic effect of glatiramer acetate. *Experimental Neurology 240* (2013), 130–144.

[4] Albert, M., Antel, J., Brück, W., and Stadelmann, C. Extensive cortical remyelination in patients with chronic multiple sclerosis. *Brain Pathology 17*, 2 (2007), 129–138.

[5] Aloisi, F. Immune function of microglia. *Glia 36*, 2 (2001), 165–179.

[6] Andrews, T. J., Osborne, M. T., and Does, M. D. Diffusion of myelin water. *Magnetic Resonance in Medicine 56* (2006), 381–385.

[7] Arnold, D. L., Matthews, P. M., Francis, G., and Antel, J. Proton magnetic resonance spectroscopy of human brain in vivo in the evaluation of multiple sclerosis: assessment of the load of disease. *Magnetic Resonance in Medicine 14*, 1 (1990), 154–159.

[8] Bakker, D., and Ludwin, S. Blood-brain barrier permeability during cuprizone-induced demyelination: implications for the pathogenesis of

immune-mediated demyelinating diseases. *Journal of the Neurological Sciences 78*, 2 (1987), 125–137.

[9] Bakshi, R., Thompson, A., Rocca, M., Pelletier, D., Dousset, V., Barkhof, F., Inglese, M., Guttmann, C., Horsfield, M., and Filippi, M. MRI in multiple sclerosis: current status and future prospects. *The Lancet Neurology 7*, 7 (2008), 615–625.

[10] Baxan, N., Harsan, L., Dragonu, I., Merkle, A., Hennig, J., and von Elverfeldt, D. Myelin as a primary source of phase contrast demonstrated in vivo in the mouse brain. In *Proc., ISMRM, 19th Annual Meeting and Exhibition, Stockholm, Sweden* (2010), p. 3016.

[11] Bender, B., and Klose, U. The in vivo influence of white matter fiber orientation towards B(0) on T2* in the human brain. *NMR in Biomedicine 23*, 9 (2010), 1071–1076.

[12] Bernstein, M. A., King, K. F., and Zhou, X. J. *Handbook of MRI pulse sequences*. Access Online via Elsevier, 2004.

[13] Blakemore, W. Observations on oligodendrocyte degeneration, the resolution of status spongiosus and remyelination in cuprizone intoxication in mice. *Journal of Neurocytology 1*, 4 (1972), 413–426.

[14] Blakemore, W. Demyelination of the superior cerebellar peduncle in the mouse induced by cuprizone. *Journal of the Neurological Sciences 20*, 1 (1973), 63–72.

[15] Blakemore, W. Remyelination of the superior cerebellar peduncle in the mouse following demyelination induced by feeding cuprizone. *Journal of the Neurological Sciences 20*, 1 (1973), 73–83.

[16] Bloch, F. Nuclear induction. *Physical Review 70*, 7-8 (1946), 460–474.

[17] Boroske, E., and Helfrich, W. Magnetic anisotropy of egg lecithin membranes. *Biophysical Journal 24*, 3 (1978), 863–8.

[18] Boxerman, J. L., Hamberg, L. M., Rosen, B. R., and Weisskoff, R. M. Mr contrast due to intravascular magnetic susceptibility perturbations. *Magnetic Resonance in Medicine 34*, 4 (1995), 555–566.

[19] Branas, P., Jordan, R., Fry-Smith, A., Burls, A., and Hyde, C. Treatments for fatigue in multiple sclerosis: a rapid and systematic review. *Health Technology Assessment (Winchester, England) 4*, 27 (2000), 1.

[20] Buxton, R. B. *Introduction to functional magnetic resonance imaging: principles and techniques*. Cambridge University Press, 2009.

[21] Caldwell, J. H., Schaller, K. L., Lasher, R. S., Peles, E., and Levinson, S. R. Sodium channel Nav1. 6 is localized at nodes of Ranvier, dendrites, and synapses. *Proceedings of the National Academy of Sciences 97*, 10 (2000), 5616–5620.

[22] Case, T., Durney, C., Ailion, D., Cutillo, A., and Morris, A. H. A mathematical model of diamagnetic line broadening in lung tissue and similar heterogeneous systems: calculations and measurements. *Journal of Magnetic Resonance (1969) 73*, 2 (1987), 304–314.

[23] Cavaglia, M., Dombrowski, S. M., Drazba, J., Vasanji, A., Bokesch, P. M., and Janigro, D. Regional variation in brain capillary density and vascular response to ischemia. *Brain Research 910*, 1 (2001), 81–93.

[24] Chen, W. C., Foxley, S., and Miller, K. L. Detecting microstructural properties of white matter based on compartmentalization of magnetic susceptibility. *NeuroImage 70* (2013), 1–9.

[25] Cherubini, A., Péran, P., Hagberg, G. E., Varsi, A. E., Luccichenti, G., Caltagirone, C., Sabatini, U., and Spalletta, G. Characterization of white matter fiber bundles with T2* relaxometry and diffusion tensor imaging. *Magnetic resonance in medicine 61*, 5 (2009), 1066–1072.

[26] Clark, C. A., and Le Bihan, D. Water diffusion compartmentation and anisotropy at high b values in the human brain. *Magnetic Resonance in Medicine 44*, 6 (2000), 852–859.

[27] Collins, C., and Stephenson, K. A circle packing algorithm. *Computational Geometry 25*, 3 (2003), 233–256.

[28] Compston, A., and Coles, A. Multiple sclerosis. *The Lancet 372* (2008), 1502–1517.

[29] Connor, J. R., and Menzies, S. L. Relationship of iron to oligodendrocytes and myelination. *Glia 17*, 2 (1996), 83–93.

[30] Davies, G., Tozer, D., Cercignani, M., Ramani, A., Dalton, C., Thompson, A., Barker, G., Tofts, P., and Miller, D. Estimation of the macromolecular proton fraction and bound pool T2 in multiple sclerosis. *Multiple Sclerosis 10*, 6 (2004), 607–613.

[31] de Rochefort, L., Liu, T., Kressler, B., Liu, J., Spincemaille, P., Lebon, V., Wu, J., and Wang, Y. Quantitative susceptibility map reconstruction from MR phase data using bayesian regularization:

validation and application to brain imaging. *Magnetic Resonance in Medicine 63*, 1 (2010), 194–206.

[32] Denic, A., Johnson, A., Bieber, A., Warrington, A., Rodriguez, M., and Pirko, I. The relevance of animal models in multiple sclerosis research. *Pathophysiology 18*, 1 (2011), 21–29.

[33] Denk, C., Torres, E. H., MacKay, A., and Rauscher, A. The influence of white matter fibre orientation on mr signal phase and decay. *NMR in Biomedicine 24*, 3 (2011), 246–252.

[34] Dickinson, W. The time average magnetic field at the nucleus in nuclear magnetic resonance experiments. *Physical Review 81*, 5 (1951), 717–731.

[35] Du, Y. P., Chu, R., Hwang, D., Brown, M. S., Kleinschmidt-DeMasters, B. K., Singel, D., and Simon, J. H. Fast multislice mapping of the myelin water fraction using multicompartment analysis of T2* decay at 3T: a preliminary postmortem study. *Magnetic Resonance in Medicine 58*, 5 (2007), 865–870.

[36] Dutta, R., and Trapp, B. Mechanisms of neuronal dysfunction and degeneration in multiple sclerosis. *Progress in Neurobiology 93*, 1 (2011), 1–12.

[37] Duyn, J. MR susceptibility imaging. *Journal of Magnetic Resonance 229* (Apr 2012), 198–207.

[38] Duyn, J. H., van van Gelderen, P., Li, T.-Q., de Zwart, J. A., Koretsky, A. P., and Fukunaga, M. High-field MRI of brain cortical substructure based on signal phase. *Proceedings of the National Academy of Sciences 104*, 28 (2007), 11796–11801.

[39] Evans, D. A new type of magnetic balance. *Journal of Physics E: Scientific Instruments 7*, 4 (1974), 247.

[40] Feynman, R. P., Leighton, R. B., and Sands, M. *The Feynman lectures on physics, vol. 2: Mainly electromagnetism and matter.* Addison-Wesley, 1979.

[41] Fields, R. D. Myelination: an overlooked mechanism of synaptic plasticity? *The Neuroscientist 11*, 6 (2005), 528–531.

[42] Fields, R. D. *The other brain.* Simon and Schuster, Incorporated, 2010.

[43] Filippi, M., Absinta, M., and Rocca, M. Future MRI tools in multiple sclerosis. *Journal of the Neurological Sciences 331*, 1-2 (2013), 14–18.

[44] Filippi, M., and Grossman, R. I. MRI techniques to monitor MS evolution The present and the future. *Neurology 58*, 8 (2002), 1147–1153.

[45] Fisel, C. R., Ackerman, J. L., Buxton, R. B., Garrido, L., Belliveau, J. W., Rosen, B. R., and Brady, T. J. MR contrast due to microscopically heterogeneous magnetic susceptibility: numerical simulations and applications to cerebral physiology. *Magnetic Resonance in Medicine 17*, 2 (1991), 336–347.

[46] Fisniku, L., Brex, P., Altmann, D., Miszkiel, K., Benton, C., Lanyon, R., Thompson, A., and Miller, D. Disability and T2 MRI lesions: a 20-year follow-up of patients with relapse onset of multiple sclerosis. *Brain 131*, 3 (2008), 808–817.

[47] Ford, J. C., Wehrli, F. W., and Chung, H.-W. Magnetic field distribution in models of trabecular bone. *Magnetic Resonance in Medicine 30*, 3 (1993), 373–379.

[48] Fu, L., Matthews, P., De Stefano, N., Worsley, K., Narayanan, S., Francis, G., Antel, J., Wolfson, C., and Arnold, D. Imaging axonal damage of normal-appearing white matter in multiple sclerosis. *Brain 121*, 1 (1998), 103–113.

[49] Fukunaga, M., Li, T. Q., van Gelderen, P., de Zwart, J. A., Shmueli, K., Yao, B., Lee, J., Maric, D., Aronova, M. A., Zhang, G., Leapman, R. D., Schenck, J. F., Merkle, H., and Duyn, J. H. Layer-specific variation of iron content in cerebral cortex as a source of MRI contrast. *Proceedings of the National Academy of Sciences 107*, 8 (2010), 3834–3839.

[50] Gareau, P. J., Rutt, B. K., Karlik, S. J., and Mitchell, J. R. Magnetization transfer and multicomponent T2 relaxation measurements with histopathologic correlation in an experimental model of MS. *Journal of Magnetic Resonance Imaging 11*, 6 (2000), 586–595.

[51] Giuliani, F., Metz, L. M., Wilson, T., Fan, Y., Bar-Or, A., and Wee Yong, V. Additive effect of the combination of glatiramer acetate and minocycline in a model of MS. *Journal of Neuroimmunology 158*, 1 (2005), 213–221.

[52] Goldman, L., and Albus, J. S. Computation of impulse conduction in myelinated fibers; theoretical basis of the velocity-diameter relation. *Biophysical Journal 8*, 5 (1968), 596–607.

[53] Haacke, E. M., Ayaz, M., Khan, A., Manova, E. S., Krishnamurthy, B., Gollapalli, L., Ciulla, C., Kim, I., Petersen, F., and Kirsch, W. Establishing a baseline phase behavior in magnetic resonance imaging to determine normal vs. abnormal iron content in the brain. *Journal of Magnetic Resonance Imaging 26*, 2 (2007), 256–264.

[54] Haacke, E. M., Brown, R. W., Thompson, M. R., and Venkatesan, R. *Magnetic Resonance Imaging: Physical Principles and Sequence Design*. Wiley, 1999.

[55] Haacke, E. M., Cheng, Y. C., House, M. J., Liu, Q., Neelavalli, J., Ogg, R. J., Khan, A., Ayaz, M., Kirsch, W., and Obenaus, A. Imaging iron stores in the brain using magnetic resonance imaging. *Magnetic Resonance Imaging 23*, 1 (2005), 1–25.

[56] Hahn, E. L. Spin echoes. *Physical Review 80*, 4 (1950), 580–594.

[57] Hallgren, B., and Sourander, P. The effect of age on the non-haemin iron in the human brain. *Journal of Neurochemistry 3*, 1 (1958), 41–51.

[58] Hanson, L. G. Is quantum mechanics necessary for understanding magnetic resonance? *Concepts in Magnetic Resonance Part A 32*, 5 (2008), 329–340.

[59] Hartline, D., and Colman, D. Rapid conduction and the evolution of giant axons and myelinated fibers. *Current Biology 17*, 1 (2007), R29–R35.

[60] He, X., and Yablonskiy, D. A. Biophysical mechanisms of phase contrast in gradient echo MRI. *Proceedings of the National Academy of Sciences 106*, 32 (2009), 13558–13563.

[61] Henkelman, R., Stanisz, G., and Graham, S. Magnetization transfer in MRI: a review. *NMR in Biomedicine 14*, 2 (2001), 57–64.

[62] Henkelman, R., Stanisz, G., Kim, J., and Bronkskill, M. Anisotropy of NMR properties of tissues. *Magnetic Resonance in Medicine 32* (1994), 592–601.

[63] Hiremath, M., Saito, Y., Knapp, G., Ting, J.-Y., Suzuki, K., and Matsushima, G. Microglial/macrophage accumulation during cuprizone-induced demyelination in C57BL/6 mice. *Journal of Neuroimmunology 92*, 1 (1998), 38–49.

[64] Hodgkin, A. L., and Huxley, A. F. Currents carried by sodium and potassium ions through the membrane of the giant axon of loligo. *The Journal of Physiology 116*, 4 (1952), 449–472.

[65] Hodgkin, A. L., and Huxley, A. F. A quantitative description of membrane current and its application to conduction and excitation in nerve. *The Journal of Physiology 117*, 4 (1952), 500–544.

[66] Holland, B., Haas, D., Norman, D., Brant-Zawadzki, M., and Newton, T. MRI of normal brain maturation. *American Journal of Neuroradiology 7*, 2 (1986), 201–208.

[67] Horch, R. A., Gore, J. C., and Does, M. D. Origins of the ultrashort-T21H NMR signals in myelinated nerve: A direct measure of myelin content? *Magnetic Resonance in Medicine 66*, 1 (2011), 24–31.

[68] Hutton, C., Bork, A., Josephs, O., Deichmann, R., Ashburner, J., and Turner, R. Image distortion correction in fMRI: a quantitative evaluation. *NeuroImage 16*, 1 (2002), 217–240.

[69] Jackson, J. D., and Fox, R. F. Classical electrodynamics. *American Journal of Physics 67* (1999), 841.

[70] Jacobs, J., and Love, S. Qualitative and quantitative morphology of human sural nerve at different ages. *Brain 108*, 4 (1985), 897–924.

[71] Jenkinson, M., Beckmann, C. F., Behrens, T. E., Woolrich, M. W., and Smith, S. M. Fsl. *NeuroImage 62*, 2 (2012), 782–790.

[72] Kinney, H. C., Karthigasan, J., Borenshteyn, N. I., Flax, J. D., and Kirschner, D. A. Myelination in the developing human brain: biochemical correlates. *Neurochemical Research 19*, 8 (1994), 983–996.

[73] Kirschner, D. A., and Ganser, A. L. Compact myelin exists in the absence of basic protein in the shiverer mutant mouse. *Nature 283*, 5743 (1980), 207–210.

[74] KLÜVER, H., and Barrera, E. A method for the combined staining of cells and fibers in the nervous system. *Journal of Neuropathology and Experimental Neurology 12*, 4 (1953), 400–403.

[75] Koch, K. M., Papademetris, X., Rothman, D. L., and de Graaf, R. A. Rapid calculations of susceptibility-induced magnetostatic field perturbations for in vivo magnetic resonance. *Physics in Medicine and Biology 51*, 24 (2006), 6381.

[76] Lancaster, J. L., Andrews, T., Hardies, L. J., Dodd, S., and Fox, P. T. Three-pool model of white matter. *Journal of Magnetic Resonance Imaging 17*, 1 (2003), 1–10.

[77] Lassmann, H. Models of multiple sclerosis: new insights into pathophysiology and repair. *Current Opinion in Neurology 21*, 3 (2008), 242–247.

[78] Lassmann, H., and Wisniewski, H. Chronic relapsing experimental allergic encephalomyelitis: morphological sequence of myelin degradation. *Brain Research* (1979), 1–12.

[79] Laule, C., Vavasour, I. M., Moore, G. R. W., Oger, J., Li, D. K. B., Paty, D. W., and MacKay, A. Water content and myelin water fraction in multiple sclerosis. A T2 relaxation study. *Journal of Neurology 251*, 3 (2004), 284–293.

[80] Le Bihan, D., Mangin, J.-F., Poupon, C., Clark, C. A., Pappata, S., Molko, N., and Chabriat, H. Diffusion tensor imaging: concepts and applications. *Journal of Magnetic Resonance Imaging 13*, 4 (2001), 534–546.

[81] Lee, J., Hirano, Y., Fukunaga, M., Silva, A. C., and Duyn, J. H. On the contribution of deoxy-hemoglobin to MRI gray-white matter phase contrast at high field. *NeuroImage 49*, 1 (2010), 193–198.

[82] Lee, J., Shmueli, K., Fukunaga, M., van van Gelderen, P., Merkle, H., Silva, A. C., and Duyn, J. H. Sensitivity of MRI resonance frequency to the orientation of brain tissue microstructure. *Proceedings of the National Academy of Sciences 107*, 11 (2010), 5130–5135.

[83] Lee, J., Shmueli, K., Kang, B.-T., Yao, B., Fukunaga, M., van Gelderen, P., Palumbo, S., Bosetti, F., Silva, A. C., and

Duyn, J. H. The contribution of myelin to magnetic susceptibility-weighted contrasts in high-field mri of the brain. *NeuroImage 59*, 4 (2012), 3967–3975.

[84] Lee, J., van van Gelderen, P., Kuo, L.-W., Merkle, H., Silva, A. C., and Duyn, J. H. T(2)*-based fiber orientation mapping. *NeuroImage 57*, 1 (2011), 225–234.

[85] Lehre, K. P., and Rusakov, D. A. Asymmetry of glia near central synapses favors presynaptically directed glutamate escape. *Biophysical Journal 83*, 1 (2002), 125–134.

[86] Levesque, I. R., Giacomini, P. S., Narayanan, S., Ribeiro, L. T., Sled, J. G., Arnold, D. L., and Pike, G. B. Quantitative magnetization transfer and myelin water imaging of the evolution of acute multiple sclerosis lesions. *Magnetic Resonance in Medicine 63*, 3 (2010), 633–640.

[87] LeVine, S., and Macklin, W. Iron-enriched oligodendrocytes: A reexamination of their spatial distribution. *Journal of Neuroscience Research 26*, 4 (1990), 508–512.

[88] Li, T., Talagala, S., Koretsky, A., and Duyn, J. Contrast similarity between FA and T2* studied in white matter of the human brain at 3.0 and 7.0 T. In *Proc. Intl. Soc. Mag. Reson. Med* (2007), vol. 15, p. 1544.

[89] Li, T.-Q., van van Gelderen, P., Merkle, H., Talagala, L., Koretsky, A. P., and Duyn, J. H. Extensive heterogeneity in white matter intensity in high-resolution T2*-weighted MRI of the human brain at 7.0 T. *NeuroImage 32*, 3 (2006), 1032–1040.

[90] Li, T.-Q., Yao, B., van Gelderen, P., Merkle, H., Dodd, S., Talagala, L., Koretsky, A. P., and Duyn, J. Characterization of T2* heterogeneity in human brain white matter. *Magnetic Resonance in Medicine 62*, 6 (2009), 1652–1657.

[91] Liu, C. Susceptibility tensor imaging. *Magnetic Resonance in Medicine 63*, 6 (2010), 1471–1477.

[92] Liu, C., Li, W., Johnson, G. A., and Wu, B. High-field (9.4T) MRI of brain dysmyelination by quantitative mapping of magnetic susceptibility. *NeuroImage 56*, 3 (2011), 930–938.

[93] Lodygensky, G., Marques, J., Maddage, R., Perroud, E., Sizonenko, S., Hüppi, P., and Gruetter, R. In vivo assessment of myelination by phase imaging at high magnetic field. *NeuroImage 59*, 3 (2012), 1979–1987.

[94] Loening, A. M., and Gambhir, S. S. AMIDE: a free software tool for multimodality medical image analysis. *Molecular Imaging 2*, 3 (2003), 131–137.

[95] Lorentz, H. A. *The Theory of Electrons: And Its Applications to the Phenomena of Light and Radiant Heat*, vol. 29. BG Teubner, 1916.

[96] Ludwin, S. Chronic demyelination inhibits remyelination in the central nervous system. An analysis of contributing factors. *Laboratory Investigation: a journal of technical methods and pathology 43*, 4 (1980), 382–387.

[97] Ludwin, S. K. An autoradiographic study of cellular proliferation in remyelination of the central nervous system. *The American Journal of Pathology 95*, 3 (1979), 683–696.

[98] Luo, J., He, X., dAvignon, D. A., Ackerman, J. J., and Yablonskiy, D. A. Protein-induced water1H MR frequency shifts: Contributions from magnetic susceptibility and exchange effects. *Journal of Magnetic Resonance 202*, 1 (2010), 102–108.

[99] Macenko, M., Niethammer, M., Marron, J., Borland, D., Woosley, J. T., Guan, X., Schmitt, C., and Thomas, N. E. A method for normalizing histology slides for quantitative analysis. In *IEEE International Symposium on Biomedical Imaging: From Nano to Macro, 2009. ISBI'09.* (2009), IEEE, pp. 1107–1110.

[100] MacKay, A., Whittall, K., Adler, J., Li, D., Paty, D., and Graeb, D. In vivo visualization of myelin water in brain by magnetic resonance. *Magnetic Resonance in Medicine 31*, 6 (1994), 673–7.

[101] Majumdar, S. Quantitative study of the susceptibility difference between trabecular bone and bone marrow: computer simulations. *Magnetic Resonance in Medicine 22*, 1 (1991), 101–110.

[102] Marques, J., and Bowtell, R. Application of a Fourier-based method for rapid calculation of field inhomogeneity due to spatial variation of magnetic susceptibility. *Concepts in Magnetic Resonance Part B: Magnetic Resonance Engineering 25B*, 1 (2005), 65–78.

[103] Marques, J. P., and Bowtell, R. Using forward calculations of the magnetic field perturbation due to a realistic vascular model to explore the BOLD effect. *NMR in Biomedicine 21*, 6 (2008), 553–565.

[104] Marques, J. P., Maddage, R., Mlynarik, V., and Gruetter, R. On the origin of the MR image phase contrast: an in vivo MR

microscopy study of the rat brain at 14.1 T. *NeuroImage 46*, 2 (2009), 345–352.

[105] Mason, J., Langaman, C., Morell, P., Suzuki, K., and Matsushima, G. Episodic demyelination and subsequent remyelination within the murine central nervous system: changes in axonal calibre. *Neuropathology and Applied Neurobiology 27*, 1 (2001), 50–58.

[106] Matsushima, G., and Morell, P. The neurotoxicant, cuprizone, as a model to study demyelination and remyelination in the central nervous system. *Brain Pathology 11*, 1 (2001), 107–16.

[107] McNeal, D. R. Analysis of a model for excitation of myelinated nerve. *IEEE Transactions on Biomedical Engineering*, 4 (1976), 329–337.

[108] McRobbie, D. W. *MRI from Picture to Proton.* Cambridge University Press, 2007.

[109] Miller, K. L., Smith, S. M., and Jezzard, P. Asymmetries of the balanced SSFP profile. Part II: white matter. *Magnetic Resonance in Medicine 63*, 2 (2010), 396–406.

[110] Morales, L. B. J., Loo, K. K., Liu, H.-b., Peterson, C., Tiwari-Woodruff, S., and Voskuhl, R. R. Treatment with an estrogen receptor α ligand is neuroprotective in experimental autoimmune encephalomyelitis. *The Journal of Neuroscience 26*, 25 (2006), 6823–6833.

[111] Morrish, A. H. *The physical principles of magnetism.* 2001.

[112] Neema, M., Stankiewicz, J., Arora, A., Guss, Z., and Bakshi, R. MRI in multiple sclerosis: whats inside the toolbox? *Neurotherapeutics 4*, 4 (2007), 602–617.

[113] Neumann, H., Kotter, M., and Franklin, R. Debris clearance by microglia: an essential link between degeneration and regeneration. *Brain 132*, 2 (2009), 288–295.

[114] Nicholson, C., and Syková, E. Extracellular space structure revealed by diffusion analysis. *Trends in Neurosciences 21*, 5 (1998), 207–215.

[115] Norton, W. T., and Cammer, W. Isolation and characterization of myelin. In *Myelin*. Springer, 1984, pp. 147–195.

[116] Noseworthy, J., Lucchinetti, C., Rodriguez, M., and Weinshenker, B. Multiple sclerosis. *The New England Journal of Medicine 343*, 13 (2000), 938–952.

[117] Ogawa, S., and Lee, T. M. Magnetic resonance imaging of blood vessels at high fields: in vivo and in vitro measurements and image simulation. *Magnetic Resonance in Medicine 16*, 1 (1990), 9–18.

[118] Ogawa, S., Menon, R. S., Tank, D. W., Kim, S. G., Merkle, H., Ellermann, J. M., and Ugurbil, K. Functional brain mapping by blood oxygenation level-dependent contrast magnetic resonance imaging. a comparison of signal characteristics with a biophysical model. *Biophysical Journal 64*, 3 (1993), 803–812.

[119] Pannese, E. *Neurocytology: Fine structure of neurons, nerve processes, and neuroglial cells*. Thieme, 1994.

[120] Patestas, M., and Gartner, L. *A textbook of neuroanatomy*, 1st edition ed. Blackwell Publishing, 1999.

[121] Peters, A. The effects of normal aging on myelin and nerve fibers: a review. *Journal of Neurocytology 31*, 8-9 (2002), 581–593.

[122] Peters, A. M., Brookes, M. J., Hoogenraad, F. G., Gowland, P. A., Francis, S. T., Morris, P. G., and Bowtell, R. T2* measurements in human brain at 1.5, 3 and 7 T. *Magnetic Resonance Imaging 25*, 6 (2007), 748–753.

[123] Peterson, R., and Bollier, M. Spectrophotometric determination of serum copper with biscyclohexanoneoxalyldihydrazone. *Analytical Chemistry 27*, 7 (1955), 1195–1197.

[124] Pike, G. B., De Stefano, N., Narayanan, S., Worsley, K. J., Pelletier, D., Francis, G. S., Antel, J. P., and Arnold, D. L. Multiple Sclerosis: Magnetization Transfer MR Imaging of White Matter before Lesion Appearance on T2-weighted Images. *Radiology 215*, 3 (2000), 824–830.

[125] Pirko, I., and Johnson, A. Neuroimaging of demyelination and remyelination models. In *Advances in Multiple Sclerosis and Experimental Demyelinating Diseases*. Springer, 2008, pp. 241–266.

[126] Port, J. D., and Pomper, M. G. Quantification and minimization of magnetic susceptibility artifacts on GRE images. *Journal of Computer Assisted Tomography 24*, 6 (2000), 958–964.

[127] Purcell, E. M., Torrey, H., and Pound, R. V. Resonance absorption by nuclear magnetic moments in a solid. *Physical Review 69*, 1-2 (1946), 37–38.

[128] Raine, C. Morphology of myelin and myelination. In *Myelin*, P. Morell, Ed. Springer US, 1984, pp. 1–50.

[129] Salomir, R., de Senneville, B. D., and Moonen, C. T. A fast calculation method for magnetic field inhomogeneity due to an arbitrary distribution of bulk susceptibility. *Concepts in Magnetic Resonance Part B: Magnetic Resonance Engineering 19B*, 1 (2003), 26–34.

[130] Sander, S., Nicholson, G. A., Ouvrier, R. A., McLeod, J. G., and Pollard, J. D. Charcot-Marie-Tooth disease: Histopathological features of the peripheral myelin protein (PMP22) duplication (CMT1A) and Connexin32 mutations (CMTX1). *Muscle and nerve 21*, 2 (1998), 217–225.

[131] Sati, P., Gelderen, P. v., Silva, A. C., Reich, D. S., Merkle, H., de Zwart, J. A., and Duyn, J. H. Micro-compartment specific T2* relaxation in the brain. *NeuroImage 77* (2013), 268–278.

[132] Schäfer, A., Wiggins, C., and Turner, R. Understanding the orientation dependent T2* contrast of the cingulum in ultra high fields. In *Proceedings of the 17th Annual Meeting of ISMRM, Honolulu, Hawaii* (2009), p. 955.

[133] Schenck, J. F. Health and physiological effects of human exposure to whole-body four-Tesla magnetic fields during MRI. *Annals of the New York Academy of Sciences 649*, 1 (1992), 285–301.

[134] Schmierer, K., Tozer, D. J., Scaravilli, F., Altmann, D. R., Barker, G. J., Tofts, P. S., and Miller, D. H. Quantitative magnetization transfer imaging in postmortem multiple sclerosis brain. *Journal of Magnetic Resonance Imaging 26*, 1 (2007), 41–51.

[135] Schmierer, K., Wheeler-Kingshott, C. A., Tozer, D. J., Boulby, P. A., Parkes, H. G., Yousry, T. A., Scaravilli, F., Barker, G. J., Tofts, P. S., and Miller, D. H. Quantitative magnetic resonance of postmortem multiple sclerosis brain before and after fixation. *Magnetic Resonance in Medicine 59*, 2 (2008), 268–277.

[136] Schweser, F., Deistung, A., Lehr, B. W., and Reichenbach, J. R. Quantitative imaging of intrinsic magnetic tissue properties using MRI signal phase: an approach to in vivo brain iron metabolism? *NeuroImage 54*, 4 (2011), 2789–2807.

[137] Sergeant, C., Vesvres, M.-H., Devès, G., and Guillou, F. Calcium, potassium, iron, copper and zinc concentrations in the white and gray matter of the cerebellum and corpus callosum in brain of four genetic mouse strains. *Nuclear Instruments and Methods in Physics Research Section B: Beam Interactions with Materials and Atoms 231*, 1 (2005), 234–238.

[138] Shepherd, T. M., Thelwall, P. E., Stanisz, G. J., and Blackband, S. J. Aldehyde fixative solutions alter the water relaxation and diffusion properties of nervous tissue. *Magnetic Resonance in Medicine 62*, 1 (2009), 26–34.

[139] Shmueli, K., de Zwart, J. A., van Gelderen, P., Li, T.-Q., Dodd, S. J., and Duyn, J. H. Magnetic susceptibility mapping of brain tissue in vivo using MRI phase data. *Magnetic Resonance in Medicine 62*, 6 (2009), 1510–1522.

[140] Shmueli, K., Dodd, S. J., Li, T.-Q., and Duyn, J. H. The contribution of chemical exchange to MRI frequency shifts in brain tissue. *Magnetic Resonance in Medicine 65*, 1 (2011), 35–43.

[141] Skripuletz, T., Hackstette, D., Bauer, K., Gudi, V., Pul, R., Voss, E., Berger, K., Kipp, M., Baumgärtner, W., and Stangel, M. Astrocytes regulate myelin clearance through recruitment of microglia during cuprizone-induced demyelination. *Brain 136*, 1 (2013), 147–167.

[142] Skripuletz, T., Lindner, M., Kotsiari, A., Garde, N., Fokuhl, J., Linsmeier, F., Trebst, C., and Stangel, M. Cortical demyelination is prominent in the murine cuprizone model and is strain-dependent. *The American Journal of Pathology 172*, 4 (2008), 1053–1061.

[143] Sled, J., Levesque, I., Santos, A., Francis, S., Narayanan, S., Brass, S., Arnold, D., and Pike, G. Regional variations in normal brain shown by quantitative magnetization transfer imaging. *Magnetic Resonance in Medicine 51*, 2 (2004), 299–303.

[144] Sofroniew, M. V., and Vinters, H. V. Astrocytes: biology and pathology. *Acta Neuropathologica 119*, 1 (2010), 7–35.

[145] Song, S.-K., Yoshino, J., Le, T. Q., Lin, S.-J., Sun, S.-W., Cross, A. H., and Armstrong, R. C. Demyelination increases radial diffusivity in corpus callosum of mouse brain. *NeuroImage 26*, 1 (2005), 132–140.

[146] Stidworthy, M. F., Genoud, S., Suter, U., Mantei, N., and Franklin, R. J. Quantifying the early stages of remyelination following cuprizone-induced demyelination. *Brain Pathology 13*, 3 (2003), 329–339.

[147] Stoll, G., Trapp, B., and Griffin, J. Macrophage function during Wallerian degeneration of rat optic nerve: clearance of degenerating myelin and Ia expression. *The Journal of Neuroscience 9*, 7 (1989), 2327–2335.

[148] Sun, S.-W., Liang, H.-F., Trinkaus, K., Cross, A. H., Armstrong, R. C., and Song, S.-K. Noninvasive detection of cuprizone induced axonal damage and demyelination in the mouse corpus callosum. *Magnetic Resonance in Medicine 55*, 2 (2006), 302–308.

[149] Suzuki, K. Globoid cell leukodystrophy (Krabbe's disease): update. *Journal of Child Neurology 18*, 9 (2003), 595–603.

[150] Sykova, E. Glia and volume transmission during physiological and pathological states. *Journal of Neural Transmission 112*, 1 (2005), 137–147.

[151] Tartaglia, M., Narayanan, S., De Stefano, N., Arnaoutelis, R., Antel, S., Francis, S., Santos, A., Lapierre, Y., and Arnold, D. Choline is increased in pre-lesional normal appearing white matter in multiple sclerosis. *Journal of Neurology 249*, 10 (2002), 1382–1390.

[152] Theiler, M. Spontaneous encephalomyelitis of mice, a new virus disease. *The Journal of Experimental Medicine 65*, 5 (1937), 705–719.

[153] Thomas, L., Boyko, O., Anthony, D., and Burger, P. MR detection of brain iron. *American Journal of Neuroradiology 14*, 5 (1993), 1043–1048.

[154] Van der Knaap, M. S., Valk, J., and Barkhof, F. *Magnetic resonance of myelination and myelin disorders*. Springer Berlin, 2005.

[155] van Gelderen, P., de Zwart, J. A., Lee, J., Sati, P., Reich, D. S., and Duyn, J. H. Nonexponential t2* decay in white matter. *Magnetic Resonance in Medicine 67*, 1 (2012), 110–117.

[156] van Meer, M. P., Otte, W. M., van der Marel, K., Nijboer, C. H., Kavelaars, A., van der Sprenkel, J. W. B., Viergever, M. A., and Dijkhuizen, R. M. Extent of bilateral neuronal network reorganization and functional recovery in relation to stroke severity. *The Journal of Neuroscience 32*, 13 (2012), 4495–4507.

[157] Velumian, A. A., Samoilova, M., and Fehlings, M. G. Visualization of cytoplasmic diffusion within living myelin sheaths of CNS white matter axons using microinjection of the fluorescent dye Lucifer Yellow. *NeuroImage 56* (2011), 27–34.

[158] Venturini, G. Enzymic activities and sodium, potassium and copper concentrations in mouse brain and liver after cuprizone treatment in vivo. *Journal of Neurochemistry 21*, 5 (1973), 1147–1151.

[159] Waxman, S. G., Kocsis, J. D., and Stys, P. K. *The axon: structure, function, and pathophysiology*. Oxford University Press, 1995.

[160] Weber, B., Keller, A. L., Reichold, J., and Logothetis, N. K. The microvascular system of the striate and extrastriate visual cortex of the macaque. *Cerebral Cortex 18*, 10 (2008), 2318–2330.

[161] Weidenheim, K. M., Kress, Y., Epshteyn, I., Rashbaum, W. K., and Lyman, W. D. Early myelination in the human fetal lumbosacral spinal cord: characterization by light and electron microscopy. *Journal of Neuropathology and Experimental Neurology 51*, 2 (1992), 142–149.

[162] Weinshenker, B. Epidemiology of multiple sclerosis. *Neurologic Clinics 14*, 2 (1996), 291–308.

[163] Wharton, S., and Bowtell, R. Whole-brain susceptibility mapping at high field: a comparison of multiple-and single-orientation methods. *NeuroImage 53*, 2 (2010), 515–525.

[164] Wharton, S., and Bowtell, R. Fiber orientation-dependent white matter contrast in gradient echo MRI. *Proceedings of the National Academy of Sciences 109*, 45 (2012), 18559–18564.

[165] Wharton, S., and Bowtell, R. Gradient echo based fiber orientation mapping using R2* and frequency difference measurements. *NeuroImage* (2013), 1–13.

[166] Wheeler-Kingshott, C. A., and Cercignani, M. About axial and radial diffusivities. *Magnetic Resonance in Medicine 61*, 5 (2009), 1255–1260.

[167] Whittall, K., MacKay, A., Graeb, D., Nugent, R., Li, D., and Paty, D. In vivo measurement of T2 distributions and water contents in normal human brain. *Magnetic Resonance in Medicine 37*, 1 (1997), 34–43.

[168] Whittall, K., MacKay, A., and Li, D. Are mono-exponential fits to a few echoes sufficient to determine T2 relaxation for in vivo human brain? *Magnetic Resonance in Medicine 41*, 6 (1999), 1255–7.

[169] Wiggins, C., Gudmundsdottir, V., Bihan, L., Lebon, D., and M., V. C. Orientation dependence of white matter T2* contrast at 7 T: a direct demonstration. In *Proceedings of the 16th Annual Meeting of ISMRM, Toronto, Canada,* (2008), p. 237.

[170] Wilhelm, M. J., Ong, H. H., Wehrli, S. L., Li, C., Tsai, P.-H., Hackney, D. B., and Wehrli, F. W. Direct magnetic resonance detection of myelin and prospects for quantitative imaging of myelin density. *Proceedings of the National Academy of Sciences 109*, 24 (2012), 9605–9610.

[171] Yablonskiy, D. A. Quantitation of intrinsic magnetic susceptibility-related effects in a tissue matrix. phantom study. *Magnetic Resonance in Medicine 39*, 3 (1998), 417–428.

[172] Yablonskiy, D. A., and Haacke, E. M. Theory of NMR signal behavior in magnetically inhomogeneous tissues: the static dephasing regime. *Magnetic Resonance in Medicine 32*, 6 (1994), 749–763.

[173] Yakovlev, P. I., and Lecours, A.-R. The myelogenetic cycles of regional maturation of the brain. *Regional Development of the Brain in Early Life* (1967), 3–70.

[174] Yandava, B. D., Billinghurst, L. L., and Snyder, E. Y. Global cell replacement is feasible via neural stem cell transplantation: evidence from the dysmyelinated shiverer mouse brain. *Proceedings of the National Academy of Sciences 96*, 12 (1999), 7029–7034.

[175] Yuan, D., and Elvidge, C. D. Comparison of relative radiometric normalization techniques. *ISPRS Journal of Photogrammetry and Remote Sensing 51*, 3 (1996), 117–126.

[176] Yudilevich, E., and Stark, H. Spiral sampling in magnetic resonance imaging-the effect of inhomogeneities. *IEEE Transactions on Medical Imaging 6*, 4 (1987), 337–345.

[177] Zhang, J., Jones, M. V., McMahon, M. T., Mori, S., and Calabresi, P. A. In vivo and ex vivo diffusion tensor imaging of cuprizone-induced demyelination in the mouse corpus callosum. *Magnetic Resonance in Medicine 67*, 3 (2012), 750–759.